

THESIS FOR THE DEGREE OF DOCTOR OF PHILOSOPHY IN NATURAL SCIENCE,  
SPECIALISING IN CHEMISTRY

**Strong exciton-photon and exciton-exciton  
coupling and its effects on molecular  
photophysics**

Yi Yu



**UNIVERSITY OF GOTHENBURG**

Department of Chemistry and Molecular Biology  
University of Gothenburg  
Gothenburg, Sweden

**Strong exciton-photon and exciton-exciton coupling and its effects on molecular photophysics**

© Yi Yu, 2023

Department of Chemistry and Molecular Biology,  
University of Gothenburg,  
SE-412 96 Gothenburg,  
Sweden

Printed by Stema Specialtryck AB  
Borås, Sweden 2023

ISBN: 978-91-8009-099-7 (PRINT)

ISBN: 978-91-8009-700-0 (PDF)

# Abstract

The energy of molecular states and their transition dynamics form the key properties to understand the photophysics of organic molecules. Strong exciton-photon and exciton-exciton couplings enables the possibility to manipulate these properties without changing the chemical structures. This is due to the formation of new energy states. Furthermore, the transition dynamics between the newly-generated and original molecular states need to be considered.

This dissertation describes the preparation, characterization and simulation of strongly coupled systems and their use for studying molecular photophysical properties. An energy-inverted singlet-triplet system was achieved by strong exciton-photon coupling. This opens up a new pathway to allow a barrier-free reverse intersystem crossing in organic dyes. In addition, the manipulation of excimer emission by strong exciton-photon coupling was analyzed. It was found that the ratio of the intensity of polaritonic and excimer emission depended on the detuning between the molecular and photonic contributions of the hybrid light-matter state, as well as the energy position of that state. Finally, a strongly exciton-exciton coupled system was realized through the formation of J-aggregates. In the aggregates, the exciton delocalization counteracted the energy gap law and led to an innovative strategy for generating highly emissive dyes in the near-infrared regime.

The research results and analysis in this thesis contribute to a deeper understanding of the fundamental molecular photophysics in the strong exciton-photon and exciton-exciton coupling regimes. This paves the way for many potential future applications, such as light emitting devices and photothermal therapies.



# List of publications

## Publications included in this thesis work

**Paper I Barrier-free reverse-intersystem crossing in organic molecules by strong light-matter coupling**

Yu, Y., Mallick, S., Wang, M., and Börjesson, K.  
*Nat. Commun.* 2021, **12**, 3255.

**Paper II Interplay between polaritonic and molecular trap states**

Mony J.†, Yu, Y.†, Schäfer C., Mallik S., Kushwaha K., and Börjesson, K.  
*J. Phys. Chem. C* 2022, **126**, 7965.

**Paper III Exciton Delocalization Counteracts the Energy Gap: A New Pathway toward NIR-Emissive Dyes**

Cravencio A., Yu Y., Edhborg F., Goebel J.F., Takacs Z., Yang Y., Albinsson B. and Börjesson K.  
*J. Am. Chem. Soc.* 2021, **143**, 19232.

## Further publication not included in this thesis

**Paper IV Chemical transformer compression for accelerating both training and inference of molecular modeling**

Yu Y., and Börjesson K.  
*Mach. Learn.: Sci. Technol.* 2022, **3**, 045009.

†Authors contributed equally to this work.



# Paper Contribution

- Paper I** Prepared all samples and performed all spectroscopic experiments, set up the temperature-dependent measurement for the emission and the emission lifetime. Analyzed the data of transition dynamics and wrote the paper together with the other authors
- Paper II** Prepared all samples and performed all spectroscopic experiments for the delayed emission samples. Analyzed the data and wrote the paper together with the other authors.
- Paper III** Performed spectroscopic measurement for the monomer and aggregates. Analyzed the data of exciton coupling and wrote the paper together with the other authors.



# Contents

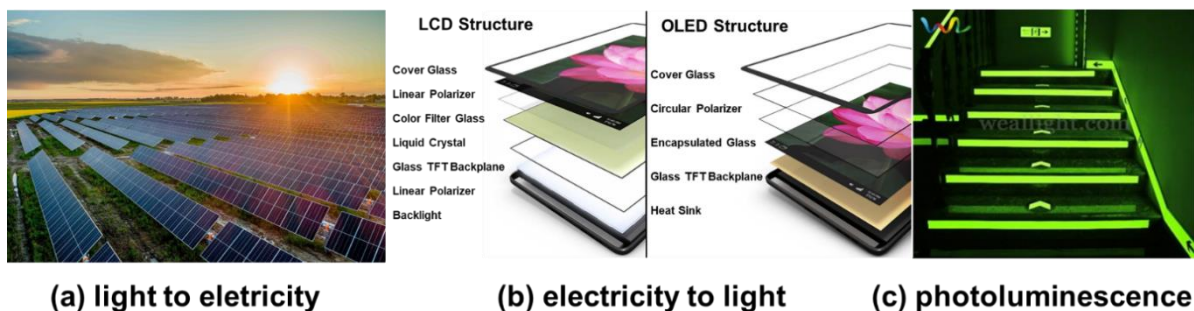
<b>1. Introductions.....</b>	<b>1</b>
<b>2. Background.....</b>	<b>3</b>
2.1 Basic principles .....	3
2.1.1 Electromagnetic waves.....	3
2.1.2 Einstein coefficients .....	4
2.1.3 Rabi oscillation.....	5
2.2 Photophysical properties of molecules.....	6
2.2.1 Molecular electronic and vibrational states.....	6
2.2.2 Molecular absorption and the transition dipole moment.....	9
2.2.3 Transition dynamics in the excited state .....	10
2.2.4 Excimer formation and properties.....	12
2.3 The theory of strong exciton-photon coupling.....	13
2.3.1 Different principles of strong exciton-photon coupling.....	13
2.3.2 The realization of strong coupling by the optical cavity.....	15
2.3.3 Dispersive behavior.....	17
2.3.4 Strong coupling limit.....	18
2.4 Exciton-exciton coupling in molecular aggregates .....	19
2.4.1 The Kasha Theory for aggregates .....	19
2.4.2 Photophysical properties of the aggregates.....	22
<b>3. Strong exciton-photon and exciton-exciton coupling and its effects on molecular photophysics.....</b>	<b>25</b>
3.1 Transition dynamics starting from triplet states .....	25
3.1.1 Thermally activated delayed fluorescence and reverse intersystem crossing ...	25
3.1.2 Two types of TADF emitters .....	26
3.1.3 The effects of spin-orbit coupling and the inverted system .....	29
3.1.4 Fundamental understanding of the transition dynamics of the TADF process .	30
3.2 Barrier-free reverse-intersystem crossing by strong light-matter coupling in TADF molecules.....	34
3.3 Manipulation of molecular trap states by strong light-matter coupling.....	40
3.4 Energy gap law considering the effect of excitonic coupling .....	45
3.5 Overcoming the energy gap law by strong excitonic coupling.....	47
<b>4. Methodology .....</b>	<b>51</b>
4.1 Organic film preparation .....	51

4.2 The growth of silver layers.....	52
4.3 Ultraviolet-visible spectroscopy.....	53
4.4 Emission spectra by photoluminescent spectrometer.....	54
4.5 The measurement of time-resolved photoluminescence spectra.....	55
<b>5. Summary and Outlook.....</b>	<b>57</b>
<b>Acknowledgement .....</b>	<b>59</b>
<b>Bibliography .....</b>	<b>61</b>
<b>Appendix .....</b>	<b>67</b>

# 1. Introductions

Studies of the interaction between light and matter have attracted intense attention in the past decades. However, humans had already begun to study these interactions 1,000 years ago (984 A.D.), when Ibn-Sahl discussed the properties of lenses and demonstrated the geometric arguments of Snell's law<sup>[1]</sup>. Several hundred years later, the scientific revolution occurred. In this period, people started to carry out quantitative research based on “fresh” theories and models. For example, James Clerk Maxwell proposed the well-known Maxwell's equations<sup>[2]</sup>. These equations are a set of coupled partial differential equations that provide a mathematical model to help us understand optical and electric properties. Maxwell, for the first time, used this theory to show that light is an electromagnetic phenomenon<sup>[3]</sup>. In 1924, De Broglie suggested that electrons have wave properties, similar to light<sup>[4]</sup>. Furthermore, in 1927, Dirac studied light-matter interactions using the theory of quantum mechanics<sup>[5]</sup>.

Supported by the results from deeper studies, these scientific theories and technologies have facilitated our ordinary lives. For example, matter in the form of an electronic device can convert light into electrical energy<sup>[6-8]</sup>. This type of devices are called solar cells (**Figure 1.1a**). Conversely, matters can emit light when electrically pumped, which is named electroluminescent devices<sup>[9]</sup> (**Figure 1.1b**). Besides, energy conversion by light-matter interactions, energy transitions also occur inside matter<sup>[10-12]</sup>. The color of one type of matters can be characterized by its absorption properties. After absorption, the light is not only converted into heat, but also can emit light in other colors (**Figure 1.1c**). Taking the photoluminescent emergency exit sign as an example, it can emit green light to guide us to env-



(a) light to electricity

(b) electricity to light

(c) photoluminescence

**Figure 1.1** (a) The case for the energy conversion from light to electricity; (b) energy conversion from electricity to light; c) matters emitting light by photoluminescence.

-acuate in orderly manner during a power outage. The mechanism of this light-to-light transition is a long-lived photoluminescent process, namely phosphorescence. Accordingly, the study of the interaction between light and matter has resulted in valuable applications to improve our society<sup>[13-18]</sup>.

When it interacts with light, matters can also be affected by its surrounding environment. Following exposure to light, exciton-photon coupling occurs. The coupling results in the absorption of a photon, which occurs all around us and is responsible for the color that we perceive. As the coupling strength continues to increase, new eigenstates are formed. We can say that the matter is in the strong coupling regime. Yakovlev and colleagues observed this phenomenon for the first time in a LiF film placed on sapphire and rutile surfaces<sup>[19]</sup>. Thereafter, strong coupling regimes were achieved for many inorganic materials<sup>[19-28]</sup>. The first published case of an organic molecule reaching this regime was in 1998 by Lidzey et al<sup>[29, 30]</sup>. One advantage for organic molecules is that they have large transition dipole moments, which makes it easy for matters to achieve the strong coupling regime at room temperature.

In similarity to exciton-photon coupling, molecules can be coupled by themselves through exciton-exciton interactions<sup>[31]</sup>. In such systems, the Coulombic interaction between molecules is of significance, as well as the packing arrangement<sup>[32]</sup>. If the interaction is strong enough, new hybrid exciton-exciton states will occur. Eventually, the molecular properties will be dramatically changed<sup>[33]</sup>.

As mentioned above, both strong exciton-photon and exciton-exciton couplings contribute to altered new energy states. Numerous studies have examined the direct effect on the molecular excited singlet states, which can be strongly coupled to light. Other than the excited singlet state, the triplet state is quantum mechanically forbidden to interact with light, which means that it cannot be strongly coupled. However, transitions to and from triplet states may be affected by strong coupling, since transitions depend on the energy difference between two states<sup>[18]</sup>. With the singlet state strongly coupled, the energy differences between states are changed, thereby affecting the dynamics<sup>[34]</sup>. Therefore, a focus of this thesis is understanding the effect that strong coupling has on the transition dynamics, starting from the triplet channel. The goal is to study these dynamics in greater depth, so as to unveil the potential of strong coupling. Meanwhile, compared with the light emitting in ultraviolet and visible regime, molecular light that is emitted in the near-infrared (NIR) range shows a relatively low quantum yield<sup>[35, 36]</sup>. Another focus of this thesis is on strong exciton-exciton coupling. How does this coupling extend the emission windows of organic molecules towards the NIR region of the electromagnetic spectrum? In addition, how does such coupling affect the efficiency of a system to emit light? The answers to these questions will provide a deeper understanding of molecular transition dynamics, which could result in valuable applications, such as organic light-emitting devices (OLEDs) and photodynamic therapies.

## 2. Background

This chapter describes the background and theory relevant to understanding the photophysical processes that occurs in organic molecules and cavities. **Section 2.1** describes the basic properties of light. **Section 2.2** discusses the photophysical properties of molecules. **Section 2.3** describes the fundamentals of strong light-matter interactions, and **Section 2.4** covers the basics of excitonic coupling in molecular aggregates.

### 2.1 Basic principles

#### 2.1.1 Electromagnetic waves

Light is an electromagnetic wave that can be described classically by Maxwell's equations<sup>[2]</sup>. Electromagnetic waves consist of a synchronously oscillating electric and magnetic field, propagating through space. As shown in **Figure 2.1**, they can be characterized by their frequency of oscillation or by their wavelength ( $\lambda$ ).

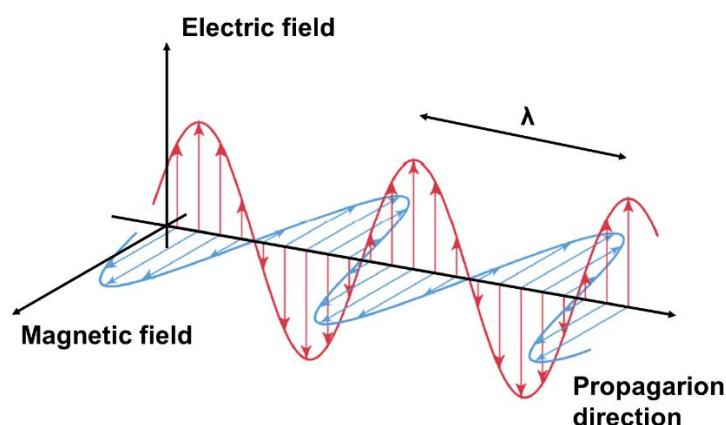


**Figure 2.1** An electromagnetic wave consists of an oscillating electric field (red) and an oscillating magnetic field (blue) that is perpendicularly propagating through space in the same direction;  $\lambda$  defines the spatial period, namely the wavelength.

The electromagnetic spectrum is classified according to wavelength into infrared, visible, ultraviolet, X-ray and others. When the electromagnetic wave interacts with matters, a photoelectric effect can occur. This is a phenomenon in which electrically charged particles are

released from or within a material when it absorbs electromagnetic radiation. To explain the photoelectric effect<sup>[37]</sup>, it was first proposed that light is a discrete packet of energy, and later this became known as a photon. The energy ( $E$ ) of a photon is described by its frequency  $\nu$  and Planck's constant  $h$ <sup>[38]</sup>, or alternatively, by its angular frequency  $\omega$  and the reduced Planck's constant  $\hbar$ , as in **Equation 2.1**,

$$E = h\nu = \hbar\omega \quad (2.1)$$

A simple case of an interaction between an electromagnetic wave and matter is the absorption or emission of photons by a system of atoms with stationary energy levels. According to the Bohr frequency condition<sup>[39]</sup>, the energy difference between two involved energy states should be equal to the frequency of the radiation multiplied by Planck's constant, as shown in **Equation 2.2**,

$$\Delta E = h\nu = \hbar\omega \quad (2.2)$$

In optical spectroscopy, a monochromator is incorporated into a fluorescence spectrophotometer and emission spectrometer to determine the wavelengths of the fluorescence lines or emission lines emitted from the sample. Then, the wavelength  $\lambda$  is usually utilized. Hence, the Bohr condition can be expressed as the rate of light  $c$  as well in **Equation 2.3**,

$$\Delta E = \frac{hc}{\lambda} \quad (2.3)$$

### 2.1.2 Einstein coefficients

Einstein proposed three possible processes for the interaction between a photon and a two-level system (**Figure 2.2**), which consists of two discrete energy levels that are separated in energy<sup>[40]</sup>. The first process entails stimulated absorption, in which the system is excited after absorbing a photon. The variation of the excited state population with time for this process  $dN_1/dt$  can be described by **Equation 2.4**,

$$\frac{dN_1}{dt} = N_0 B_{01} \rho(\nu) \quad (2.4)$$

where  $N_0$  is the number of the ground state ( $S_0$ ),  $B_{01}$  is the Einstein coefficient of stimulated absorption, and  $\rho(\nu)$  is the spectral density of the radiation frequency, which represents the different ratios among the radiation frequencies.

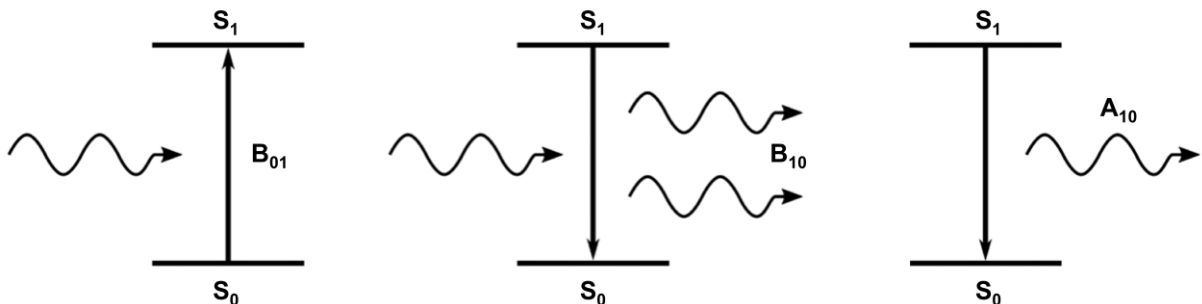


**Figure 2.2** Three processes of interaction between the ground state ( $S_0$ ) and excited state ( $S_1$ ): absorption ( $B_{01}$ ), stimulated ( $B_{10}$ ), and spontaneous ( $A_{10}$ ) emissions in a two-level system.

The second process is stimulated emission, which works in the opposite way to absorption. One photon stimulates the emission of another photon from an excited two-level system. Over time, the depopulation of the excited state is determined by **Equation 2.5**,

$$\frac{dN_1}{dt} = -N_1 B_{10} \rho(\nu) \quad (2.5)$$

where  $N_1$  is the number of the excited state  $S_1$ , and  $B_{10}$  is the Einstein coefficient of stimulated emission. The population inversion of the two-level system can be realized owing to the competing processes of stimulated emission and absorption.

The third process is spontaneous emission, whereby a two-level system relaxes to its ground state by emitting a single photon. In contrast to the other two processes, spontaneous emission is independent of any photon radiation and depends only on the Einstein coefficient of spontaneous emission  $A_{10}$  and the number of excited states  $N_1$ , as shown in **equation 2.6**,

$$\frac{dN_1}{dt} = -N_1 A_{10} \quad (2.6)$$

The relationship between the Einstein coefficients of the spontaneous and stimulated emission can be obtained from the steady-state condition. This condition is shown in **Equation 2.7**,

$$B_{01} N_0 \rho(\nu) = B_{10} N_1 \rho(\nu) + A_{10} N_1 \quad (2.7)$$

This means that in the steady-state condition, the two emission rates (spontaneous and stimulated) must counterbalance the rate of absorption. According to this condition, the populations of the different states are in equilibrium. Using Planck's distribution and the Boltzmann expression<sup>[41]</sup>, the relationship is determined as follows in **Equation 2.8**,

$$A_{10} = \frac{8\pi h \nu^3}{c^3} B_{10} \quad (2.8)$$

### 2.1.3 Rabi oscillation

Rabi oscillation is a highly simplified model that does not consider any relaxation, decay or dephasing. It appears in quantum two-level systems that interact with an external electromagnetic fields<sup>[42]</sup>. If the excitation frequency of the electromagnetic field approaches the resonant frequency of the two levels, the system starts to oscillate between the ground state and the excited state with the Rabi frequency. The expression for the frequency is shown in **Equation 2.9**,

$$\Omega_R = \frac{d|E_0|}{\hbar} \quad (2.9)$$

where  $d$  is the associated transition dipole moment (a complex vector quantity that shows the interactions between the molecules and the electromagnetic wave; it will be explained in detail in **Section 2.2.2**), and  $E_0$  is the amplitude of the electric field. Assuming that the system is initially in the ground state, the probability of the system being in the excited state is,

$$P_e(t) = \frac{\Omega_R}{\sqrt{\Omega_R + \delta^2}} \sin^2 \frac{\sqrt{\Omega_R + \delta^2}}{2} t \quad (2.10)$$

where  $P_e(t)$  is the probability of being in the excited state and  $\delta$  is the difference between the energies of the light and the two-level transition. The probability of being in the excited state oscillates over time, which means that successive excitation of a two-level system does not always lead to a transition into the excited state (**Figure 2.3**). Once a sufficiently high excited state density is generated, further excitations return the system to its ground state due to stimulated emission. Detuning affects the probability and energy of the oscillations. Only in the absence of detuning, the probability of being in the excited state reaches unity at specific times. Moreover, the system remains in the same state if the external field is shut off.

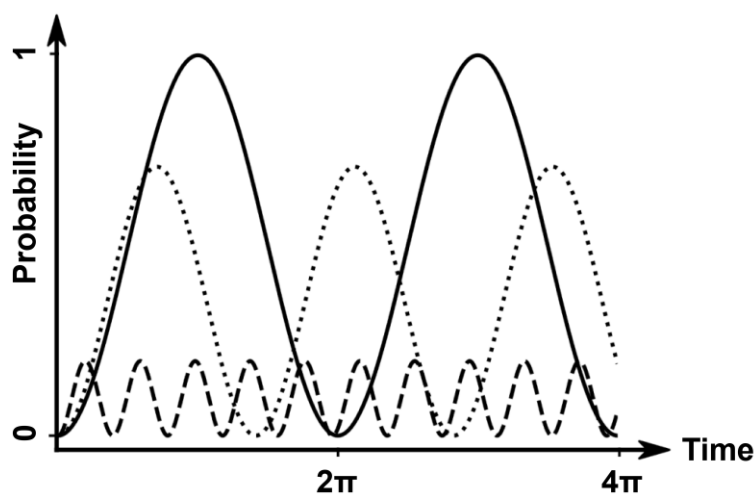


**Figure 2.3** Rabi oscillation describing the probability of the system in the excited state over time using different detuning values of  $\delta = 0$  (solid line),  $\Omega_R$  (dotted line) and  $5\Omega_R$  (dashed line).

## 2.2 Photophysical properties of molecules

Having settled the basic properties of the light, we now turn our attention to the molecules. The energetic structures of molecules involve various levels and transitions. In this section, the molecular energy states, absorption and transition dynamics will be discussed.

### 2.2.1 Molecular electronic and vibrational states

#### The Schrödinger equation, electronic states and molecular orbitals

Organic molecules are composed of atomic assemblies with a positive nucleus and negative electrons. The electrons exhibit wave-particle duality. In other words, they can be described both as particles and waves. Therefore, electrons can only be understood through quantum mechanics, instead of classical mechanics. Then, this kind of knowledge can be utilized to represent the organic molecule. Generally, in quantum system, the energy level of molecules can be described by the time-independent Schrödinger equation<sup>[43]</sup>, shown in **equation 2.11**,

$$\hat{H}\Psi = E\Psi \quad (2.11)$$

where  $\hat{H}$  is the Hamiltonian operator, which represents the total energy of the system including

the kinetic and potential energies,  $\Psi$  is the wave function, and  $E$  is the total energy, which can be divided into kinetic energy, potential energy, and electron-electron interaction energy. The Schrödinger equation can only be solved analytically for a hydrogen atom without electron-electron interaction energy<sup>[44]</sup>.

To overcome the difficulty above, zero-order Born Oppenheimer approximation is adopted, where the nuclei of the atoms are served as classical positive particles at unchanged positions<sup>[45]</sup>. This approximation simplified the description of the molecules in the description of quantum mechanics. In quantum mechanics, the electronic systems are generally characterized by the quantum number: principal ( $n$ ), orbital angular momentum ( $l$ ), magnetic ( $m_l$ ) and electron spin quantum number ( $m_s$ , namely spin as well). Firstly, the principal quantum number is related to the energy of the state ( $n = 1, 2, 3 \dots$ ). Next, the angular one ranges from 0 to  $n-1$ , which determines the angular distribution of the atoms. Then, the atomic orbital with specific  $n$  and  $l$  states can be oriented in different directions, which is described by the magnetic quantum number ( $m_l = 0, \pm 1, \pm 2 \dots, \pm l$ ). Finally, the last quantum number does not depend on any quantum number above. It represents the state of the intrinsic rotation. The  $m_s$  can be in two states with  $m_s = +1/2$ , denoted as  $\uparrow$ , and with  $m_s = -1/2$ , denoted as  $\downarrow$ .

Molecular orbital (MO) theory<sup>[46]</sup> is used to study the multiply-electron systems. In absorption and luminescent spectroscopy, the highest occupied molecular orbital (HOMO) and the lowest unoccupied molecular orbital (LUMO) play key roles. The transition from HOMO to LUMO can be described in the way that electrons are promoted into one or more of the unoccupied orbitals. Thereafter, the excitation energy should be determined by the energy differences between the respective orbitals.

In multiple electron systems, the electron configuration will often give rise to a number of different electronic states if the electrons can be arranged in different ways. The molecular ground state ( $S_0$ ) follow three rules: the Aufbau principle<sup>[47]</sup>, Pauli Exclusion principle<sup>[48]</sup> and Hund's rule<sup>[49]</sup>. According to the Hund's rule, the electrons should not be spin paired before each orbital contains one electron. Therefore, the molecular total spin ( $S = |\sum m_s|$ ) in ground state is 0 and the spin multiplicity ( $M, M = 2S + 1$ ) is equal to 1, which is called as singlet state. As a molecule is excited to the higher state, it can still have equal number of electrons in the  $m_s$ . Hence, the spin multiplicity is equal to 1 as well, which is deemed to be in the excited singlet state ( $S_1$ ). If the molecular total spin is 1,  $M$  is equal to 3. The system is called excited triplet state. Accordingly, the difference among these three states is shown in **Figure 2.4**.

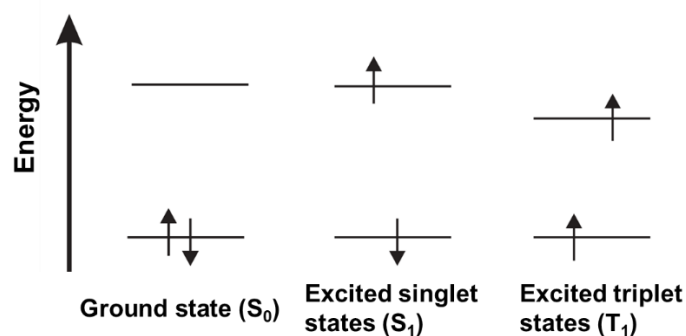


**Figure 2.4** The difference among the ground state ( $S_1$ ), excited singlet ( $S_0$ ) and triplet ( $T_1$ ) states.

### Vibrational states

The nucleus of the molecule vibrates around its equilibrium position, instead of remaining

stationary. The vibration of a molecule is quantized, which results in two consequences. On the one hand, the nuclei cannot be completely at rest. Even in the lowest energy state, they undergo so-called zero-point vibrations, which contributes positively to the total energy of the molecule. On the other hand, the possible levels of vibrational energy are discontinuous, and the spacing between the levels of vibrational energy is much smaller than the electron excitation energy. As a result of these molecular vibrations, for each electronic state of a molecule there exists a series of vibrational energy levels associated with that state.

By solving the Schrödinger equation, the energy eigenstates of the vibrational state  $E_v^{[44]}$  are shown in **Equation 2.12**,

$$E_v = \hbar\omega \left( v + \frac{1}{2} \right) \quad (2.12)$$

where  $v$  is the vibrational quantum number. It is clear from the equations that the energy levels are equidistant and never zero. Nonetheless, the potential energy surface in reality is not a perfect oscillator. Considering the classical picture of two atoms connected by a spring, it is clear that the bond will break if the spring is distorted at some level. Harmonic oscillators are also ineffective at bringing two positively charged nuclei too close to each other. By some level of approximation, the Coulomb repulsion will begin to play a key role. As an approximation of the potential energy surface, the Morse potential<sup>[50]</sup> is introduced in **Equations 2.13**,

$$V(r) = D_e(1 - e^{-a(r-r_e)})^2 \quad (2.13)$$

where  $V(r)$  is the Morse potential,  $D_e$  is the dissociation energy, and  $r - r_e$  is the distortion. **Figure 2.5** shows clearly the difference between a harmonic oscillator (black) and Morse potential.

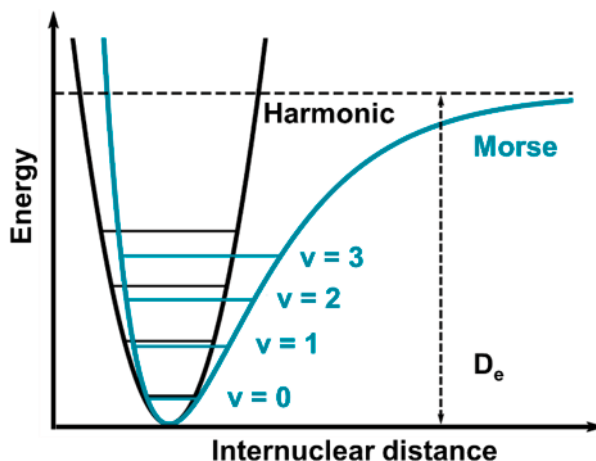


**Figure 2.5** Energy schemes of the harmonic oscillator (black) and Morse potential (green), with some of the vibrational levels and the bond dissociation energy  $D_e$ .

The corrected potential energy is accompanied by a shift in the vibrational energy levels, so that they are no longer equidistant. However, it is still a good approximation to assume that the lowest vibrational levels are uniformly separated.

## 2.2.2 Molecular absorption and the transition dipole moment

### Molecular absorption

The electrons in molecules can interact with electromagnetic radiation. Through perturbation of the electron wave function, the radiation can lead to an electronic transition. For example, this type of transition in molecules occurs when they absorb a photon. A molecule that has absorbed a photon changes its configuration so that a molecular transition occurs from the ground state to the excited state.

In this case, light is described as an electromagnetic field that oscillates with the frequency of the photon, as shown in **Figure 2.1**. To describe the absorption of photons, one must start with the ground state of the molecule. When an external electric field (photon) is applied, the wave function of the electron generally changes only slightly and temporarily. Nevertheless, in molecules, if the energy of the photon matches the energy gap ( $\Delta$ ) between the ground state and some excited states, the photon frequency  $\nu$  satisfies the Bohr frequency condition<sup>[51]</sup>, which is given by **Equation 2.2**. Then, the wave function resonates with the oscillatory field. Finally, there is a finite possibility that the molecule transfers from the ground state to the corresponding excited state. Meanwhile, the photon gets absorbed.

### Transition dipole moment and selection rule

The Bohr frequency condition described in Equation 2.3 is important but not sufficient for the absorption process. Additionally, the initial and final electronic states must be suitable for the excitation by the electric field. Mathematically, this condition can be expressed with the help of the transition dipole moment  $M_{n \rightarrow m}$  between the initial ( $n$ ) and final states ( $m$ ), as represented in **Equation 2.14**,

$$M_{n \rightarrow m} = \langle \Psi_m | \hat{\mu} | \Psi_n \rangle \quad (2.14)$$

where  $\Psi_n$  and  $\Psi_m$  are the electronic wave functions of the initial states and final state, respectively,  $\hat{\mu}$  is the sum of the vectors that define the positions of the electrons, namely the operator of the transition dipole moment. If the absorption procedure is possible, the dipole moment operator should be non-zero. Meanwhile, the probability ( $P$ ) of the absorption is proportional to  $M_{n \rightarrow m}$ , as shown in **Equation 2.15**,

$$P \propto |\langle \Psi_m | \hat{\mu} | \Psi_n \rangle|^2 \quad (2.15)$$

In order to study the probability of absorption in greater depth, selection rules are introduced<sup>[52]</sup>. These rules are essential for understanding the behavior of a particular system and for designing systems with specific properties. Selection rules are used to predict the strength of electronic transitions and are usually discussed in the framework of symmetry and spin.

Regarding symmetry, if the molecule under consideration has a center of inversion, then all the eigenstates are either symmetric (even parity) or antisymmetric (odd parity). As shown in **Equation 2.15**, the transition dipole moment can only be non-zero for states with different parities ( $\Psi$  represents the different wave functions). In other words, radiative transitions are only possible from a symmetric to an antisymmetric state or vice versa. In practice, symmetry-forbidden transition can still occur, however at considerably lower rates than symmetry-allowed transitions. This is the case because vibrations of appropriate symmetry lead to an admixture of

the forbidden excited state with some allowed state. This phenomenon is termed vibronic coupling (vibrational and electronic), and it is neglected within the Born-Oppenheimer approximation.

Regarding spin, the transition can be non-zero only if the initial and final state are in the same spin condition (here in **Equation 2.15**,  $\Psi$  represents the electronic spin wave function). In other words, they should have the same multiplicity and total electron spin direction. Electron transitions are designated as spin-allowed transitions when the multiplicity of the states is the same. This spin selection rule is valid to the extent that spin and orbital functions can be separated. Deviations from this rule result in transitions between states of different multiplicities, namely spin-forbidden transitions that are due to spin-orbit coupling (SOC)<sup>[53]</sup>. This is a relativistic effect resulting from the interaction of the spin magnetic moment with the magnetic moment owing to its operation in the nuclear electrostatic field<sup>[54]</sup>. High SOC can be observed in elements that have a high nuclear charge, and this is referred to as the heavy atom effect<sup>[55]</sup>. To our knowledge, SOC is crucial in photochemistry, allowing spin-forbidden processes such as phosphorescence to occur in organic molecules. Accordingly, the symmetric selection rule applies to radiative processes, while the spin selection rule applies to both radiative and non-radiative processes, as outlined below.

### 2.2.3 Transition dynamics in the excited state

#### Perrin-Jablonski diagram

After molecular absorption, the molecule is excited into higher electronic and vibrational energy levels. The energy transitions among those states are summarized in the Perrin-Jablonski diagram<sup>[56]</sup> in **Figure 2.6**. The different processes can be classified as radiative and non-radiative. Absorption, fluorescence and phosphorescence are radiative processes, while intersystem crossover (ISC), internal conversion (IC) and vibrational relaxation are non-radiative processes. Further information on these two processes will be given in the following section.

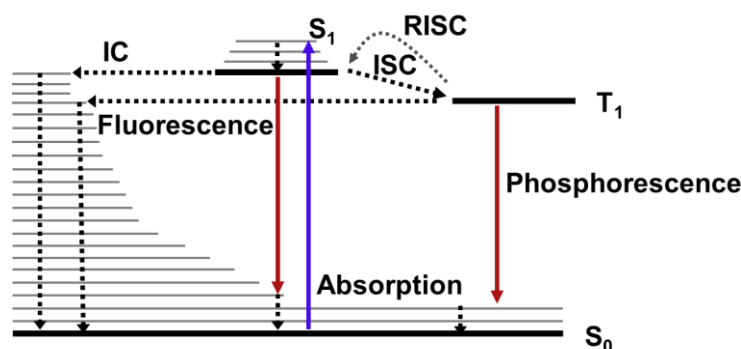


**Figure 2.6** Perrin-Jablonski diagram of the photophysical process for the molecule. The thick black lines represent the electronic levels, while the thin gray lines represent the vibrational levels. The blue arrow represents molecular absorption, and the red arrows represent radiative transitions for emission. The dashed arrows represent the non-radiative processes for internal conversion (IC), intersystem crossing (ISC), and reverse intersystem crossing (RISC).

#### Non-radiative processes and the energy gap law

Non-radiative decay occurs in the absence of photon emission, and follows several possible mechanisms. The system can be relaxed from a higher vibrational level to the lowest one within

the same electronic state. The excess energy is released to the surroundings. In general, vibrational relaxation is the fastest process, whereby the molecule will relax to the lowest vibrational level. Then, it will undergo other radiative or non-radiative processes. Therefore, emissions are rarely found at higher vibrational levels due to vibrational relaxation.

Other than transition within the same electronic state, a system can be converted to a lower energy level that belongs to another electronic state. IC is one of these non-radiative processes<sup>[57]</sup>. In contrast to vibrational relaxation, IC process changes the electronic state of the molecule. This process is usually irreversible because it is followed by a very rapid vibrational relaxation, which brings the molecule down to the lowest vibrational level. Together with vibrational relaxation, this is the reason for Kasha's rule, which states that for a given multiplicity, the luminescence originates only from the lowest excited state<sup>[58]</sup>. This means that the fluorescence is independent of the excitation wavelength. This is because the IC process and vibrational relaxation of the excited state occur faster than the luminescence from the higher excited state.

ISC is another non-radiative process. In this process, the molecules go from the excited singlet to the excited triplet state. Since the spin must flip, this is a spin-forbidden transition and is, therefore, very slow. The rate constant can be increased by stronger spin-orbit coupling<sup>[53, 59]</sup>, allowing the transition to proceed. This can be achieved by introducing heavy atoms into the molecular structure. In similarity to IC, the ISC process is irreversible due to the rapid vibrational relaxation. There exist, however, some molecules that can undergo reverse intersystem crossing (RISC) after ISC. These molecules exhibit thermally activated delayed fluorescence (TADF)<sup>[60]</sup>. A prerequisite for this behavior is that the energy difference between the excited singlet and the triplet states is as small as possible. The spin, triplet state and RISC will be elaborated upon in the next chapter.

The rate of non-radiative decay follows the energy gap law<sup>[61]</sup>. According to this law, the rate decreases exponentially as the energy difference between two electronic states increases in a series of related molecules. A quantitative explanation for the energy gap law will be provided in the next chapter.

### **Radiative processes, lifetimes and the quantum yield**

A radiative process involves the transition of a molecule from an excited state to a ground state through the emission of a photon, which corresponds to the spontaneous emission mentioned in **Section 2.2.1**. The two main forms of radiative decay are fluorescence and phosphorescence. The difference between these processes is that fluorescence involves a transition from an excited singlet state to a singlet ground state, while phosphorescence is from an excited triplet state to a singlet ground state. Thus, phosphorescence is a spin-forbidden transition, which can be enhanced by spin-orbit coupling, as described earlier<sup>[53, 59]</sup>. Since phosphorescence is a spin-forbidden process, its radiative rate is many orders of magnitude lower than that of fluorescence. The fluorescence lifetime is used to describe the average time that a population of molecules spend in an excited singlet state before decay. It represents the relationship between the radiative and non-radiative processes in molecules. The relationship between the lifetime and two rate constants is expressed by **Equation 2.16**<sup>[62]</sup>,

$$\tau_f = \frac{1}{k_f + \sum k_{nr}} \quad (2.16)$$

where  $k_f$  is the fluorescent rate, and  $\sum k_{nr}$  is the rate of the sum of non-radiative processes, including the IC and ISC. Regarding the quantum yield, it is defined as the ratio of the number of emitted photons to the number of absorbed photons. According to Kasha's rule, the quantum yield is expected to be independent of the excitation wavelength because the internal relaxation process is much faster than radiative or non-radiative decay. The quantum yield can be written as the sum of the non-radiative rate  $\sum k_{nr}$  and the radiative decay rate  $k_f$ <sup>[63]</sup>, as expressed in **Equation 2.17**,

$$\Phi_f = \frac{k_f}{k_f + \sum k_{nr}} \quad (2.17)$$

If the rate of fluorescence exceeds the rate of all non-radiative decays, the quantum yield is close to 1. When the non-radiative rate is much higher than the radiative rate, the quantum yield is close to zero. Due to the impact of the non-radiative rate, the quantum yield shows dependencies on the solvent and concentration. The quantum yields of other processes, such as IC, ISC and phosphorescence, can be defined in a similar way as the ratios of their rates to all other rates. Besides IC and ISC, the RISC is a transition process that cannot be neglected when the energy gap between the singlet and triplet state narrows. This process will be introduced in detail in the next chapter.

## 2.2.4 Excimer formation and properties

For some aromatic compounds, such as pyrene and naphthalene, the fluorescence spectra do not show any vibronic structures in concentrated samples but they show broad and large Stokes-shifted emissions. In such a case, excimers are formed. They are formed by a collision between an excited molecule and an identical unexcited molecule ( $M^* + M = (MM)^*$ )<sup>[64]</sup>. In other words, excimers are dimers in the excited state. The features of excimers are shown in **Figure 2.7**. The lower curve describes the repulsive energy between the two molecules in the ground state. The upper curve represents a minimum energy corresponding to excimer formation where two

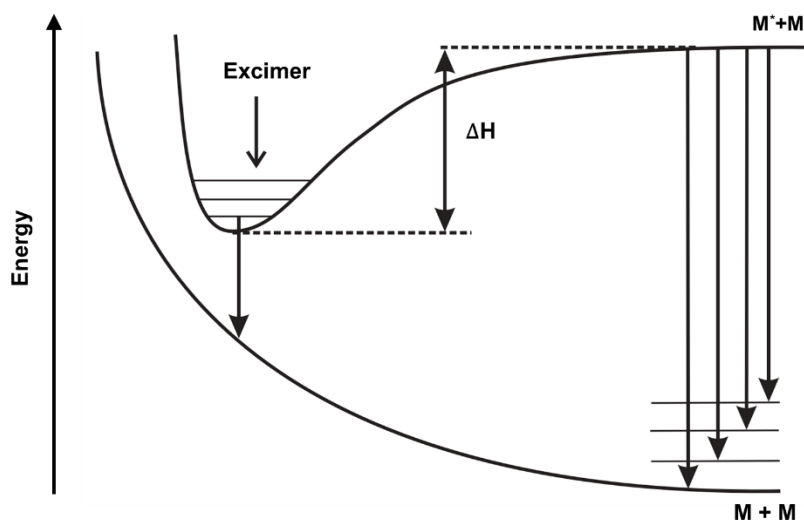


**Figure 2.7** The energy surfaces in the excimer,  $M^*+M$  represents excimer formation.

molecules are at a short distance from each other. In the case of pyrene, the experimental value of the energy minimum at the excited energy surface is ( $\Delta H$ ) is 42 kJ/mol. Compared with the monomer, excimer emission is structure-less, since the lowest energy state is dissociative and can be considered continuous.

For organic light emitting materials, excimer formation will typically decrease the emission quantum yield. Moreover, the FWHM of the emission band is dramatically increased, which decreases the purity of the light. Therefore, the manipulation of excimer formation is of great importance.

## 2.3 The theory of strong exciton-photon coupling

In this section of the thesis, the principle underlying strong exciton-photon coupling is introduced.

### 2.3.1 Different principles of strong exciton-photon coupling

#### Classical description

The simplest way to explain strong exciton-photon coupling is to use the macroscopic analogy. We first consider two undamped harmonic oscillators with masses  $m_1$  and  $m_2$  and their respective spring constants  $k_1$  and  $k_2$ . The two coupled harmonic oscillators with frequencies of  $\omega_1$ ,  $\omega_2$  are coupled together with a spring of constant  $k_3$ <sup>[65]</sup>, as shown in **Figure 2.8**.

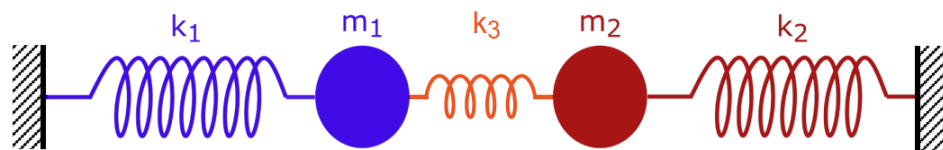


**Figure 2.8** Scheme of two harmonic oscillators coupled together.

According to Newton's second law, the motion of the system can be described by **Equation 2.18**:

$$m_1 \ddot{x}_1 + k_1 x_1 + k_c (x_1 - x_2) = 0 \quad (2.18a)$$

$$m_2 \ddot{x}_2 + k_2 x_2 + k_c (x_1 - x_2) = 0 \quad (2.18b)$$

where  $m$  represents the mass and  $x$  is the force value. After solving **Equation 2.19**, two new modes with two frequencies ( $\omega_+$  and  $\omega_-$ ) of the system are obtained<sup>[65]</sup>,

$$\omega_{\pm} = \frac{1}{2} (\omega_1 + \omega_2 \pm \sqrt{(\omega_1 - \omega_2)^2 + 4\Omega^2}) \quad (2.19)$$

where  $\Omega$  is the split frequency ( $\Omega = k_3/(m_1 m_2 \omega_1 \omega_2)^{1/2}$ ). When the system is at resonance,  $\omega_1 = \omega_2$ , then  $\omega_{\pm} = \omega \pm \Omega$ . The two new modes that arise due to strong coupling are shown in **Figure 2.9**. The detuning represents the difference between the frequencies of oscillators 1 (red) and 2 (blue). This phenomenon has been observed in macroscopic systems such as coupled

springs and acoustic waves.

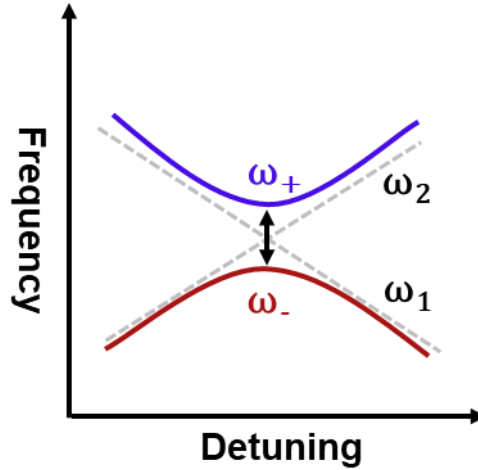


**Figure 2.9** Sketch of the anticrossing behavior of a strongly coupled system, where the detuning is the difference between the frequencies of oscillators 1 (red) and 2 (blue).

### Quantum description

The quantum description of the strong exciton-photon coupling will now be introduced. It is discussed in the framework of cavity (illustrated in **Section 2.3.4**) quantum electrodynamics, where the electromagnetic field and the molecular system are coupled together. A simple system consists of a two-level atom coupled with a single mode of an electromagnetic field. In this case, the model is described by the Jaynes-Cummings Hamiltonian, which was introduced in 1967 and which comprises the sum of the molecule, the electric field, and the molecule-field interaction within the rotating frame approximation<sup>[66]</sup>:

$$\begin{aligned}\hat{H}_{JC} &= \hat{H}_{Mol} + \hat{H}_{Cav} + \hat{H}_{Int} \\ &= \frac{1}{2}\hbar\omega_{Mol}\hat{\sigma}_z + \hbar\omega_{Cav}(\hat{a}^\dagger\hat{a} + \frac{1}{2}) + \hbar g_0(\hat{a}\hat{\sigma}_+ + \hat{a}^\dagger\hat{\sigma}_-)\end{aligned}\quad (2.20)$$

where  $\hat{a}$  and  $\hat{a}^\dagger$  are the creation and annihilation operators for the field mode,  $\hat{\sigma}_z$ ,  $\hat{\sigma}_+$  and  $\hat{\sigma}_-$  are the Pauli matrices for inversion, raising and lowering, respectively. In addition,  $\omega_{Mol}$  and  $\omega_{Cav}$  are the frequencies for the molecular transition and the cavity transition, respectively, and  $g_0$  is the magnitude of the coupling between the molecule and the photon. In this equation, the term  $\hat{a}\hat{\sigma}_+$  represents the transition of the molecule from the ground state to the excited state, while  $\hat{a}^\dagger\hat{\sigma}_-$  represents the reverse process.

In reality, the coupled system contains many molecules, instead of just a single molecule. According to the Tavis-Cummings Hamiltonian<sup>[67]</sup>, the model can be extended to  $N$  molecules. This is achieved using the Holstein-Primakoff transformation<sup>[68]</sup>, which changes the Pauli matrices ( $\hat{\sigma}_z$ ,  $\hat{\sigma}_+$  and  $\hat{\sigma}_-$ ) above into a bosonic operator,  $\hat{b}$ . The collection of the molecular two-level systems now acts as a giant quantum oscillator<sup>[67]</sup>, as shown in **Equation 2.21**,

$$\hat{H} \cong \frac{1}{2}\hbar\omega_{Mol}(-\frac{N}{2} + \hat{b}^\dagger\hat{b})\omega_{Mol}\hat{S}_z + \hbar\omega_{Cav}\hat{a}^\dagger\hat{a} + \hbar g(\hat{a}\hat{b}_+ + \hat{a}^\dagger\hat{b}_-)\quad (2.21)$$

where  $\hat{b}^\dagger$ ,  $\hat{b}_+$  and  $\hat{b}_-$  are bosonic operators, and  $g$  is the collective coupling between  $N$

molecules and one photon. The collective coupling is of great importance and indicates that the strength of the exciton-photon coupling is enhanced by a factor of  $N^{1/2}$ . Therefore, the coupling strength of the system can be enhanced by increasing the molecular concentration.

The Jaynes-Cummings Hamiltonian can yield the two eigenstates of the system through diagonalization<sup>[69]</sup>. The two eigenstates are linear combinations of the light and matter, called polaritons, which can be described by **Equation 2.22**,

$$|P^+\rangle = \alpha|e, 0\rangle + \beta|g, 1\rangle \quad (2.22a)$$

$$|P^-\rangle = \beta|e, 0\rangle - \alpha|g, 1\rangle \quad (2.22b)$$

where  $P^+$  and  $P^-$  are the upper and lower polaritons, and  $|g\rangle$  and  $|e\rangle$  represent the ground and excited state of the molecules, respectively. While  $|0\rangle$ ,  $|1\rangle$  are the numbers of photons in the optical cavity. When the system is in resonance, the energy difference between the  $P^+$  and  $P^-$  is called the vacuum Rabi splitting, and it is expressed as the coupling strength ( $g$ ), as in **Equation (2.23)**:

$$\hbar\Omega_R = 2\hbar g = 2d \sqrt{\frac{\hbar\omega_{Cav}}{2\varepsilon_0 V}} \quad (2.23)$$

where the square root part represents the vacuum electric field inside the cavity.

### 2.3.2 The realization of strong coupling by the optical cavity

Strong exciton-photon coupling can be realized by placing the molecules inside an optical cavity. An optical cavity that contains an arrangement of mirrors forms a standing-wave resonator for electromagnetic waves. Here, we shall constrain our discussion to the simplest case, called a planar cavity, also known as a Fabry–Pérot cavity. It consists of two plane mirrors that are separated by an adjustable length. The mirrors are parallel to each other, so that the light bounces back and forth between the mirrors forming standing waves. As shown in **Figure 2.10**, a commonly used cavity structure for strong coupling with organic materials consists of: (1) a

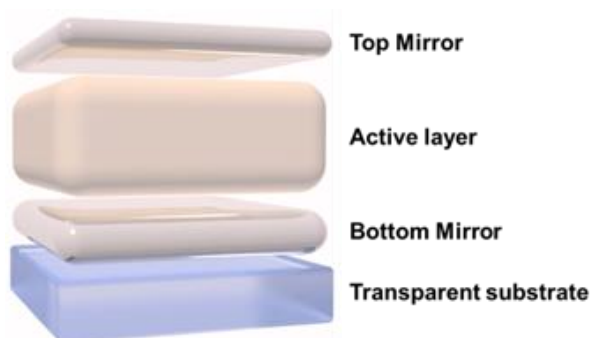


**Figure 2.10** A Typical structure of an optical cavity used for strongly coupled organic materials, comprising (from bottom to top) a transparent substrate, the bottom mirror, the active (organic) layer, and the top mirror.

bottom mirror, which is usually supported by a transparent substrate (e.g., glass, quartz, ZnSe

in the infrared region, etc.); (2) an active layer, which normally consists of thin films of organic materials. It is common to disperse the chromophores within an inert matrix (e.g., polymer), to ensure better film quality and/or to adjust the coupling strength (the coupling strength depends on the chromophore concentration); and (3) a top mirror, which is supported by the active layer. Thus, the thickness of the solid active layer governs the resonance frequency of the cavity. It is also possible to construct cavities using a liquid medium as the active layer. However, this is technologically difficult for electronic transitions due to the nanometric scale of the cavity.

The cavity is on-resonance when the light is in phase after one round trip, giving a maximum for the transmitted light through the cavity. Assuming that there is no light penetration into the cavity mirrors, the resonance condition occurs when the cavity length,  $L_{Cav}$ , is equal to an integer number of intra-cavity half-wavelengths (**Figure 2.11**),

$$L_{Cav} = m \frac{\lambda}{2n} \quad (2.24)$$

where  $\lambda$ ,  $n$  and  $m$  are the wavelength of the light, the refractive index of the material inside the cavity, and an integer number, respectively.

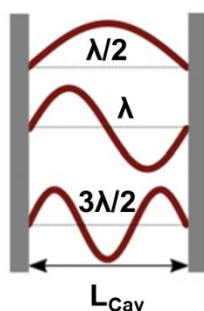


**Figure 2.11** The structure of a Fabry–Pérot cavity. The cavity length  $L_{Cav}$  is equal to an integer number of intra-cavity half-wavelengths ( $l/2$ ) between two mirrors.

The energy dissipation from a cavity (due to absorption, scattering or leakage through the imperfect mirrors) is characterized by the quality factor (Q-factor):

$$Q = \frac{\omega_r}{\Delta\omega_c} \quad (2.25)$$

where  $\omega_r$  and  $\Delta\omega_c$  are the resonant frequency and the linewidth of the cavity mode, respectively. Generally, for reaching the SC regime, the Q-factor should be as high as possible, in order to reduce the energy dissipation from the cavity. However, there is no reason why the Q-factor should be much higher than the linewidth of the molecular transition being coupled. This is because it is the total dissipation from the system (cavity plus molecule) that should be slower than the exchange of energy between the molecules and the cavity. As a rule of thumb, a cavity with a full width at half maximum (FWHM) that is roughly equal to the FWHM of the molecular transition being coupled offers a good compromise between the Q-factor and transparency (the cavity needs to have a finite transparency to be probed).

### 2.3.3 Dispersive behavior

An important property of the hybrid states is their dispersive behavior. The dispersive behavior of the polariton is inherited by the photon contribution, while the molecular transition is non-dispersive (**Figure 2.12**). The coupled harmonic oscillator (CHO) model can be used to simulate the dispersive experimental data for characterizing the system, such as the Rabi splitting  $\hbar\Omega_R$  or the Hopfield coefficients  $|\alpha|^2$  and  $|\beta|^2$  (i.e., the contribution of the photonic or excitonic part to each polariton). The energy of the cavity mode with respect to the angle of incidence ( $\theta$ ) can be expressed using **Equation 2.26**<sup>[70]</sup>,

$$E_{Cav}(\theta) = E_0 \left(1 - \frac{\sin^2 \theta}{n_{eff}^2}\right)^{-\frac{1}{2}} \quad (2.26)$$

where  $E_0$  is the energy of the cavity mode at normal incidence, and  $n_{eff}$  is the effective refractive index.

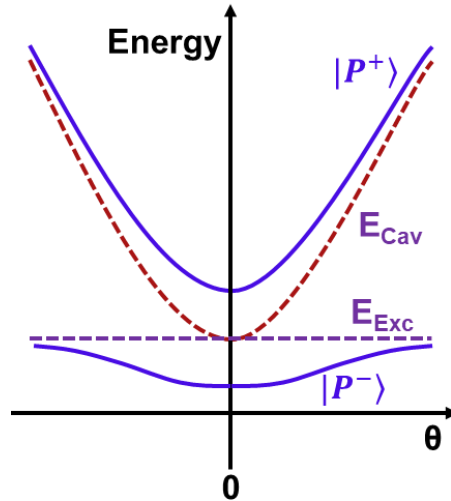


**Figure 2.12** Dispersion of the polaritons (blue,  $P^-$  and  $P^+$ ) at the resonance of the exciton (purple,  $E_{Exc}$ ) and cavity mode (red,  $E_{Cav}$ ).

For a two-level system, a  $2 \times 2$  matrix is used in the CHO model to represent the coupling, as shown in **Equation 2.27**<sup>[71]</sup>,

$$\begin{pmatrix} E_{Cav}(\theta) & \frac{\hbar\Omega_R}{2} \\ \frac{\hbar\Omega_R}{2} & E_{Exc} \end{pmatrix} \begin{pmatrix} \alpha \\ \beta \end{pmatrix} = E \begin{pmatrix} \alpha \\ \beta \end{pmatrix} \quad (2.27)$$

The eigenvalues of the matrix give the energies of the upper polariton  $E^+$  and the lower polariton  $E^-$ , as well as the Hopfield coefficients  $|\alpha|^2$  and  $|\beta|^2$ . Then, the energy dependence on the angle  $\theta$  can be represented by **Equation 2.28**,

$$E^{\pm}(\theta) = \frac{E_{Cav}(\theta) + E_{Exc}}{2} \pm \frac{1}{2} \sqrt{(\hbar\Omega_R)^2 + \Delta(\theta)^2} \quad (2.28)$$

where  $\Delta(\theta)$  is the difference in energy between the cavity mode and the molecular transition. The contribution of the photonic or excitonic part to each polariton, the Hopfield coefficients, can be calculated using **Equation 2.29**,

$$|\alpha|^2 = \frac{1}{2} \left( 1 + \frac{\Delta(\theta)}{\sqrt{(2\hbar g)^2 + \Delta(\theta)^2}} \right) \quad (2.29a)$$

$$|\beta|^2 = \frac{1}{2} \left( 1 - \frac{\Delta(\theta)}{\sqrt{(2\hbar g)^2 + \Delta(\theta)^2}} \right) \quad (2.29b)$$

In the resonant case, the energy of the cavity mode is isoenergetic with the energy of the molecular transition, and both parts contribute half to each polariton. This contribution varies with the detuning between the exciton and photon energies. In addition, the polariton can be easily adjusted between the different contributions by varying the number of molecules. For thicker cavities, the energy of the cavity mode is reduced. If the energy of the cavity is lower than the molecular transition, the photon contribution to the lower polariton increases, whereas the contribution to the upper polariton decreases. Such a system is called red-detuned<sup>[72]</sup>. For the opposite case of a blue-detuned system, the energy of the cavity mode is higher than the energy of the molecular transition. The values of the Hopfield coefficients can be represented as a function of the angle of incidence ( $\theta$ ) (**Figure 2.13**).

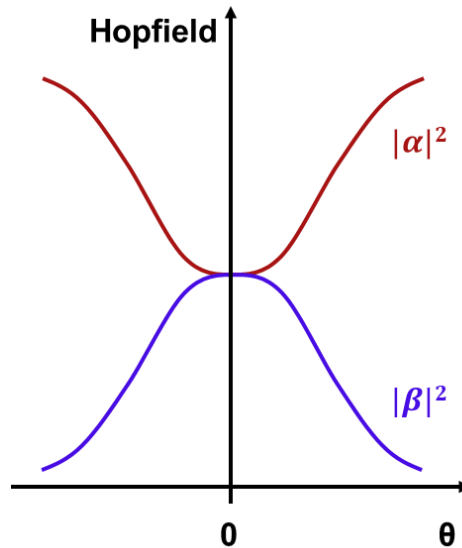


**Figure 2.13** Hopfield coefficients to the polariton dispersion.

### 2.3.4 Strong coupling limit

At resonance, the relative strength of the coupling is controlled by three parameters: the photon decay rate of the cavity,  $\kappa$ ; the non-resonant decay rate of the molecule,  $\gamma$ ; and the coupling

strength,  $g$ . When  $g \ll (\kappa, \gamma)$ , the system is in the weak coupling regime. Conversely, when  $g \gg (\kappa, \gamma)$ , the system is in the strong coupling regime. In the strongly coupled regime, the interaction of light with matter is faster than the dissipation process. Therefore, the molecule interacts coherently with the cavity and can emit and reabsorb cavity photons multiple times before the cavity photons are lost<sup>[73, 74]</sup>. In other words, the polaritons emerge in the system. Both  $\kappa$  and  $\gamma$  are related to experimentally measurable parameters. They are the linewidth of the cavity and the linewidth of the molecular absorption band, respectively. When the splitting (at resonance) is larger than two dissipation factors, i.e.,  $2g > (\gamma + \kappa)/2$ , it is assumed that the system is in the strong coupling regime. The shift from weak to strong coupling occurs when both polarization branches are spectrally resolved, i.e., the splitting ( $\Omega_R$ ) must be larger than the FWHM of the cavity mode ( $\Delta\omega_c$ ) and the bare molecular absorption ( $\Delta\omega_x$ ). The **Equation 2.30** is shown below,

$$\Omega_R = \frac{\Delta\omega_x + \Delta\omega_c}{2} \quad (2.30)$$

However, the criterion described above is not sufficient to ensure that the system is in the strong coupling regime. In the weak coupling regime, splitting can, for example, occur for other reasons. In order to visualize the anti-crossing between the exciton and cavity modes, the dispersive nature of the polaritonic states should always be characterized, as shown in **Figure 2.14**.

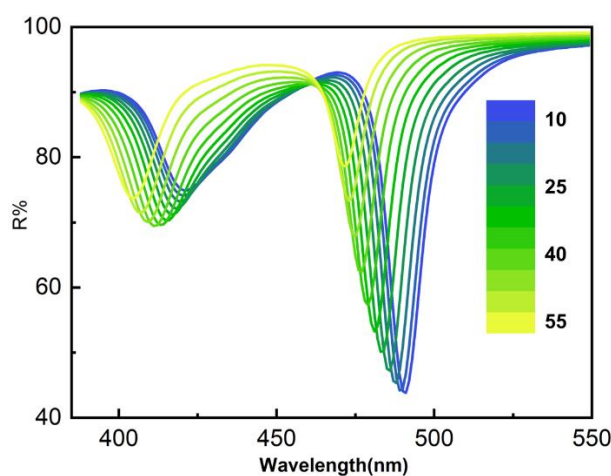


**Figure 2.14** Angle resolved reflectance spectra of dyes inside the optical cavity.

## 2.4 Exciton-exciton coupling in molecular aggregates

Exciton-photon coupling has been introduced above. Let's turn our attention now to excitonic coupling through Coulombic interactions in molecular aggregates.

### 2.4.1 The Kasha Theory for aggregates

Seven decades ago, Kasha showed that molecular dimers that are stacked “head-to-tail” exhibit red-shift absorption and an enhanced radiative decay rate, whereas dimers that are stacked “side-by-side” exhibit a blue-shift absorption and a suppressed decay rate<sup>[75, 76]</sup>. We call these two forms J- and H-aggregates, respectively. Thereafter, the Frenkel exciton theory was

developed to study these two types of aggregates. In this theory, the interaction between the molecules is called the Coulombic intermolecular coupling<sup>[32]</sup>,  $J_c$ . This type of interaction has significant effects on the photophysical properties of the molecules. In **Figure 2.15**, the simplest case of the molecular dimer is depicted, where the Coulombic coupling  $J_c$  gives rise to the formation of two delocalized states that are split by  $2|J_c|$ . The two delocalized levels consist of in-phase and out-of-phase linear combinations of two local excited states. The in-phase or symmetric state is characterized by an enhanced transition dipole moment, while the transition dipole moment of the out-of-phase state is lower than that of the monomer. Meanwhile, in J-aggregates, the negative coupling ( $J_c < 0$ ) results in the symmetric state having a lower energy than the monomer or antisymmetric state. In contrast, in H-aggregates with  $J_c > 0$ , the ordering is reversed.

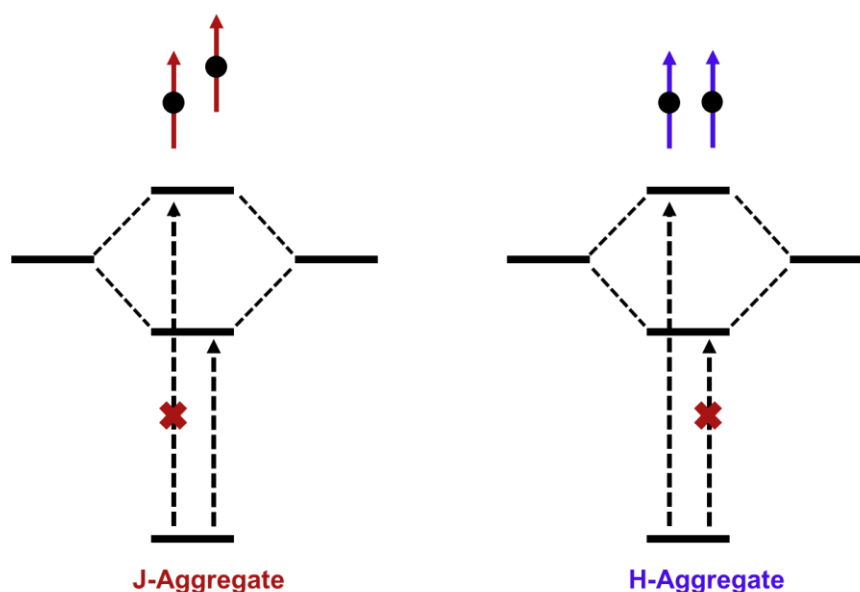


**Figure 2.15** Energy level diagrams for the J-aggregate and H-aggregate dimers. Transition is allowed only to the symmetric state (decreased energy difference in the J-aggregates and increased energy difference in the H-aggregates, as compared to the monomers.).

According to the previous theory<sup>[77]</sup>, two important values, exciton bandwidth ( $W$ ) and nuclear relaxation energy ( $S\omega_{\text{vib}}$ ), are described so as to gain quantitative structural insights into the nature of the aggregates. As for the exciton bandwidth, the free exciton bandwidth for the linear aggregates is defined by **Equation 2.31**,

$$W = |J_{k=0} - J_{k=\pi}| \quad (2.31)$$

where  $J_k$  is the  $k$ -dependent (Fourier) component of the Coulombic coupling. When only the nearest neighbor (n,n.) coupling  $J_c$  is retained, then  $J_k$  can be calculated following the **Equation 2.32**,

$$J_k = 2J_c \cos(k) \quad (2.32)$$

which is a reasonable approximation for linear aggregates. Then, the calculation of  $W$  is simplified to **Equation 2.33**<sup>[33]</sup>,

$$W = 4|J_c| \quad (2.33)$$

The  $J_c$  can be calculated as half the energy difference between the 0-0 absorptions ( $A_{0-0}$ ) of the monomer and the aggregates, as shown in **Figure 2.16**.

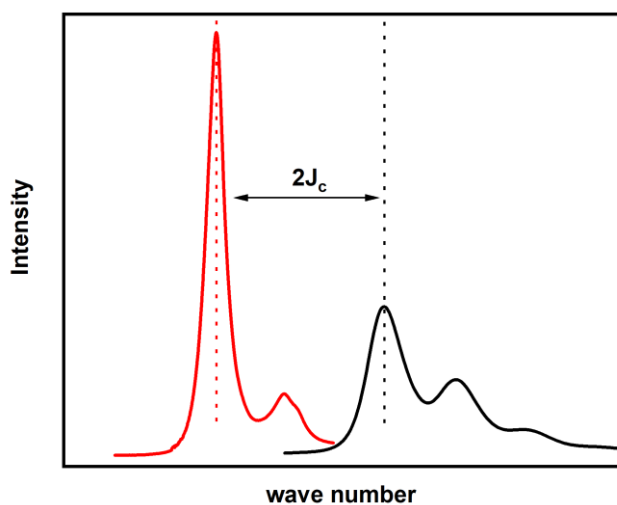


**Figure 2.16** The value of the Coulombic intermolecular coupling shown by absorption spectra of the J-aggregate (red) and monomer (black).

Regarding to the nuclear relaxation energy ( $S\omega_{\text{vib}}$ )<sup>[78]</sup>, it is the quantity of energy released when the molecule relaxes to the minimum excited state potential after molecular absorption. Here,  $S$  is the Huang-Rhys (HR) factor that describes the potential difference between the ground and excited states<sup>[79]</sup>. It can be seen as a quantification of the relative shift between the ground and excited state potentials, and it can be calculated as the ratio of the  $I_{0-0}$  to  $I_{0-1}$  intensities for the monomer emissions. Furthermore,  $\omega_{\text{vib}}$  is the vibrational frequency, which can be calculated as the difference in energy between  $A_{0-1}$  and  $A_{0-0}$ . The Harmonic nuclear potential wells for the ground and excited states are portrayed in **Figure 2.17**.

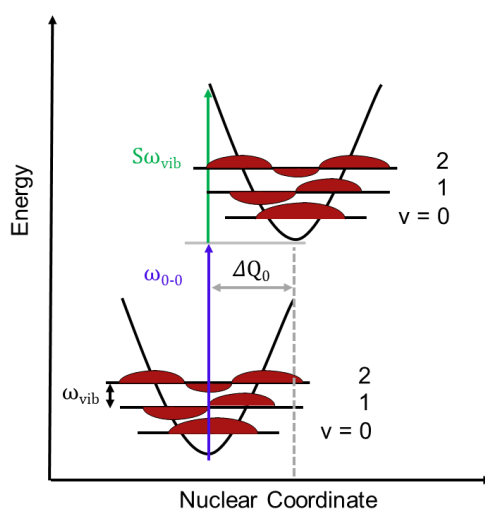


**Figure 2.17** Harmonic nuclear potential wells for the ground and excited states. The  $\Delta Q_0$  term represents the potential difference between the excited and ground states;  $\omega_{\text{vib}}$  is the vibrational energy, and  $S\omega_{\text{vib}}$  represents the relaxation energy ( $S$  is the Huang-Rhys factor).

When  $W \ll S\omega_{\text{vib}}$ , the system is in the weak excitonic coupling regime. As the bandwidth  $W$  increases, the system goes to the intermediate exciton coupling regime. If the exciton bandwidth continues to increase, when  $W \gg S\omega_{\text{vib}}$ , the system is in the strong excitonic coupling regime. Another important value for the aggregates is the coherence number ( $N$ ), which is also known as the excitonic delocalization length<sup>[80]</sup>. It describes the number of chromophores over which the states are coherently delocalized. It has been shown that the linewidth correlation between monomer and J-aggregate follows a square root dependence on  $N$ . Furthermore, to minimize the influence of higher vibrational modes on the linewidth of the emission or absorption, the full width at two thirds maximum ( $\text{FW}_{2/3M}$ ) of the monomer and J-aggregate emissions can be used to determine  $N$ <sup>[81]</sup>,

$$N = \left( \frac{\text{FW}_{2/3M_{\text{mon}}}}{\text{FW}_{2/3M_{\text{agg}}}} \right)^2 \quad (2.34)$$

## 2.4.2 Photophysical properties of the aggregates

As aggregates are formed, both the absorption and emission spectra will shift. Moreover, the molecular transition dynamics will change. The variation will be shown below.

**Figure 2.18a, b** and **c** represent the transitions of the monomer, J-aggregates, and H-aggregates between the ground and excited state, respectively. Meanwhile, the 0-x absorption ( $A_{0-x}$ ) and 0-x emission (here,  $x = 0, 1$  or  $2$ , namely  $I_{0-x}$ ) are the absorptions and emission in different vibrational modes, respectively. The monomer shows three vibronic peaks in both the absorption and emission processes. As for the absorption spectrum of J-aggregates, it is red-shifted (the energy gap between two states decreases) and narrower than the one of monomer. The narrow band width is due to the increase of the coherence number of the aggregates<sup>[33]</sup>. In addition, less vibrational component is seen in the J-aggregates, which means that the new delocalized states have less vibrational transitions. This is because the delocalized excited state

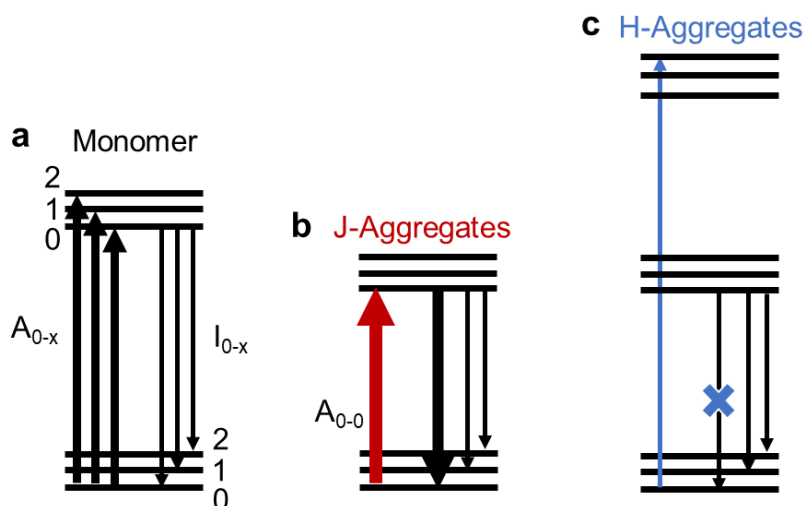


**Figure 2.18** Jablonski diagram of the absorptions and emissions for the monomer (**a**), J-aggregates (**b**) and H-aggregates (**c**), and the  $A_{0-x}$  and  $I_{0-x}$  ( $x = 0, 1$  or  $2$ ) represent the absorptions and emissions in different vibrational modes.

is more ground state like. Finally, the intensity of the absorption is strongly enhanced due to the increase of the transition dipole moment. Regarding the emission spectrum, the intensity of  $I_{0-0}$  will also be increased and narrowed. As shown in **Figure 2.18b**, the thick red and black arrows represent the  $A_{0-0}$  and  $I_{0-0}$ , respectively. Their lengths are very similar to each other. This indicates that the energy difference between the absorption and emission is smaller than the case in monomer. Therefore, the Stokes shift in the J-aggregates will be very small or even negligible. The reduced Stokes shift is due to the decreased reorganization energy ( $\lambda$ ), which will be discussed further in the next chapter.

In contrast, compared with **Figure 2.18a&c**, less vibrational component is observed in the H-aggregates than that of the monomer. However, the absorption of the H-aggregates is blue-shift due to the increase of the transition energy. As for the emission, the greatest degree of attenuation of the radiative component is seen for the  $I_{0-0}$ . This is because, in the ideal H-aggregate, the  $I_{0-0}$  is strictly forbidden due to the cancellation of the dipole moment in the band bottom state<sup>[31]</sup>. In ideal H-aggregates, the highest energy component of the emission spectrum is, therefore, the  $I_{0-1}$ . Thus, the Stokes shift in H-aggregates is larger than in the cases of the monomer and J-aggregates.

As mentioned in **Section 2.2.3**, the transition rate and quantum yield are the key values describing the molecular photoluminescence. In J-aggregates, the radiative rate of the J-aggregates is always higher than that of the monomer, so-called superradiance<sup>[82]</sup>. This effect has a simple classical interpretation: with a collection of oscillators, their amplitudes add up coherently to form a large effective dipole. As there is extension of the exciton, the size of the dipole moment is restricted to the coherence number. Thus, the radiative rate should be strongly increased, being inversely proportional to the coherence number. Besides the radiative rate, the quantum yield depends on the non-radiative rate as well. The emission quantum yield and non-radiative rate will be discussed in detail in the next chapter.



## **3. Strong exciton-photon and exciton-exciton coupling and its effects on molecular photophysics**

In this chapter, firstly, the transition dynamics starting from the molecular triplet state is introduced. Secondly, the experimental observations of the effect of strong exciton-photon on molecular photophysics is described and discussed. Thirdly, the non-radiative rate in different coupling regimes is described by considering the energy gap law. Finally, the experimental and theoretical result of the exciton-exciton coupling on the molecular near-infrared emission is shown and analyzed.

### **3.1 Transition dynamics starting from triplet states**

Molecular transition dynamics were outlined in the previous chapter. However, most of the cases discussed involved transitions between different singlet or vibrational states. Here, we focus on the dynamics starting from the triplet state. Knowledge regarding the reverse intersystem crossing is introduced, as well as thermally activated delayed fluorescence (TADF) molecules.

#### **3.1.1 Thermally activated delayed fluorescence and reverse intersystem crossing**

In an optically pumped luminescent system, all the excited molecules will migrate to higher energy-level singlet states. However, the excited singlet and triplet states are formed in a 1:3 ratio in electrically pumped light emitting systems. The difference is due to the spin statistics<sup>[83]</sup>. Given the low radiative rate constant of triplet states<sup>[52]</sup>, they represent an energy loss channel to hinder the development of highly efficient organic light-emitting diodes (OLEDs). A common approach to counteract this limitation is to use heavy metal complexes. In this way, the radiative decay of the triplet state is enabled by the enhanced SOC, whereby the heavy atom effect leads to sufficient mixing of the singlet and triplet states. As a result, the complex structure can allow internal quantum efficiencies of OLED devices to reach 100% theoretically. Nonetheless, they also show several major disadvantages when used in OLEDs: (1) the

complexes are unstable, especially in the blue light-emitting region; (2) the metals are expensive and likely toxic. Therefore, they are unsuitable considering the high production output.

Before Adachi investigated thermally activated delayed fluorescence (TADF), it was firstly rationalized by Perrin almost 90 years ago. Nowadays, this relatively well-known mechanism is proposed as a strategy to harvest non-emissive triplet excited states in OLEDs. Molecules with TADF performances always have small energy difference between the lowest singlet and triplet states. Hence, the reverse intersystem crossing (RISC) is likely to occur between the excited singlet and triplet states (shown in **Figure 2.5**). In practice, the rate of RISC is large enough to compete with the non-radiative decay from the triplet. Harvesting efficiencies for the triplet can be realized in different emitting regions. The small energy gap between the  $S_1$  and  $T_1$  is accomplished by molecular design. Broadly speaking, a small energy gap is achieved by separating the HOMO and LUMO orbitals in space. To achieve this separation, these molecules have covalently linked electron donor (D) and acceptor (A) units. Although small energy gap seems easy to achieve, minimizing internal conversion and obtaining a high quantum yield of the emission are not simple tasks. This is because the overall performance is influenced by many factors, such as the dielectric medium, molecular geometry, the presence of low-energy, triplet excited states and localization in the donor or acceptor units. The D-A structure leads to a strong charge transfer between the two states, which gives rise to a relatively small overlap between the HOMO and LUMO frontier orbitals. In addition, it decreases the electronic exchange energy to realize small energy gap as well.

### 3.1.2 Two types of TADF emitters

#### Donor-Acceptor TADF emitters

Efficient TADF molecules should satisfy the condition of a small energy gap ( $\Delta E_{ST}$ ) between the excited singlet and triplet states. Then, the RISC can outcompete the non-radiative process to harvest the triplet-emitting channel, which will enhance the emission quantum yield. Therefore, the small value of  $\Delta E_{ST}$  is essential to facilitate the RISC rate given by the Arrhenius equation,

$$k_{RISC} = A \cdot \exp\left(\frac{-\Delta E_{ST}}{k_B T}\right) \quad (3.1)$$

where  $k_{RISC}$  is the RISC rate constant,  $T$  is the temperature,  $k_B$  is the Boltzmann factor, and  $\Delta E_{ST}$  is the energy barrier between the triplet and singlet states. Three different aspects are usually considered when calculating the energies of the excited singlet and triplet states<sup>[84]</sup>: (1) the electron repulsion energy ( $K$ ), which is the first order correction of the Coulombic interaction; (2) the orbital energy ( $E_{orb}$ ) that is associated with the one-electron orbital for a fixed nuclear framework in the excited state; (3) the exchange energy ( $J$ ), which represents the first-order quantum-mechanical correction, including the Pauli principle, and affects the two unpaired electrons in the excited state (one electron in the HOMO and the other in the LUMO). The three components contribute to the energies of both the singlet and triplet states. However, due to the different spin arrangements of the singlet and triplet excited states, the exchange energy  $J$  increases the energy in the singlet state and decreases the energy in the triplet state by the same amount, based on **Equations (3.2a)** and **(3.2b)**. The energy gap is therefore described by **Equation 3.2c**,

$$E_S = K + E_{orb} + J \quad (3.2a)$$

$$E_T = K + E_{orb} - J \quad (3.2b)$$

$$\Delta E_{ST} = E_S - E_T = 2J \quad (3.2c)$$

Based on **Equation 3.2c**, it is clear that decreasing the singlet-triplet energy gap requires minimization of the exchange energy  $J$ , which is calculated using **Equation 3.3**<sup>[85, 86]</sup>,

$$J = \iint \varphi(r_1) \psi(r_2) \left( \frac{e^2}{r_1 - r_2} \right) \varphi(r_2) \psi(r_1) dr_1 dr_2 \quad (3.3)$$

where  $\varphi$  and  $\psi$  represent the HOMO and LUMO wave functions, respectively, and  $e$  is the charge of the electron. This equation indicates that  $J$  can be decreased by minimizing the overlap between the HOMO and LUMO. This can, in a first approximation, be achieved by spatially separating the two frontier orbitals. When the molecules contain donor and acceptor units that are linked via an aromatic bridge, spatial separation of the frontier orbitals will occur and give rise to strong charge transfer transitions. Furthermore, the singlet and triplet energy splitting values can be decreased further by twisting the donor and acceptor moieties around the D-A axis, so as to obtain relative orientation near-orthogonality. Additionally, this can be accomplished by increasing the distance between the two units. The most commonly-used electron donor and acceptor units for TADF molecules are shown in **Figure 3.1**.

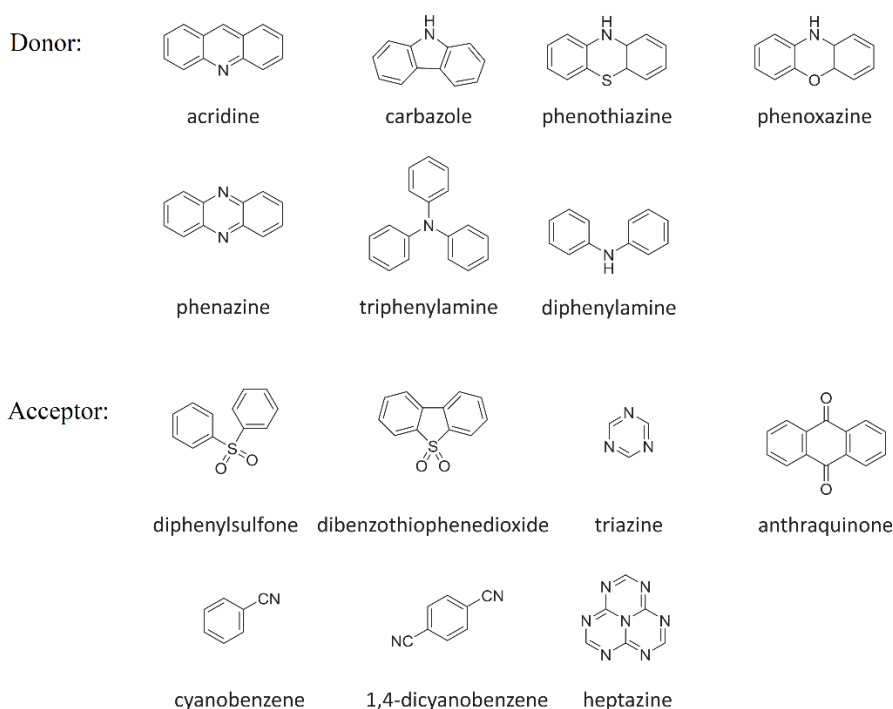


**Figure 3.1** Typical donor and acceptor units in TADF molecules.

### Multiple resonance TADF emitters

Due to their harvesting of the triplet emitting channel, the organic TADF molecules can ideally achieve 100% internal quantum efficiency even when electrically excited. However, the emission color purity needs to be taken into account as well (a small emission FWHM is

favorable). In general, the spectral FWHMs of the emitters are controlled by the structure distortion (SD) between the ground and excited states<sup>[87]</sup>. As the degree of SD increases during the electrical transition (**Figure 3.2a**), more vibronic transitions are generated by vibrational modes strongly coupled with the structural changes, leading to a large excited state reorganization energy. This results in a larger FWHM (**Figure 3.2c**). In contrast, when the degree of SD is minimized, the FWHM is decreased (**Figure 3.2b**). Meanwhile, the Stokes shift is strongly associated with the sum of the ground and excited-state reorganization energies ( $\lambda_M$  and  $\lambda_M^*$ ). Therefore, an increase in SD is assumed to give rise to a larger Stokes shift as well.

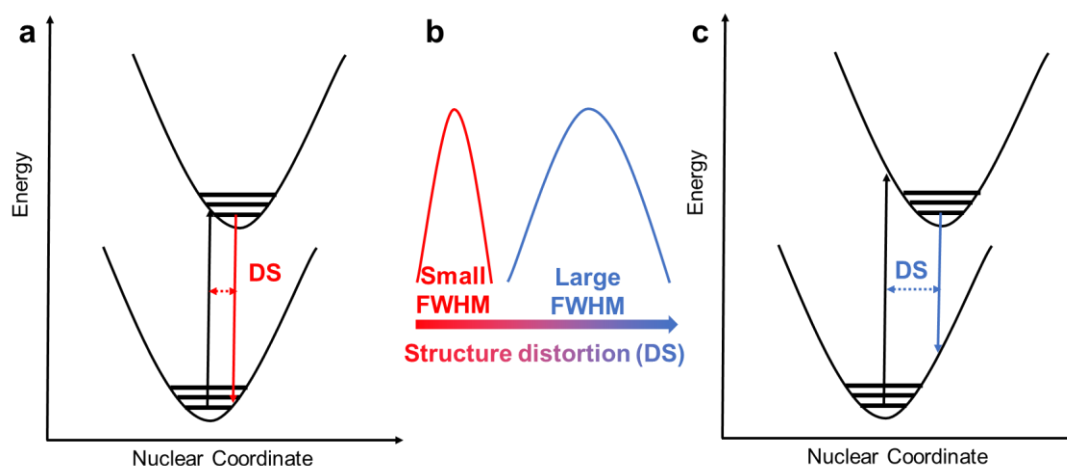


**Figure 3.2** Schematic representation of the basic design principle for broad and narrow band emissions.

In TADF molecules with D-A structures, as the spatial separation of HOMO-LUMO increases, the degree of SD increases. Consequently, it results in a large FWHM and Stokes shift, which affects the light purity.

In order to tackle the problem outlined above, a TADF molecular design strategy based on the multiple resonance effect was proposed in 2016<sup>[88]</sup>.

Through the new strategy, electron-withdrawing boron atoms are in a fused polycyclic aromatic skeleton, with electron-donating nitrogen atoms in the ortho position. The atomic arrangement induces the localization of the HOMO and LUMO wave functions at different type of atoms (**Figure 3.3**). More specifically, the HOMO is localized primarily to the electron-donating atoms (nitrogen atoms) and their ortho-/para-positioned carbon atoms, whereas the LUMO is distributed to the electron-withdrawing boron atoms and its ortho-/para-positioned carbon atoms.

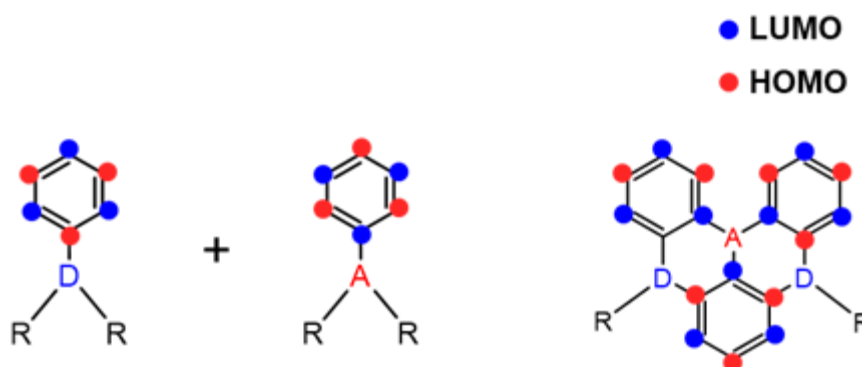


**Figure 3.3** HOMO-LUMO separation by multiple resonance effect

Therefore, the spatial separation of HOMO and LUMO can be achieved without depending on donor-acceptor structures. Based on this distinct multiple resonance effect, the bonding/antibonding features between adjacent atoms are weakened. Moreover, the structural relaxation and vibronic coupling are decreased due to the resulting nonbonding orbitals. Accordingly, this strategy enables small Stokes shifts and FWHMs, as well as a small  $\Delta E_{ST}$ . Commonly used multiple-resonance TADF molecules are shown in **Figure 3.4**.

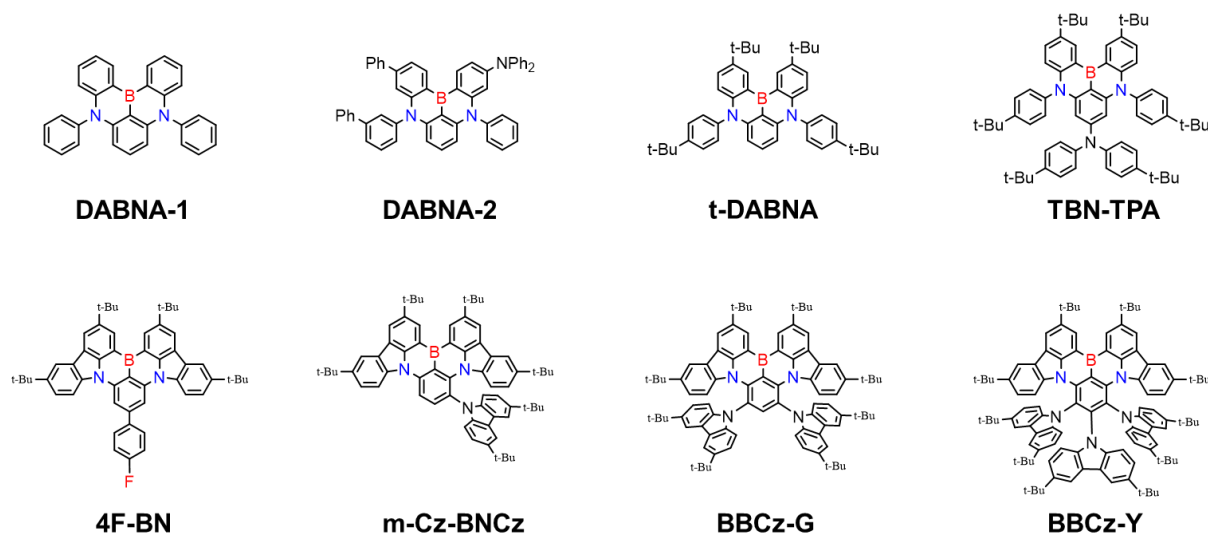


**Figure 3.4** Conventional MR TADF molecules (Boron represents the acceptor in red color, while nitrogen is the donor in blue color)<sup>[89]</sup>.

### 3.1.3 The effects of spin-orbit coupling and the inverted system

Based on the above, a small  $\Delta E_{ST}$  can facilitate efficient reverse intersystem crossing. However, an extremely small  $\Delta E_{ST}$  (close to zero) may not generate a satisfactory rate of RISC. This is due to a limitation of SOC. Actually, the rate of the RISC can be studied following the Marcus electron-transfer theory. The rate can be expressed as<sup>[90]</sup>,

$$k_{RISC} = \frac{2\pi}{\hbar} |\langle S_1 | H_{SO} | T_1 \rangle|^2 \frac{1}{\sqrt{4\pi\lambda_M k_B T}} \sum_{n=0}^{\infty} e^{-S} \frac{S^n}{n!} \exp\left[-\frac{(\Delta E_{ST} + \lambda_M + n\hbar\omega_{eff})^2}{4\pi\lambda_M k_B T}\right] \quad (3.4)$$

where  $\lambda_M$  is the molecular reorganization energy about the intramolecular and intermolecular low-frequency vibrations<sup>[91]</sup>,  $\langle S_1 | H_{SO} | T_1 \rangle$  represents the spin orbit coupling (SOC) matrix element between the singlet and triplet states,  $k_B$  is the Boltzmann constant,  $T$  represents the temperature,  $\hbar\omega$  is the effective energy of a mode showing the relevant non-classical high-frequency intramolecular vibrations<sup>[92]</sup>, and  $S$  is the Huang-Rhys factor. The equation is very similar to the description of charge transport in organic semiconductors, in which the electronic coupling is replaced by SOC. This equation emphasizes that SOC is crucial for the rate of RISC,

as well as the small energy gap. It should be noted that an increase of SOC by one order of magnitude results in a two orders of magnitude increase in the RISC rate.

If the  $\Delta E_{ST}$  is very small due to the large spatial separation of the HOMO and LUMO, the SOC tends to vanish. This is because the spin-orbit operator acts on both the spin magnetic quantum number of the electron and its spatial angular momentum quantum number. Then, the SOCs with the same spatial orbital occupation are formally zero, since any change in spin cannot be compensated by a corresponding change in the orbital angular momentum. Therefore, when designing a TADF molecule, we can only balance the effects of SOC and the energy gap, and this hinders the development of efficient OLED devices.

One strategy to overcome this limitation is to design an inverted singlet and triplet system. Miyajima et al. discover a molecule disobeying Hund's rule with a negative  $\Delta E_{ST}$ <sup>[93]</sup>. The mechanism behind the negative  $\Delta E_{ST}$  is that the molecule is in a double-excitation configurations in which two electrons of occupied orbitals have been promoted out to virtual orbitals<sup>[94-98]</sup>. The effective admixture of such configurations stabilizes the singlet state. However, given the Pauli exclusion principle, the triplet state cannot undergo this stabilization. Considering this difference, the  $\Delta E_{ST}$  could be negative. The structure of the molecule and its transition dynamics are shown in **Figure 3.6**.

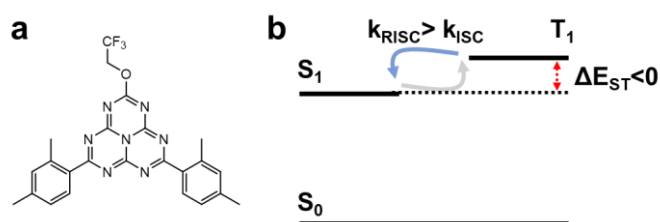


**Figure 3.5** (a) The structure of the singlet-triplet inverted molecule; (b) the transition dynamics of the inverted molecule.

As for the experimental result of the singlet-triplet inverted molecule, the delayed lifetime increases as the temperature increases, which has never been observed in any pure organic system. Applying an Arrhenius type of analysis, the RISC rate decreases as the temperature decreases. This indicates that the RISC is not a thermally activated transition. Moreover, it is the first time in a pure organic system that the RISC rate is higher than the ISC rate, due to the inverted singlet and triplet states.

One limitation of the inverted system is that the oscillator strength of the  $S_1$ - $S_0$  transition in the energy-inverted molecule is low ( $f = 0.01$ ). Although RISC is very fast, the small value of  $f$  has a negative effect on the external quantum efficiency of the material. Nonetheless, inverted systems are of great importance for the development of efficient OLEDs.

### 3.1.4 Fundamental understanding of the transition dynamics of the TADF process

Time-resolved measurements are widely used to study the complex photophysics of TADF processes. Upon light excitation, prompt fluorescence (PF) is seen at first. PF results from the radiative decay of the singlet excited states (**Figure 3.6**), which occurs within a few nanoseconds. Thereafter, an emission tail appears due to delayed fluorescence (DF).

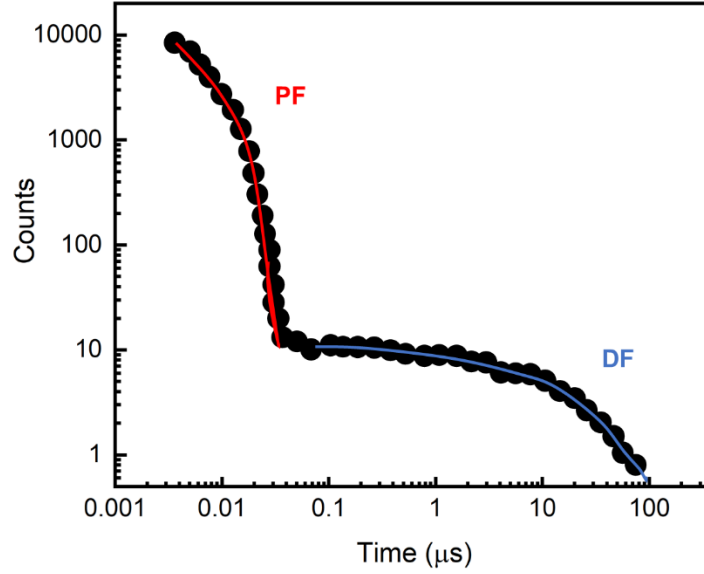


**Figure 3.6** Fluorescence decay of the DABNA-2 (one TADF molecule)<sup>[88]</sup>. The blue and red lines represent the prompt and delayed fluorescence, respectively.

The rates of intersystem crossing ( $k_{ISC}$ ) and reverse intersystem crossing ( $k_{RISC}$ ) are key parameters to determine the equilibrium between singlet and triplet states. A strong emission yield of TADF results from a high  $k_{ISC}$  that facilitates triplet formation, as well as a high  $k_{RISC}$  that competes with other decay processes. The yield of triplet formation,  $\Phi_{RISC}$ , can be described by the equation below<sup>[99]</sup>,

$$\Phi_{RISC} = \frac{k_{RISC}}{k_{RISC} + k_{IC}^T + k_{PH}} \quad (3.5)$$

where  $k_{IC}^T$  and  $k_{PH}$  represent the rates of internal conversion from the triplet state and phosphorescence, respectively.

After considering the  $\Phi_{RISC}$ , we continue to study the rate of RISC. According to the previous literature, the  $k_{RISC}$  can be described by the equation below<sup>[100]</sup>,

$$k_{RISC} = \frac{1}{\tau_{DF}} \frac{k_{RISC}}{1 - \Phi_{ISC}\Phi_{RISC}} \quad (3.6)$$

where  $\tau_{DF}$  is the lifetime of DF, and  $\Phi_{ISC}$  represents the yield of ISC from the excited singlet state to the triplet state. When  $k_{RISC}$  is much greater than  $k_{IC}^T$  and  $k_{PH}$ , **Equation 3.6** can be simplified,

$$k_{RISC} = \frac{1}{\tau_{DF}} \frac{1}{1 - \Phi_{ISC}} \quad (3.7)$$

The lifetime of DF can easily be measured. Hence, the challenge becomes how to obtain the yield of ISC. The value of  $\Phi_{ISC}$  is related to quantum yields of the PF ( $\Phi_{PF}$ ) and DF ( $\Phi_{DF}$ ). When  $\Phi_{DF}/\Phi_{PF}$  is  $\geq 4$ , as well as  $\Phi_{RISC} \approx 1$ , the photophysical characterization of the transition dynamics is greatly simplified, as the equation below<sup>[101]</sup>,

$$\Phi_{ISC} = \frac{\Phi_{DF}}{\Phi_{PF} + \Phi_{DF}} \quad (3.8)$$

By inserting **Equation 3.8** into **3.6**, the  $k_{RISC}$  can be obtained following **Equation 3.9**,

$$k_{RISC} = \frac{1}{\tau_{DF}} \frac{\Phi_{PF} + \Phi_{DF}}{\Phi_{PF}} \quad (3.9)$$

Equation 3.9 has been used to analyze  $k_{RISC}$ . In some cases, the requirements (for  $\Phi_{RISC}$  and  $\Phi_{DF}/\Phi_{PF}$ ) cannot be satisfied. The  $\Phi_{DF}/\Phi_{PF}$  can be very low if the rate of intersystem crossing ( $k_{ISC}$ ) is not sufficiently high compared with  $k_{PF}$ . Taking the DABNA-2 molecule<sup>[88]</sup> as an example, the  $k_{ISC}$  is about one-tenth of the  $k_{PF}$ , which results in the low value of  $\Phi_{DF}/\Phi_{PF}$  (<0.1). In addition, when the sample is at high concentration, the  $k_{IC}^T$  cannot be ignored. The condition for  $\Phi_{RISC}$  is not matched due to the non-negligible  $k_{IC}^T$ . Accordingly, the simplified equation cannot be used in many cases.

Alternatively, temperature-dependent measurements can help with the analysis. These measurements are essential to prove that the DF results from the thermally activated process. In this case, the DF will be enhanced as the temperature increases. **Figure 3.7** shows the features of the temperature-dependent measurements for the lifetimes of DABNA-2. The lifetime of the DF decreases drastically when the temperature increases from 77 K to 200 K.

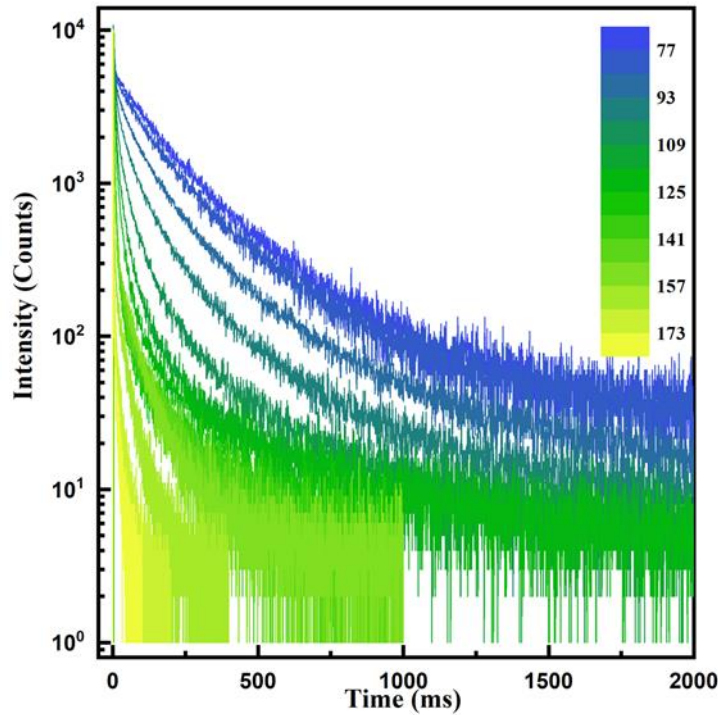


**Figure 3.7** The temperature-dependent fluorescence decay of a TADF molecule.

As the temperature changes, the calculation of the  $k_{RISC}$  can use the equation below<sup>[102]</sup>,

$$k_{RISC}(T) = \frac{k_{PF}}{k_{ISC}} \frac{k_{DF}(T) \cdot \Phi_{DF}(T)}{\Phi_{PF}(T)} \quad (3.10)$$

where  $k_{PF}$  and  $k_{DF}$  are the prompt and delayed fluorescence rate constants, respectively. The  $k_{PF}$  and  $k_{ISC}$  parameters are temperature-independent, while  $k_{DF}$ ,  $\Phi_{DF}$  and  $\Phi_{PF}$  are temperature-dependent. In addition, both the DF and PF quantum yields are proportional to the integrated emissive intensities. The  $k_{DF}$  can be represented as  $\tau_{DF}$ , according to the following expressions:

$$\Phi_{DF}(T) \propto I_{DF}(T) \quad (3.11a)$$

$$\Phi_{PF}(T) \propto I_{PF}(T) \quad (3.11b)$$

$$k_{DF} = \frac{1}{\tau_{DF}} \quad (3.11c)$$

where  $I_{DF}$  and  $I_{PF}$  represent the intensities of DF and PF, respectively. By integrating **Equation 3.11** into **3.10**, the following relationship can be used,

$$k_{RISC}(T) \propto \frac{I_{DF}(T)}{I_{PF}(T) \cdot \tau_{DF}(T)} \quad (3.12)$$

After obtaining the value of  $k_{RISC}$ , the  $\Delta E_{ST}$  associated with TADF can be calculated following the Arrhenius equation. Thus, the  $\Delta E_{ST}$  can be obtained through temperature-dependent measurements.

## 3.2 Barrier-free reverse-intersystem crossing by strong light-matter coupling in TADF molecules

In **Section 3.1**, it was proposed that an inverted singlet-triplet system facilitates the triplet emitting channel. In addition, a new molecule has been shown to violate Hund's rule with a negative  $\Delta E_{ST}$ . Here, I will discuss the results from **Paper I** in which an inverted singlet-triplet system is realized by strong light-matter coupling.

Five TADF molecules were selected in an initial screening process as state-inversion candidates: 3DPyM-pDTC, a boron difluoride curcuminoid derivative (BDC)<sup>[103]</sup>, DABNA-1, DABNA-2<sup>[104]</sup> and TBN-TPA<sup>[105]</sup> (structures are shown in **Figure 3.8**). The first two of them are D-A TADF molecules, while the last three are multiple resonance TADF molecules. All the candidates have small energy gaps  $\Delta E_{ST}$ . For the screening, firstly, the optical properties of the five molecules were characterized. Then, the five molecules were placed between two Ag mirrors to form Fabry-Pérot cavities, and basic optical measurements were performed. Finally, BDC and DABNA-2 were chosen as the representative for D-A and multiple resonance TADFs, respectively. The reason why they were selected is that they have high Rabi splitting due to a high transition dipole moment. Additionally, the selected molecules showed strong P<sup>-</sup> emissions, as compared with their excitonic emissions.

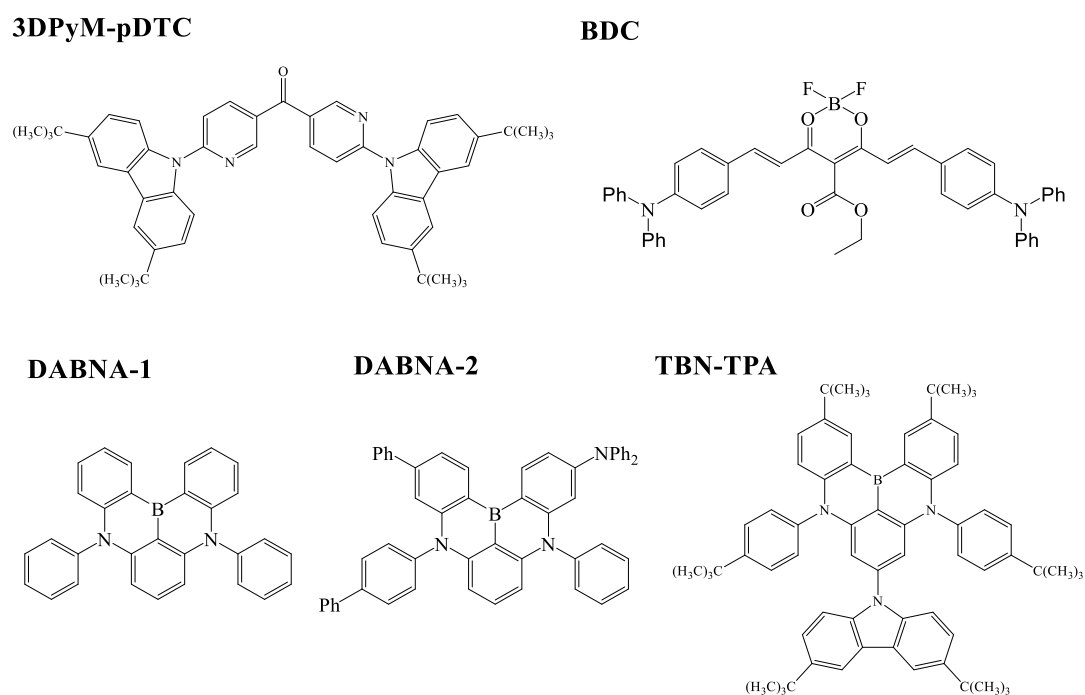


**Figure 3.8** Initially studied TADF molecules: 3DPyM-pDTC, the boron difluoride curcuminoid derivative (BDC), DABNA-1, DABNA-2 and TBN-TPA

DABNA-2 was initially studied in terms of the RISC dynamics inside and outside the cavities. **Figure 3.9** shows the spectra of the neat film of DABNA-2 about absorption, PF at room temperature, and gated emission at 77 K. At low temperature, the gated emission consists of not only DF, but also phosphorescence. The DF is only a weak residual (the peak position is the same as with PF), while the phosphorescence is the main component at  $\sim 515$  nm. The long-

lived fluorescence results from RISC from  $T_1$  to  $S_1$  by thermally activated process. The different intensity between DF and phosphorescence is due to the low RISC rate at 77 K. Hence, phosphorescence can compete with RISC in low temperature range.

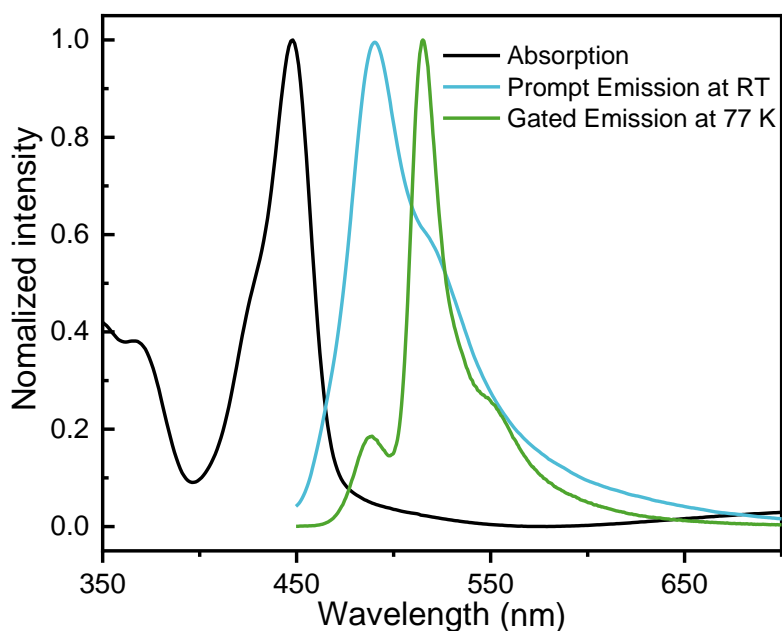


**Figure 3.9** Absorption (black), prompt emission at room temperature (blue) and gated emission at 77 K (green, 50 ns gate delay, delayed fluorescence at  $\sim 490$  nm and phosphorescence at 515 nm) spectra of a neat film of DABNA-2.

Having established the properties of the organic film, we turn our attention to the energy positions of the polariton. **Figure 3.10** presents the angle-resolved reflectivity values for four cavities (**Cavity1.1-1.4**) of different thicknesses. According to the coupled harmonic oscillator analysis (**Equation 2.18**), all the Rabi splitting values are about 0.42 eV, which is higher than the FWHM of the molecular absorption and cavity resonance. Therefore, all the samples are in the strong light-matter coupling regime. However, they have different  $P^-$  energies. Considering the position of the  $T_1$  (it is not perturbed by the vacuum field<sup>[106]</sup>), energy inversion has been achieved in **Cavity1.3&1.4**. In addition, the molecular contributions for the  $P^-$  state are 0.38, 0.33, 0.21 and 0.12 at zero degree for **Cavity1.1-1.4**, respectively. This indicates that the molecular contribution increases and the photonic contribution decreases as the cavities become more red-detuned. The effect of the polariton composition on the transition dynamics will be

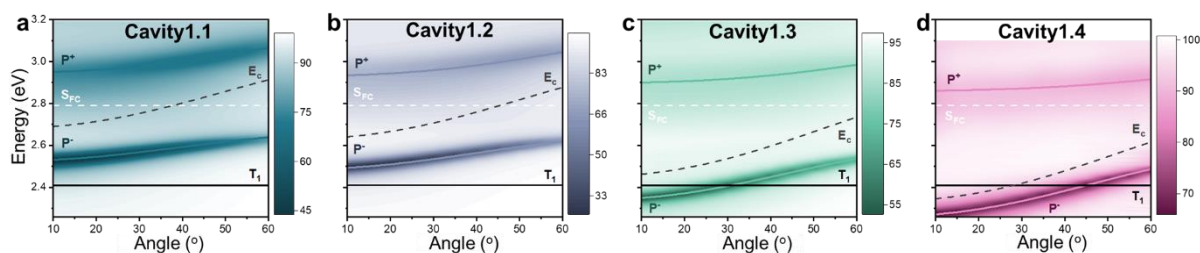


**Figure 3.10** Angle-dependent reflectance of **Cavity1.1 (a)**, **1.2 (b)**, **1.3 (c)**, and **1.4 (d)** together with molecular energy levels ( $S_{FC}$  = Frank-Condon state,  $T_1$  = Triplet state, and  $E_c$  = Cavity energy) and fitted polariton dispersions ( $P^+$  and  $P^-$ ).

described below.

To further verify the energy inversion caused by strong coupling, the emission spectra were evaluated (**Figure 3.11**). Compared with the emission spectrum of the neat film, the P<sup>-</sup> emissions of **Cavity1.1&1.2** are higher in energy compared with the T<sub>1</sub>. In contrast, the P<sup>-</sup> emission in **Cavity1.3&1.4** are lower than the T<sub>1</sub>.

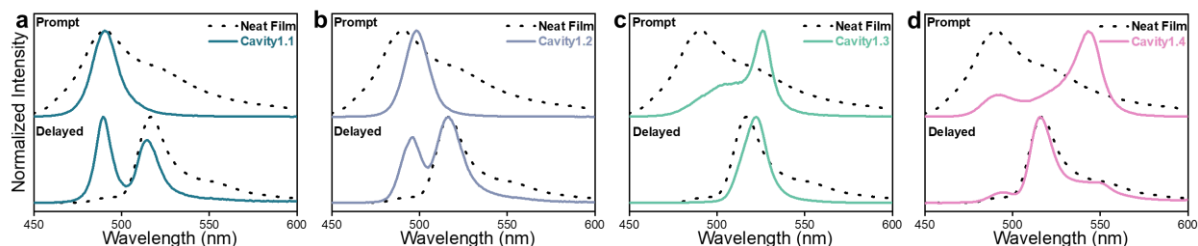


**Figure 3.11** Prompt (recorded at room temperature) and delayed (recorded at 77 K) emission spectra of a neat film (dashed black line), **Cavity1.1 (a)**, **1.2 (b)**, **1.3 (c)**, and **1.4 (d)**.

For all the cavities, the polariton emission maxima move to higher energies upon cooling. The blue shift is of the same magnitude (approximately 2 nm) and is, therefore, attributed to a small contraction of the film during cooling. The emission maximum of phosphorescence from a neat film is indicated by the vertical gray-dashed line in all the graphs, and the energy of the lower polariton, as derived from reflectivity measurements, is indicated with a vertical dashed line of corresponding color.

Up to this point, the singlet-triplet energy inversion has been demonstrated in **Cavity1.3** and **Cavity1.4**. Now, the temperature-dependent DF will be characterized to elucidate the transition dynamics inside the cavities. **Figure 3.12** displays the temperature-dependent long-lived emissions and associated lifetimes inside and outside the cavities. As the temperatures increase, the intensity of the DF in neat film increases initially, but then decreases. Furthermore, the DF lifetimes decrease progressively with increases in temperature. These results are attributed to the different temperature dependencies of  $k_{RISC}$  and  $k_{NR}$ . More concisely, in the lower temperature range, TADF is enhanced due to the increase in  $k_{RISC}$ . As the temperature increases even further, the  $k_{NR}$  plays a more important role. Regarding **Cavity1&2**, similar trends are observed from the same thermally activated processes. However, the energy-inverted **Cavity3** is unique in the series in 3 points: 1) the intensity of the DF decreases steadily as the temperature increases at the beginning; 2) there is a plateau for the temperature-dependent lifetime change (at around 125 K); and 3) the intensity of the P<sup>-</sup> emission is 10-times higher than that for the other samples. Hence, the transition dynamics of coupled and uncoupled molecules differs in the same cavity. As for **Cavity1.4**, its trend of variation is similar to that of the neat film.

To provide more insights into the transition dynamics of these samples, the relative rates of delayed emissions are calculated according to **Equation 3.12**. **Figure 3.13a** represents the relative rates among five samples across the whole temperature range. It is clear that the relative  $k_{RISC}$  in the neat film, as well as in **Cavity1.1**, **1.2** and **1.4**, follows exponential growth, which indicates that the RISC is a thermally activated process. Additionally, the activation energies are 0.115, 0.096, 0.065 and 0.118 eV for the neat film, **Cavity1.1**, **Cavity1.2**, and **Cavity1.4**, respectively. The decreased activation energies in **Cavity1.1** and **Cavity1.2** imply a direct tran-

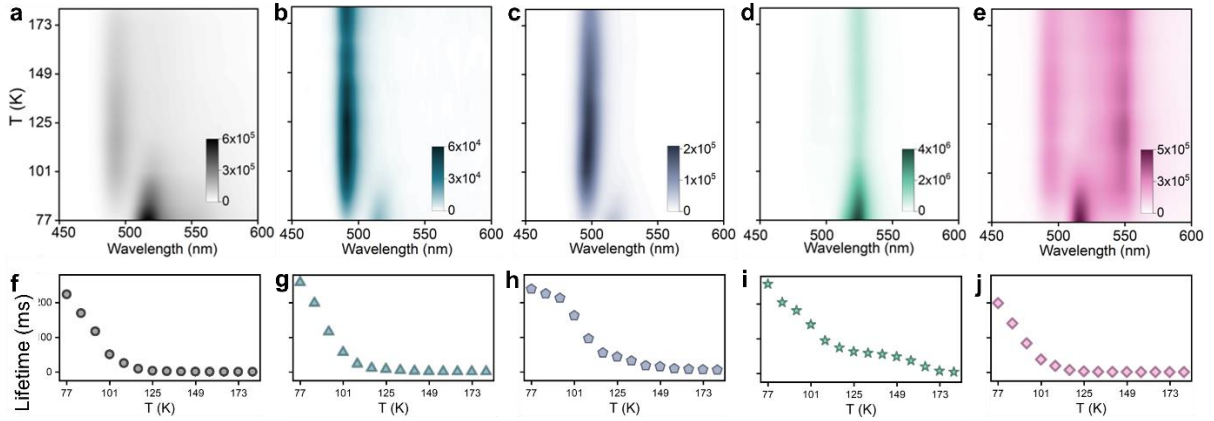


**Figure 3.12** Temperature-dependent gated emissions (gate delay, 100 ns) for neat film (**a**) and **Cavity1.1-1.4** (**b-e**). The emission from **Cavity1.3** is approximately one order of magnitude higher than those from the other cavities. **f-j** Temperature-dependent lifetimes of the delayed emissions.

-sition from the  $T_1$  to  $P^-$ . As for **Cavity1.4**, the effect of energy inversion is negligible for the transition dynamics, which indicates that the connection between the  $T_1$  and  $P^-$  is negligible. This lost connection might be the result of the low molecular contribution in **Cavity1.4**.

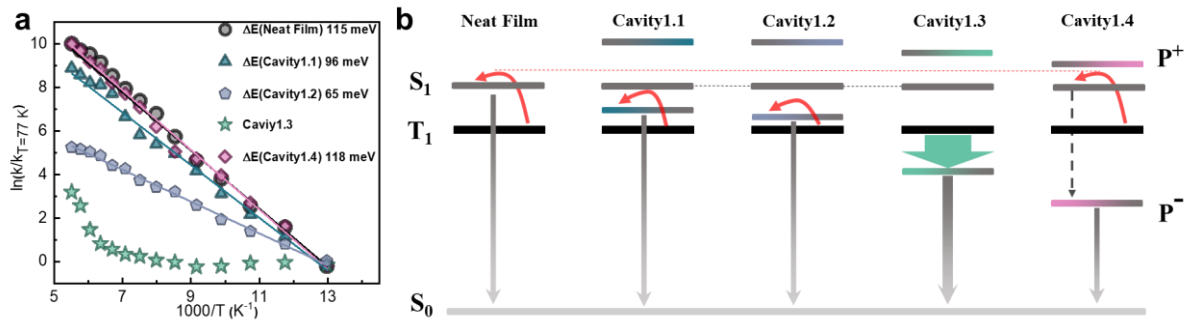


**Figure 3.13** (a) Arrhenius analysis with calculated activation energies for delayed  $P^-$  (or singlet) emissions inside and outside the cavities. Lines indicate the best fit to **Equation 3.12**. (b) Schematic of the dynamics of the triplet to polariton (or singlet) transition at low temperatures. Red arrows represent thermally activated processes and green represents barrier-free RISC. The dashed black arrow indicates a relaxation from  $S_1$  to  $P^-$ , and the gray arrows represent delayed emissions from  $S_1$  or  $P^-$ .

In contrast, in **Cavity1.3**, the relative rate shows little change from 77 K to 150 K, other than exponential growth. Therefore, a barrier-free and exothermic conversion from  $T_1$  to  $P^-$  is realized. Nonetheless, a thermally activated pathway occurs as the temperature increases further. It is assumed that the barrier-free and thermally activated transitions compete with each other. In the low-temperature range, the barrier-free transition dominates the dynamics. The thermally activated transition plays a more-important role when the temperature is higher than 150 K. The transition dynamics among the different samples are shown in **Figure 3.13b**.

After studying the transition dynamics of DABNA-2, we turn our attention to BDC, which is the D-A TADF molecule. A film of BDC (45 wt%, host material is 4,4'-Bis(N-carbazolyl)-1,1'-biphenyl) was placed into the cavities to achieve the strong exciton-photon coupling regime. Due to time constraints, only two cavities have so far been prepared. **Table 3.1** shows the properties of the cavities. **Figure 3.14** shows the basic optical properties of the film and the two

cavities. The  $P^-$  energies of **Cavity2.1** and **Cavity2.2** are lower than the Frank-Condon state (0.332 and 0.402 eV, respectively). Due to the D-A structure, there is a large Stokes shift in the organic film (0.460 eV). Considering the large Stokes shift, the energy differences between the  $P^-$  state of **Cavity2.1&2.2** and the geometry-relaxed  $S_1$  (the energy of  $S_1$  is 1.791, based on the intersection point between the absorption and emission spectra of the organic film) are 0.048 and 0.118 eV, respectively. Meanwhile, BDC has no phosphorescent emission even at 77 K. However, in the literature, it has been reported that the singlet-triplet energy gap is 0.10 eV<sup>[103]</sup>.

**Table 3.1** Properties of BDC inside **Cavity2.1&2.2**. (The unit of the energy is eV).

Sample	Cavity2.1	Cavity2.2
Rabi splitting	0.700	0.711
Detuning	-0.040	96.7
$P^-$ energy position	1.743	1.673
Energy difference ( $P^-$ vs $S_{FC}$ )	0.332	0.402
Energy difference ( $P^-$ vs $S_1$ )	0.048	0.118

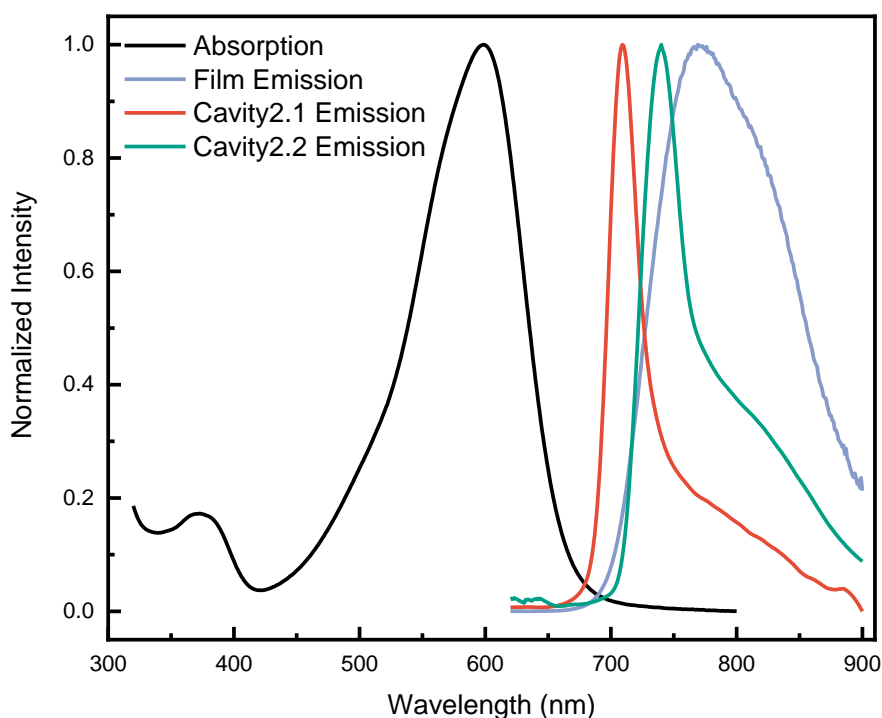


**Figure 3.14** Basic optical properties of the film and the two cavities.

We now turn our attention to the DF transition dynamics. **Figure 3.15a&b** present the temperature-dependent DF emissions for the bare film and **Cavity2.1**. In addition, the temperature-dependent DF lifetimes were measured. In similarity to the case of DABNA-2, the  $k_{RISC}$  is calculated for the two samples (**Figure 3.16c**). Even though the energy difference between the  $P^-$  and singlet state is much larger than the Frank-Condon state, the result indicates that no transition dynamics change occurs after placing the BDC molecules into the cavity. This may be the result from large Stokes shift (0.465 eV) for the BDC. The dynamics of **Cavity2.2**

was also studied. However, the DF intensity was too weak to measure. One explanation is that based on the energy gap law mentioned in **Section 3.2**, the non-radiative rate increases exponentially as the red-shift of the emission occurs. In addition, it has been reported in the literature that the quantum yield decreases dramatically as the peak position goes to a lower energy<sup>[103]</sup>. Therefore, the weak signals result from the low quantum yield of **Cavity2.2**. Accordingly, the inverted singlet-triplet state is not achieved in BDC due to the large Stokes shift. Another interpretation for the low intensity of the signal is that. The lower energy of P<sup>-</sup> will affect the ISC process in this molecule. Then the yield of ISC in the cavity is too small to contribute to the later RISC process.

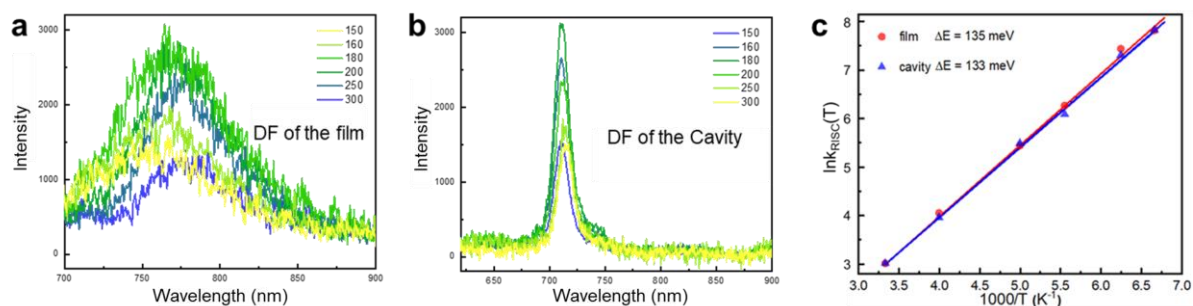


**Figure 3.15** Temperature-dependent DF of the BDC film (a) and **Cavity2.1** (b), (c) temperature-dependencies  $k_{\text{RISC}}$  for the film (red) and **Cavity2.1** (blue).

In conclusion, we demonstrate inversion of the singlet and triplet excited states of a TADF molecule following strong coupling to an optical cavity. The limitation of Hund's rule has been broken by manipulating the energy flow from the triplet to the P<sup>-</sup> state through a barrier-free transition. The results obtained in this work could promote new applications of OLEDs.

### 3.3 Manipulation of molecular trap states by strong light-matter coupling

When the temperature is  $<200$  K, the long-lived emissions from DABNA-2 films result from the TADF process due to the RISC, which has the same spectral envelope as the prompt emission. However, at room temperature, the long-lived emission of the same sample is red-shifted and shows clear signatures indicative of excimer formation (shown in **Figure 3.16**). The peak positions of the absorption and PF are 448 and 490nm, respectively. In addition, both spectra have small FWHMs. In contrast to the situation at low temperatures the long-lived emission at room temperature shows a much broader and red-shift excimer feature, with the peak maximum at around 600 nm. The reason why the DF is completely different from the PF is that the DF is from the triplet channel, which is significantly long-lived, enabling the trapping of the excited state into an excimer state. In this way, RISC takes place from the excimer triplet manifold to the excimer singlet manifold. Moreover, the different performance of DF at room temperature versus low temperature is most likely due to the fact that excimer formation is a diffusion-controlled process<sup>[107]</sup>.

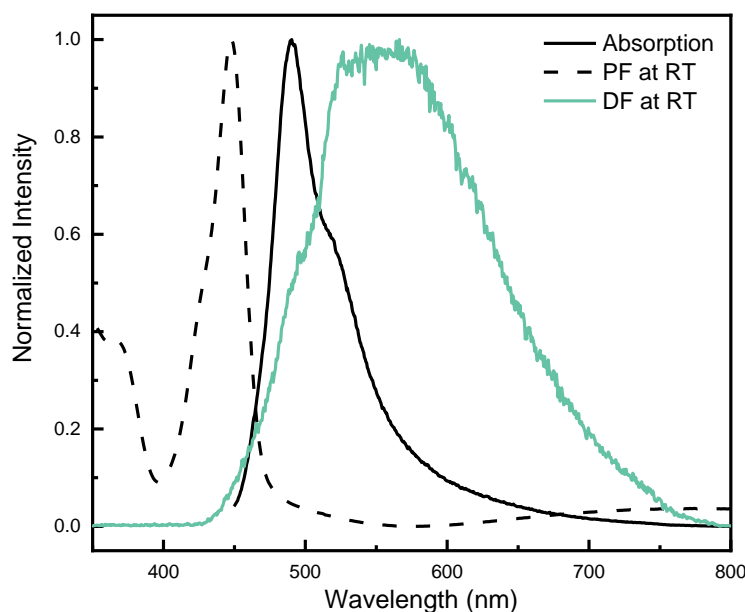


**Figure 3.16** Absorption (dashed line), PF (black solid line) and DF (green solid line) of a DABNA-2 film at room temperature.

The optical properties of neat DABNA-2 films inside cavities were studied. Two cavities with different detuning patterns are shown in **Figure 3.17**. Specifically, one cavity is red-detuned, while the other one is blue-detuned. From the analysis of a two-harmonic oscillator model (**Equation 2.18**), their Rabi splitting levels are both are about 0.41 eV, which is higher than the FWHM of the molecular transition (0.19 eV). In addition, both of these cavities show anti-crossing behaviors, as evidenced by angle-resolved reflectivity measurements. Accordingly, the two samples are in the strong coupling regime.

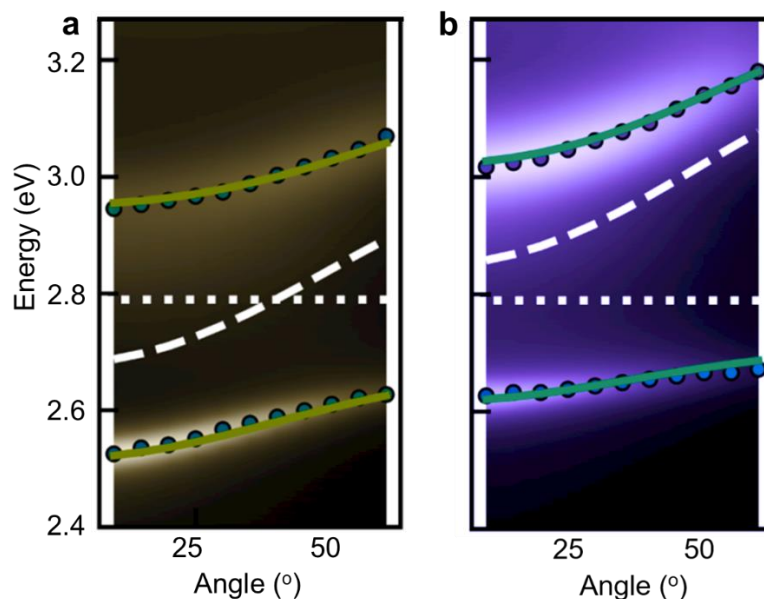


**Figure 3.17** Angle dependent reflectivity of DABNA-2 inside **Cavity3.1 (a)** and **Cavity3.2 (b)**

**Figure 3.18** DF spectra of the strongly coupled system at room temperature. The emissions inside the cavities are detuning-dependent. Compared with the neat film outside the cavity, the red-detuned cavity shows almost exclusively delayed polaritonic emission. Whereas the blue-detuned cavity shows a higher degree of excimer emission with a little hump representing the long-lived polaritonic emission. Given no excimer feature for the PF in the films inside and outside the cavities, the excimer states should be formed on the triplet surface. Considering that the red-detuned cavity has a lower energy than the blue-detuned one, it is hypothesized that the small difference in the  $P^*$  energy position can significantly change the energetic driving force for the transition from the triplet excimer to the polariton.

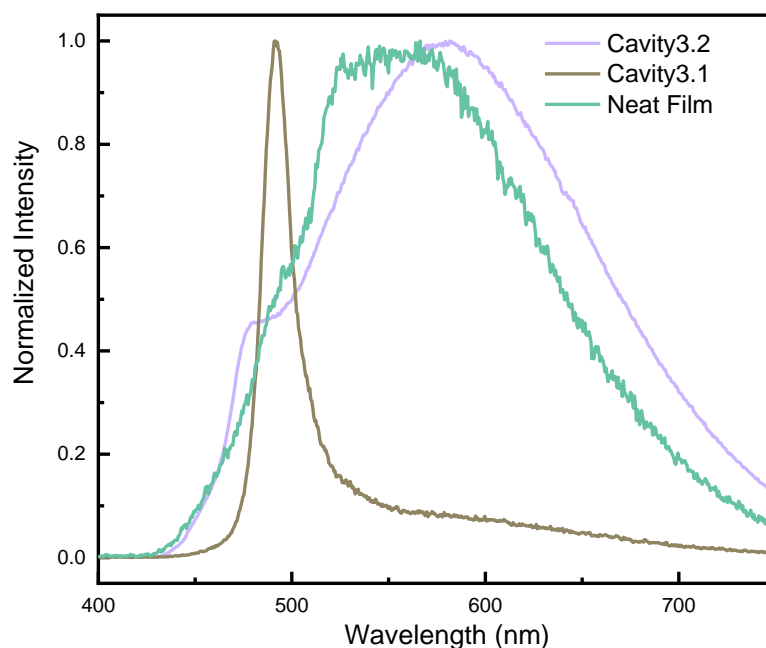


**Figure 3.18** The DF of the Neat Film, **Cavity3.1** and **Cavity3.2**.

The transitions between the excimer and P<sup>-</sup> states of the two cavities are shown in the Jablonski diagram in **Figure 3.19**.

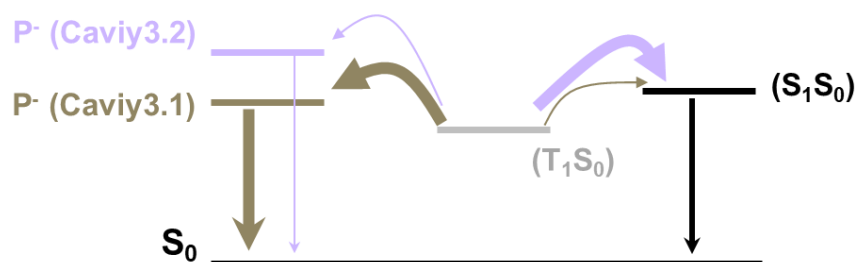


**Figure 3.19** Jablonski diagram showing the transition from the excimer to the P<sup>-</sup> state.

To strengthen our hypothesis, time-resolved delayed emission spectra were measured for the two differently detuned cavities. The red-detuned cavity shows no decrease of the ratio of the P<sup>-</sup> and excimer emission intensities as the gate time ranges from 50 ns to 1  $\mu$ s, whereas the ratio of the blue-detuned one decreases as time progresses. This supports the previous discussion that the trap states form on the long-lived triplet surface. Moreover, the non-decreasing feature means that the transition occurs directly from the triplet excimer state to the P<sup>-</sup> state (**Figure 3.20a**). In contrast, in the blue-detuning cavity, some part of the delayed polaritonic emission result from the monomer RISC process (**Figure 3.20b**), which has a shorter lifetime compared with the excimer.

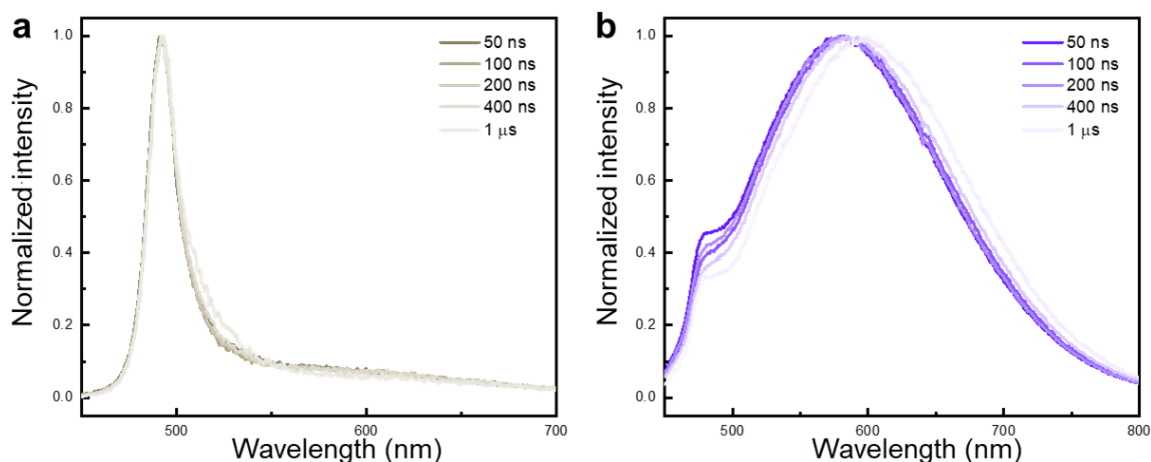


**Figure 3.20** Normalized time resolved delayed emission spectra for the **Cavity3.1(a)** and **Cavity3.2 (b)**.

We have concluded that the position of the P<sup>-</sup> energy level plays a key role in the manipulation of excimer emission by strong light-matter coupling. However, there are multiple states and transitions involved in the DABNA-2 system, which makes it very difficult to study the dynamics quantitatively. We now turn our attention to an easier case in which the long-lived triplet state is not taken into account. The molecule we selected was 1-ethyl-perylene (et-perylene), which is a flat dye with a high transition dipole moment. As shown in **Figure 3.21**, it has a broad excimer emission with a lifetime in the nanosecond range.

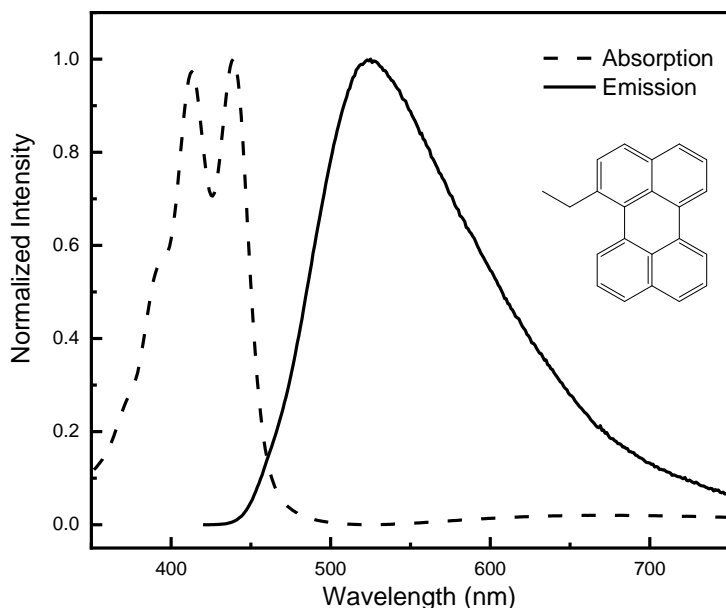


**Figure 3.21** Absorption (dashed line) and fluorescence (solid line, dominated by excimer emission) profiles of 1-ethyl-perylene at room temperature.

Similar to the case of the DABNA-2, the et-perylene inside the cavities with different detunings were investigated. Their detuning information is shown in **Figure 3.22** where four samples are presented. The molecular contribution to the  $P^+$  state ranges from 36% for the most red-detuned cavity to 78% for the most blue-detuned cavity. Through the analysis of a coupled harmonic oscillator model using a  $3 \times 3$  matrix, the Rabi splitting levels are found to be within a similar range for all the cavities, at about 0.34 eV and 0.38 eV for the first and second transitions, respectively. Both of these values are higher than the FWHMs of the molecular transitions (0.14 eV and 0.20 eV, respectively). These results indicate that all of the samples are in the strong coupling regime.

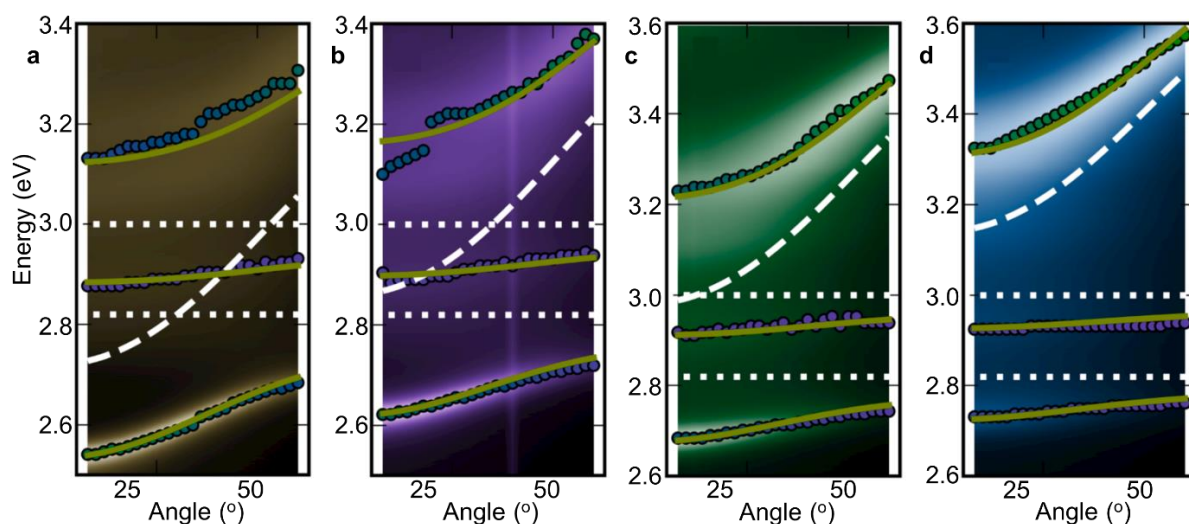


**Figure 3.22** Angle-dependent reflectivity of the 1-ethyl-perylene inside **Cavity 4.1-4.4 (a-d)**.

As for the emission spectra of the strongly coupled et-perylene (**Figure 3.23a**), the results show an obvious detuning dependency, which is consistent with the case of DABNA-2. The highest

polaritonic emission is obtained for the most red-detuned cavity, while the most blue-detuned cavity shows the strongest excimer emission, which is most-pronounced in the 550–600 nm region. The same dependency as the last case of DABNA-2 strengthens our hypothesis that the position of the  $P^-$  state is crucial for the transition dynamics with excimer emission. The lower  $P^-$  state will suppress excimer emission.

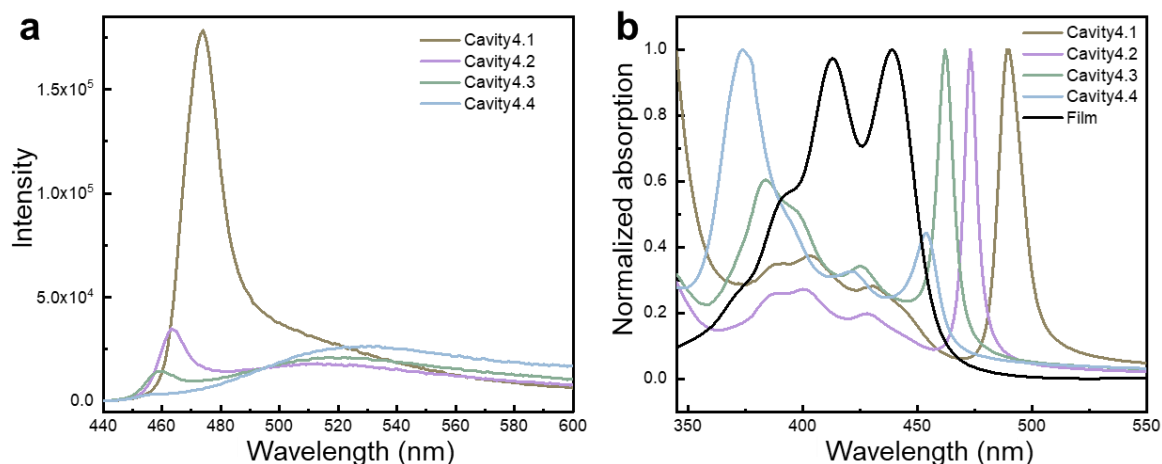


**Figure 3.23** (a) Emission spectra of the four differently tuned cavities containing et-perylene; (b) comparison of the molecular absorption and excitation spectra of the four cavities (0 degree).

To further study how the excimer states are populated, excitation spectra for the emissions at 520 nm are shown in **Figure 3.23b**. The most red-detuned cavity shows the largest mismatch between the cavity excitation and the molecular absorption spectra. In fact, the competing process occur between the emissions of polariton and excimer, which result from the exciton reservoir. For the most red-detuned cavity, the larger energy gap between the exciton reservoir and the  $P^-$  state leads to the strongest driving force of the polariton emission. In contrast, the blue-detuned cavity has a weaker driving force. Meanwhile, the decays from the exciton reservoir to the excimer state are the same for all the different detuned samples. Therefore, it is energetically more-favorable to populate the polariton emission in a red-detuned cavity than in a blue-detuned cavity.

In conclusion, it has been presented that the excimer emission can be manipulated by the strong light-matter interaction. This can be accomplished with both short- and long-lived emissions. In practice, this strategy has potential to increase the purity levels of light-emitting devices.

### 3.4 Energy gap law considering the effect of excitonic coupling

As mentioned in **Section 2.2.3**, the rate of non-radiative decay ( $k_{nr}$ ) follows the energy gap law. In this section, I will provide a quantitative explanation for this, considering the excitonic coupling that occurs in J-aggregates.

The reorganization energy is of importance when discussing the energy gap law. It is the amount of energy required to stabilize the highly polar solute transient-solvent system in the molecular excited state<sup>[78]</sup>, which leads to a relaxed state of free energy. In general, the reorganization energy is represented by half of the Stokes shift, and can be expressed as,

$$\lambda = \frac{1}{2} \hbar [\max(\sigma_a(\nu)) - \max(\sigma_f(\nu))] \quad (3.13)$$

where  $\max(\sigma_a(\nu))$  and  $\max(\sigma_f(\nu))$  are the peak positions of the normalized absorption and emission. However, this equation is valid only when the absorption and emission spectra of the molecules are Gaussian in shape<sup>[108]</sup>. In other situations, the simple **Equation 3.13** cannot be used. The alternative method is to consider the relationship between two integrals shown below<sup>[109]</sup>,

$$\lambda = \frac{\int_0^\infty [\sigma_a(\nu) - \sigma_f(\nu)] \nu d\nu}{\int_0^\infty [\sigma_a(\nu) + \sigma_f(\nu)] d\nu} \quad (3.14)$$

where  $\sigma_a(\nu)$  and  $\sigma_f(\nu)$  are the absorption and emission spectral line shapes, respectively, and the two integrals are used to show information about the absorption and emission intensities.

In **Section 2.4.1**, the limits of strong and weak excitonic coupling have been introduced. As derived by Englman and Jortner, in the weak coupling regime, the ground and excited states are in a matching type of configuration in which no surface crossing occurs. Consequently, the  $k_{nr}$  can be represented by the equation below<sup>[61]</sup>,

$$k_{nr} = \frac{C^2 \sqrt{2\pi}}{\hbar \sqrt{\omega_{vib} \Delta E}} \exp \left\{ -\frac{\Delta E}{\omega_{vib}} \left[ \ln \left( \frac{\Delta E}{l \cdot \lambda} \right) - 1 \right] \right\} \quad (3.15)$$

where  $C$  represents the effective electronic coupling constant between the ground and excited states,  $\Delta E$  is the energy difference between  $S_1$  and  $S_0$ ,  $\omega_{vib}$  represents the vibrational energy,  $l$  is the number of vibrational modes that induces the non-radiative transition, and  $\lambda$  is the reorganization energy of the promoting vibrational mode. Here, the equation describes the energy gap law quantitatively, whereby  $k_{nr}$  increases exponentially as the energy gap decreases. In the strong excitonic coupling regime (a J-aggregate), the molecules are coherently delocalized. In this case, the excited state spreads out over many molecules, and each individual molecule becomes more ground state-like. Then, it is specified as **Equation 3.16**<sup>[110]</sup>:

$$\lambda_J = \frac{\lambda_M}{N} \quad (3.16)$$

where  $\lambda_M$  and  $\lambda_J$  represent the reorganization energies of the monomer and J-aggregates, respectively, and  $N$  is the exciton delocalization length. The equation indicates that strong

exciton coupling connects the molecular states and amplify the excitation configuration<sup>[111]</sup>. Thereafter, the monomer's reorganization energy is partitioned into multiple excitonic wave vector modes. Finally, the reorganization energy is decreased in the J-aggregates. One simple case is when the reorganization energy of the dimers is lower than that of the monomer<sup>[112]</sup>. Then, a semi-quantitative analysis can be used to study the emission quantum yield change from the monomer to the J-aggregates. When only considering the delocalization effect on the non-radiative process, the  $k_{nr}$  of the J-aggregates can be shown as in the equation below,

$$k_{nr} = \frac{C^2\sqrt{2\pi}}{\hbar\sqrt{\omega_{vib}\Delta E}} \exp\left\{-\frac{\Delta E}{\omega_{vib}} \left[ \ln\left(\frac{\Delta E}{l \cdot \lambda_J}\right) - 1 \right]\right\} \quad (3.17)$$

The effect of exciton delocalization can counterbalance the reduced energy gap. This indicates that the  $k_{nr}$  might be maintained or even decreased in the J-aggregates compared with the monomer, due to the excitonic delocalization effect. Therefore, excitonic delocalization has the potential to counteract the energy gap law and facilitate high-quantum yields of NIR dyes.

### 3.5 Overcoming the energy gap law by strong excitonic coupling

This section discusses the results from **Paper III**. The background of J-aggregates and the energy gap law were introduced in **Sections 2.4 and 3.4**, respectively. Previously, the limited solubility has been the main obstacle for studying rylene-expanded dyes <sup>[113, 114]</sup>. Here, bay-alkylation was used to increase the solubility of quaterrylene. The procedure for synthesizing quaterrylene is not discussed here but can be found in **Paper III**. The molecule studied is a bay-alkylated quaterrylene, named 1,1'-dihexylquaterrylene (QTRLN), the structure of which is shown in **Figure 3.24**. The excitonic coupling properties of QTRLN will be examined in detail in the section.

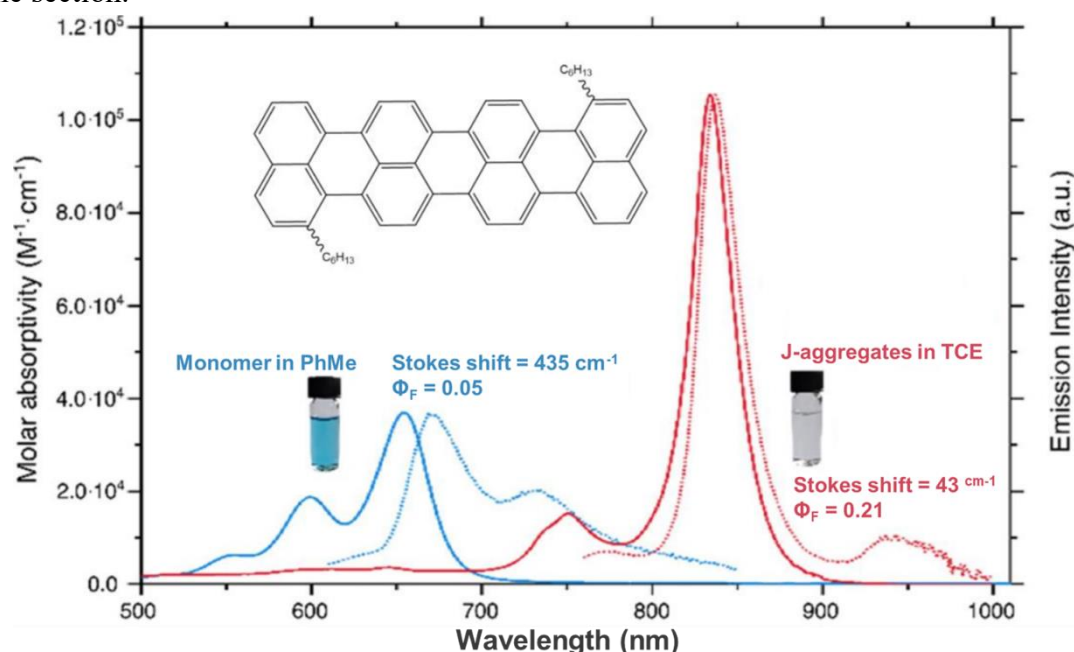


**Figure 3.24** Absorption and emission spectra of  $10^{-6}$  M QTRLN recorded in toluene (blue) and in  $C_2H_2Cl_4$  (red), scaled according to their molar absorptivity values. QTRLN is present in its monomeric form in toluene, while in  $C_2H_2Cl_4$  it forms super-radiant J-aggregates.

The purified QTRLN was first dissolved in different solvents. It was noticed that the colors of solutions were different. That is, the compound was light blue in toluene and dichloromethane (DCM), while it was completely transparent and colorless in 1,1,2,2-tetrachloroethane (TCE). We then measured the spectroscopic properties of the samples dissolved in DCM and TCE. As shown in **Figure 3.24**, rylene-characteristic vibrational bands are presented in the absorption spectrum of QTRLN. The peak positions of the vibronic processes for  $A_{0-0}$ ,  $A_{0-1}$ , and  $A_{0-2}$  are 654, 600 and 552 nm, respectively. Furthermore, the molar absorptivity coefficient at 654 nm is  $37,000 \text{ M}^{-1}\text{cm}^{-1}$ . Nonetheless, when QTRLN was dissolved in TCE, its absorption showed a significant red-shift (of almost 180 nm or  $3,300 \text{ cm}^{-1}$ ), as well as a greatly narrowed band. Moreover, the number of vibronic bands decreased to two, and the ratio of the intensities of the two bands ( $A_{0-0}$  and  $A_{1-0}$ ) dramatically increased. Finally, the molar absorptivity coefficient ( $105,000 \text{ cm}^{-1}$ ) of QTRLN in TCE was 3-fold higher than that of QTRLN in toluene.

Regarding the emission spectra, the emission profile of the dye in toluene was almost the mirror image of the absorption profile, with the  $I_{0-0}$  and  $I_{0-1}$  peaks at 671 nm and 733 nm, respectively. In addition, the Stokes shift between the absorption and emission was  $365 \text{ cm}^{-1}$ . As for the dye

in TCE, its emission is also a mirror image of the absorption and the emission was in the NIR regime. However, the Stokes shift was now greatly decreased to 3 nm ( $43 \text{ cm}^{-1}$ ). Taken together, these results suggest that QTRLN forms J-aggregates when dissolved in TCE, and are in a monomeric form when dissolved in toluene.

Now we turn our attention to a quantitative assessment of the J-aggregates. In order to determine whether the J-aggregates are in the strong excitonic coupling regime, the values of the exciton bandwidth ( $W$ ) and nuclear relaxation energy ( $S\omega_{vib}$ ) were compared. According to the theory described in **Section 2.4**, the resonant Coulombic coupling ( $J_c$ ) was calculated based on the  $A_{0-0}$  energy difference between the monomer and the J-aggregates. Thus, according to **Equation 2.33**, the value of  $W$  was  $6,688 \text{ cm}^{-1}$ . Meanwhile,  $S\omega_{vib}$  was  $700 \text{ cm}^{-1}$ , considering the vibrational energy ( $\omega_{vib} = 1,400 \text{ cm}^{-1}$ ) and Huang-Rhys factor ( $S = 0.5$ ) (obtained by the method described in **Section 2.4.2**). Therefore,  $W$  was 9.5-times higher than the  $S\omega_{vib}$ , which indicated that the J-aggregates are in the strong excitonic coupling regime. Therefore, the lower-energy transitions in aggregates resulted from the delocalization of the multiple QTRLNs, which eventually led to the significant red-shifting of the emission and absorption.

Besides the changes in the transition energies, the emission quantum yields were 0.05 for the monomer and 0.21 for the J-aggregates. The quantum yield of the monomer was very close to those of other molecules having similar structures<sup>[115, 116]</sup>. It was clear that the molecule lacks rotatable aromatic structures, and that the quantum yield was achieved at a very low concentration. As a consequence, the increased quantum yield for the J-aggregates should not be the result from aggregation-induced effects. Considering the large red-shifting and NIR emission of the J-aggregate, the quantum yield was actually very high. For example, some highly-emissive NIR dyes, such as cyanine and dibodipy derivatives, showed quantum yields of  $< 0.05$ .

To study in greater depth the mechanism underlying the high quantum yield of the J-aggregates, time-resolved emission spectroscopy was measured. The lifetime of the monomer was 1.05 ns, as measured with time-correlated single-photon counting. For the emission lifetime of the J-aggregates, a streak camera was used to assess intensity dependency with time (no change with time could be observed). Instead, the decay followed a mono-exponential function and the lifetime was 1.50 ns. The photophysical properties of the QTRLN states are summarized in **Table 3.2**.

**Table 3.2** Photophysical properties of QTRLN in monomer and J-aggregates states.

Property	Monomer	J-aggregates
Abs <sub>max</sub> (nm)	654	834
$\epsilon$ ( $M^{-1} \text{ cm}^{-1}$ )	37,000	105,000
Em <sub>max</sub> (nm)	1.743	1.673
Stokes shift ( $\text{cm}^{-1}$ )	0.332	0.402
Lifetime (ns)	1.05	1.50
Quantum yield	0.05	0.21
$k_r$	$4.8 \cdot 10^7$	$1.4 \cdot 10^8$
$k_{nr}$	$9.05 \cdot 10^8$	$5.33 \cdot 10^8$

According to these results, compared with the monomer, the radiative rate of J-aggregates is 3-fold higher, while the non-radiative rate is 40% lower. As for the change in the radiative rate, the increase is due to superradiance, as described in **Section 2.4** as reported previously<sup>[82]</sup>. Regarding the non-radiative rate, to the best of our knowledge, no case showing a decrease has been reported to date for J-aggregates. Considering the substantial red-shift, the result overcomes the energy gap law mentioned in **Section 3.2**. To understand the reason for the slower-than-expected non-radiative decay, the effect of excitonic delocalization should be taken into account. Thus, the issue is how to calculate the excitonic delocalization length ( $N$ ) of the J-aggregates (described in **Section 2.4**). This value calculation can follow three strategies: based on the difference of the line width, superradiance effect and reorganization energy in the monomer and J-aggregates.

For the first strategy, according to **Equation 2.35**, by comparing the  $FW_{2/3}Ms$  of the absorption spectra,  $N$  is 6, which indicates that in TCE solution, 6 chromophores are coherently delocalized. In the second method, for ideal J-aggregates with the molecules in a perfectly head-to-tail structure, the delocalization length can be calculated based on the ratio of the two radiative rates (monomer and J-aggregate), giving a result of 3, which is lower than the value obtained by the analysis of the spectral  $FW_{2/3}Ms$ . The difference can be interpreted as showing that the molecules in the aggregate are in a slip-stacked arrangement rather than in an ideal head-to-tail structure.

Regarding the third strategy, a major difference between the monomer and aggregates is the decreased reorganization energy ( $\lambda_M$ , is  $589\text{ cm}^{-1}$  and  $\lambda_J$  is  $131\text{ cm}^{-1}$ ). Thus is because of the excitonic delocalization, whereby each molecule in the aggregates contains only a partially excited state electron density, leading to a geometry that resembles more closely the ground state than the excited state. According to the ratio of the two  $\lambda$  values (shown in **Equation 3.14**), the delocalization length is 4.5.

Evaluation of the aggregate size is performed with diffusion NMR spectroscopy (DOSY). During the diffusion experiment, the smaller species diffuse faster than the larger species. Thus, the latter ones maintain in the NMR spectra for longer times. A predictive model is constructed to simulate the diffusion coefficients for the aggregates. This model consists of slip-stacked molecules placed  $3.5\text{ \AA}$  apart, which is the conventional stacking distance for perylenes. The model was utilized to simulate the diffusion coefficient using the HYDRO++10 software. The experimental and simulated coefficients are summarized in **Table 3.3**. For the QTRLN monomers in  $CD_2Cl_2$ , the experimental and simulated results are consistent with each other, which confirms the accuracy of the simulated model. As for the QTRLN aggregates in  $C_2D_2Cl_4$ , the experimental values overlap with the simulated values at 14 units. This indicates that the size of the slip-stacked aggregates is 14. It should be noted that the DOSY measurement requires a relatively high sample concentration ( $10^{-4}\text{ M}$ ). In contrast, for the optical spectroscopy measurements, the concentration should be low (here,  $10^{-5}\text{ M}$ ). Therefore, the higher value of  $N$  obtained from DOSY arises from the concentration difference. However, the DOSY results

**Table 3.3.** Experimental and simulated diffusion coefficients of QTRLN (units are  $m^2/s$ ).

Solvent	Experimental	Simulated
$CD_2Cl_2$ ( $10^{-4}\text{ M}$ )	$1.0*10^{-9} (\pm 7*10^{-11})$	$1.0*10^{-9}/14\text{ units}$
$C_2D_2Cl_4$ ( $10^{-4}\text{ M}$ )	$6.0*10^{-11} (\pm 6*10^{-12})$	$6.4*10^{-11}$

still show that the QTRLN in TCE has a multiple slip-stacked structures.

After obtaining the value of  $N$ , we proceeded to study the non-radiative rates for the monomer and J-aggregates. Regarding the QTRLN monomer in toluene, half of the Stokes shift is smaller than the energy of the vibronic mode (182 and 1,400  $\text{cm}^{-1}$ , respectively). The non-radiative rate of the monomer can be described quantitatively following **Equation 3.15** based on the energy gap law. For the J-aggregates in TCE, due to the strong excitonic coupling effect, the calculation should follow **Equation 3.17**. However, the value of the electronic coupling ( $C$ ) is unknown for either the monomer or J-aggregates, which prevents a fully quantitative calculation of the two non-radiative values. However, a semi-quantitative analysis can still be carried out by dividing the non-radiative rates of the monomer and J-aggregates with each other. Here, it is assumed that the  $C$  is the same for both the monomer and J-aggregates. According to the two equations, considering the excitonic delocalization (using the experimental reorganization energies for the monomer and J-aggregates), the ratio of  $k_{nr}$  in the monomer and J-aggregates is 1,600. In contrast, when only considering the energy gap difference, the ratio is 0.0025. The real value is 1.7, indicating that additional factors, which are difficult to obtain experimentally (such as  $C$ ), need to be considered in the more-quantitative analysis. Nonetheless, the results indicate that the exciton delocalization in the J-aggregates counterbalances the reduced energy gap, thereby substantially increasing the emission quantum yields of the NIR dyes.

In conclusion, it is assumed that the highly ordered nature of the J-aggregates structure reduces the reorganization energy through excitonic delocalization, thereby overcoming the energy gap law to facilitate the development of organic NIR dyes.

## 4. Methodology

This chapter outlines the experimental methods and techniques used in the work of this thesis. The sample preparation methods are described in Sections 4.1. Thereafter, the different spectroscopic methods are presented in the later sections.

### 4.1 Organic film preparation

The organic films of the molecules are prepared by spin-coating. Before spin-coating, the molecule is dissolved in a suitable solvent. The process of spin-coating is shown in **Figure 4.1**. Initially, this solution is dropped onto a substrate in the spin-coater. Then the rotation is started and accelerated to the desired speed. Most of the liquid is expelled due to centrifugal force. Finally, the viscous film becomes thinner and the remainder of the solvent is excluded by an air flow, yielding a solid film of the molecule.

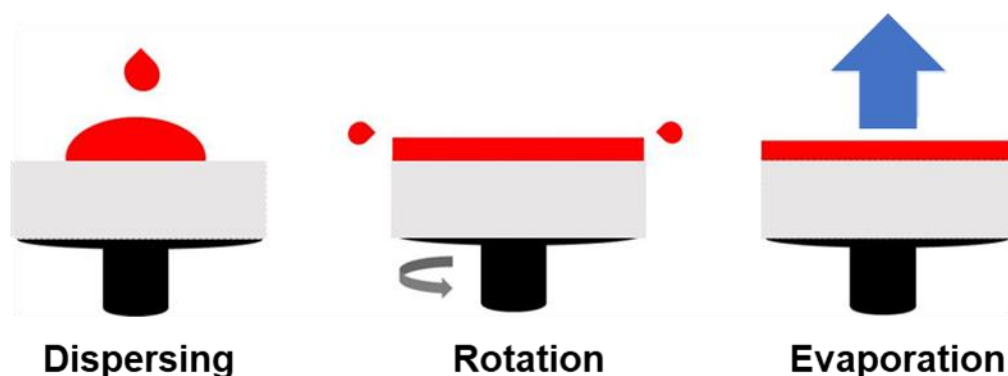


**Figure 4.1** Three processes of spin-coating, including: dispersing, rotation and evaporation.

The spin-coating technique was used in **Paper I-II**, to prepare the optical active layer inside the optical cavity. The dye molecule and polymers were dissolved at a desired mass ratio in a suitable solvent. The overall concentration of both molecules was used to calculate the appropriate thickness to couple to one of the cavity modes; normally, the lambda mode was used. The fine-tuning was performed by changing the rotational speed during the spin-coating process, making it possible to produce cavities with different types of detuning of the strong exciton-photon coupling.

A flat and well-proportioned organic film is essential for the creation of high-quality cavities (with high-Q factor). Extensive efforts were put into developing skills for growing the desired

films using spin-coating. The following four main strategies were used: 1) the thickness of film was directly proportional to the concentration of the solvents and the inverse of the square root of the spin speed, which are the two general variables for controlling the thickness; 2) even though a thick film could be achieved at low spin speed, the flatness was affected, especially when the spinning was performed at  $<1,000$  rpm. In order to obtain satisfactory samples, the concentration of the solvents had to be sufficiently high. Thus, a higher spin speed could be used; 3) in general, dynamic dispense spin coating performs better than static dispense spin coating; and 4) millipore filter can facilitate the exclusion of invisible sediments from the spin-coating solvents, which further increases the flatness and Q-factor for the cavities.

## 4.2 The growth of silver layers

The growth of silver layers was carried out using magnetron sputtering. Magnetron sputtering is a widely used physical vapor deposition (PVD) method for the deposition of metallic thin films<sup>[117, 118]</sup>. It is a high-vacuum ionic sputtering method, in which high energy ions bombard a target and eject atoms from its surface (**Figure 4.2a**).

A high voltage (around 500 V) is applied to create a plasma between the cathode and the anode. The magnets keep the electrons close to the surface of the target, generating a higher plasmonic density and increased growth speed. During the sputtering process, the vacuum chamber is first evacuated to remove all contaminating gases and to reduce the partial pressures of all the background gases. Argon gas is then injected and becomes positively charged in the plasma (activated plasma shown in **Figure 4.2b**), and it is accelerated towards the cathode located below the target. The kinetic energy is sufficiently high to eject atoms from the metallic target. The loose atoms migrate through the high-vacuum chamber and are deposited on the glass or quartz substrate. The thickness of the metal film is manipulated by a quartz crystal microbalance (QCM), which is located close to the substrate holder. The frequency of the QCM is affected by the deposition on the surface of the crystal. The thickness can be manipulated on a sub-nanometer scale.

The sputtering technique was used in **Paper I-II**, to prepare bottom and upper silver layers for the optical cavity. For the bottom layer, the thickness is 100 nm, and it acts as a reflective side. Regarding the upper layer, the thickness is 30–40 nm, and it acts as a semi-transparent side.

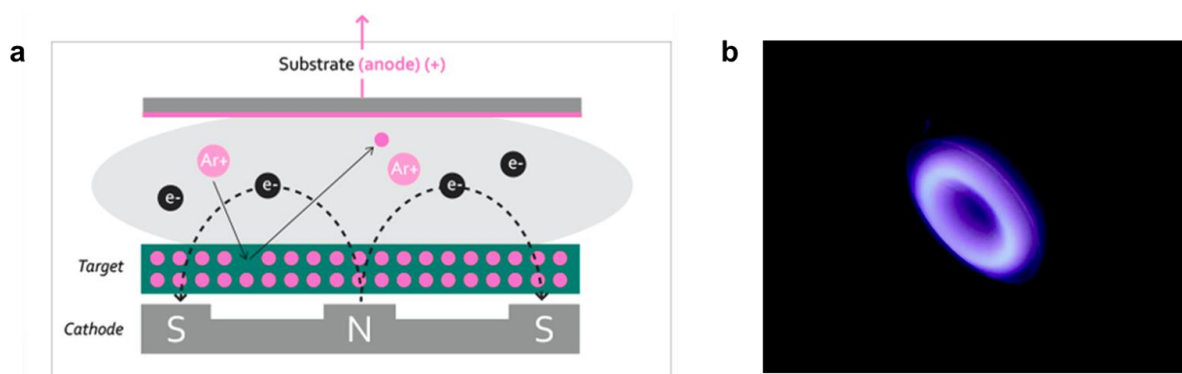


**Figure 4.2** (a) The mechanism of the magnetron sputtering sputter, (b) The Photograph of a activated plasma.

### 4.3 Ultraviolet-visible spectroscopy

Ultraviolet-visible spectroscopy (UV-Vis) is used to measure the molecular electronic and vibronic transitions. It gives insights into the molecule's singlet energy levels and transition dipole moment. The absorption depends on the molecular molar absorptivity coefficient  $\epsilon$ . The value of  $\epsilon$  is specific for a structure and is energy (wavelength or wave number)-dependent. The absorption at a certain wavelength  $A_\lambda$  is described by the Beer-Lambert-Bouguer law<sup>[119]</sup>,

$$A_\lambda = \epsilon(\lambda)cl \quad (4.1)$$

where  $c$  is the sample concentration, and  $l$  is the path length for the sample.

A typical setup is shown for the double-beam UV-Vis spectrophotometer (**Figure 4.3**). In the settings, the light of a lamp with a broad spectrum is made monochromatic. It is then split into two separate beams. One beam hits the sample and the other passes through the reference. Finally, both light beams are received and the absorption  $A_\lambda$  is determined by the following equation,

$$A_\lambda = \log \frac{I_0(\lambda)}{I(\lambda)} \quad (4.2)$$

where  $I(\lambda)$  is the intensity of the transmitted light through the sample, and  $I_0(\lambda)$  is the intensity of the transmitted light of the reference beam. The reference sample is the substrate used for solid samples or the solvent in a cuvette.

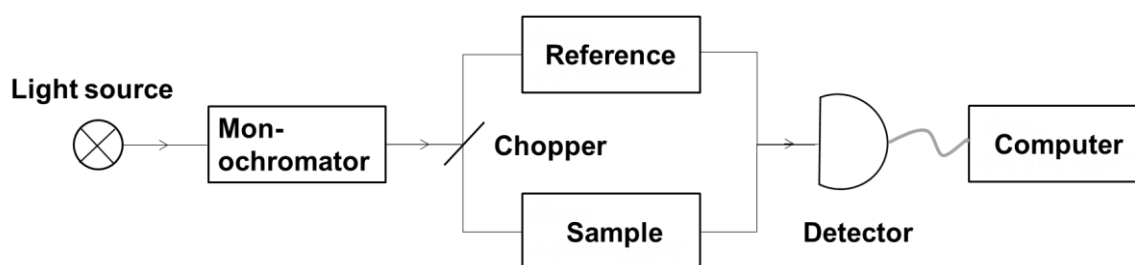


**Figure 4.3** Schematic of the setup for a dual-beam UV-Vis spectrophotometer.

Additionally, the UV-Vis spectrophotometer can be used to measure the reflectivity using a reflective sample holder. A mirror with known reflectance is the reference sample here. The relation between absorption  $A_\lambda$ , transmittance  $T_\lambda$  and reflectance  $R_\lambda$  is

$$A_\lambda = 100 - R_\lambda - T_\lambda \quad (4.3)$$

For a reflective sample without any transmittance ( $T_\lambda = 0$ ), the absorption ( $A_\lambda$ ) of the sample can be directly calculated from the reflectance.

In **Paper I-II**, the UV-Vis spectrophotometer was used to detect the energy positions of the upper and lower polariton states. A coupled harmonic oscillator model (introduced in **Section 2.3.3**) was used to analyze the dispersive behaviors of the polaritons to receive the Rabi splitting  $\hbar\Omega_R$  and the Hopfield coefficients. In addition, in **Paper III**, the UV-Vis spectrophotometer was utilized to detect the peak positions of the monomer and J-aggregates. Then, the value of the Coulombic coupling could be deduced from half the energy difference between the  $A_{0-0}$  values of the monomer and the aggregates.

#### 4.4 Emission spectra by photoluminescent spectrometer

A spectrofluorometer can be utilized to study the photoluminescence properties of a sample<sup>[120]</sup>. The settings are divided up into an excitation arm and an emission arm. The excitation arm consists of a light source with a broad spectrum, such as a xenon lamp. The white light goes through a monochromator to generate light of a specific wavelength. Then, the monochromated-light excites the sample and the emission spectrum is measured in another arm located at an angle of  $90^\circ$  to the excitation arm. The emission light passes through a monochromator before it is measured by a detector. For strongly scattering or absorbing samples, a front-face mode can be used to characterize the emission coming from the part of the sample where the excitation beam hits it first. Two different modes can be utilized to measure the excitation and emission spectra of a molecule. For the emission spectrum, the excitation wavelength is unchanged and the emission is measured for each wavelength. Regarding the excitation spectrum, the emission wavelength is fixed and the excitation wavelength changes. In practical terms, a low level of absorption of the sample is required, to avoid inner filter effects. Samples with a small Stokes shift and high absorption can reabsorb the emitted light and, thereby, manipulate the measured emission spectrum.

In our experimental settings, the prompt emission of the organic films was studied using conventional luminescence measurements. The prompt emission of the cavities was determined using the angle-dependent setup shown in **Figure 4.4**.

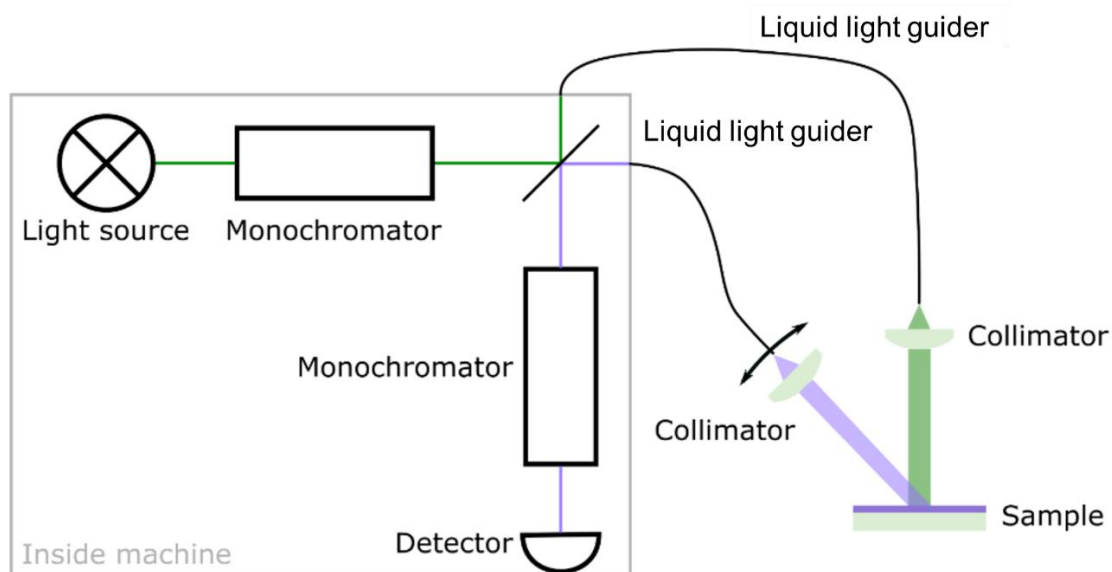


**Figure 4.4** Sketch of the spectrofluorometer connected via optical fibers to the homemade setup measuring the angle-dependent steady-state photoluminescence.

In addition, delayed emission spectra of the films and cavities were analyzed using the Edinburgh Instrument LP 980 spectrometer equipped with an ICCD (Andor). The gate delay was set to exclude the prompt emission signals (generally, 20–50 ns). The optical density or long-pass filter was used to protect the camera of the LP 980 from over-saturation. The details of the gate delay measurement will be provided in the next section.

## 4.5 The measurement of time-resolved photoluminescence spectra

### Time-correlated single photo counting (TCSPC)

In general, molecules can become relaxed from the excited state to the ground state through different radiative and non-radiative decays. The relaxation of simultaneously excited molecules does not take place at the same time, since the relaxation is based on probability. The reduction in emission intensity  $I$  is described by **Equation 4.4**,

$$I(t) = I_0 e^{-\frac{t}{\tau}} \quad (4.4)$$

where  $I(t)$  is the intensity after time  $t$ , and  $I_0$  is the initial intensity when the excitation stops. The emission lifetime  $\tau$  of an organic molecule can be measured using TCSPC. During this measurement, the sample is excited by a short-pulsed laser, which also starts a timer. The detection of an emitted photon stops the timer (**Figure 4.5, a and b**). This process is repeated until a statistically significant number of measurements has been performed.

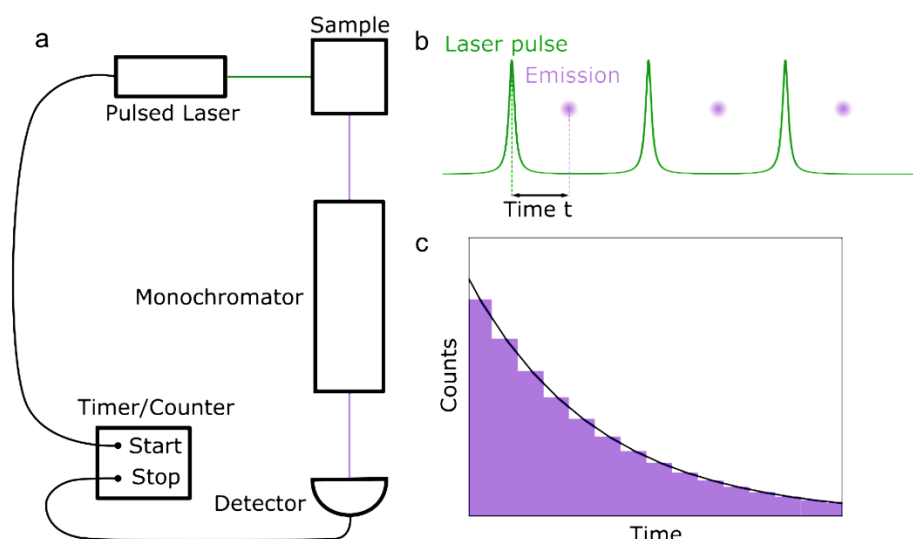


**Figure 4.5** (a) Sketch of the TCSPC setup to measure the time-resolved photoluminescence; (b) measurement of start-stop times with TCSPC and (c) histogram of the measured times.

All the measured times are plotted in a histogram against the number of counts (**Figure 4.5c**). Only the first photon is detected. Therefore, it is crucial that less than one photon is collected per 100 excitation pulses. Otherwise, there is the possibility that two photons are emitted such that the measurement is shifted to a shorter lifetime. The decay of the histogram resembling the intensity decay at a certain emission wavelength can be fitted using **Equation 4.5**.

$$I(t) = \sum_{i=1}^n \alpha_i e^{-\frac{t}{\tau_i}} \quad (4.5)$$

where  $\alpha_i$  is the pre-exponential factor representing the amplitude of a component at time  $t = 0$ ,  $\tau_i$  is the decay time of the component, and  $n$  is the number of components. Therefore, it is described as the sum of the different emitting components at a certain wavelength. The different components of a multi-exponential decay can be the result of a mixture of distinct chromophores that are emitting light at the same wavelength with different decays or different

regions of a sample having various morphological or aggregational states.

The resolution of the measurements depends on the pulse width of the excitation laser and on the response time of the detector. The laser width and detector response are measured as the instrument response function (IRF), and are involved in the re-convolution fitting.

TCSPC was used to determine the lifetimes of the prompt emissions in the nanosecond range. The lifetimes of the delayed emissions were measured using single-photon counting multichannel scaling (MCS) with the Spectra-Physics Nd:YAG 532-nm laser (pulse width  $\sim 7$  ns) coupled to the Spectra-Physics primoScan optical parametric oscillator (OPO). MCS is a complementary, time-resolved technique to the more widely known TCSPC, and is the method of choice for measuring delayed fluorescence. In MCS measurements, the detection window is split into time intervals and all the photons that arrive within a specified time interval are recorded; the signals in the next interval are then counted and so on until the entire time range has been recorded. This multiple-stop mode of detection makes the detection count rates higher, as compared with the measurements performed with TCSPC, which reduces the characterization time of longer decays.

When measuring the long lifetimes of the TADF system, as shown in **Figure 4.6**, the intensity of the prompt component may be several orders of magnitude greater than that of the delayed component. Therefore, the disparity between the emission intensities of the prompt and delayed parts is likely to make the MCS measurement inefficient.

The solution to this problem is to time-gate the PMT detector. By gating the detector, the high voltage to the PMT is only applied manually, using settings known as the gate. The time between the start of the excitation pulse and the start of the gate (namely, the gate delay) and the length of the gate are selected according to the relationship between the prompt and delayed emission lifetimes. More specifically, the gate delay is chosen such that the fluorescence has ended, which simultaneously enables higher count rates to be used and isolates the delayed emission from the prompt emission. Meanwhile, the gate width is set according to the lifetime of the sample. The width should be sufficiently long to include all the signals when the emission is long-lived.

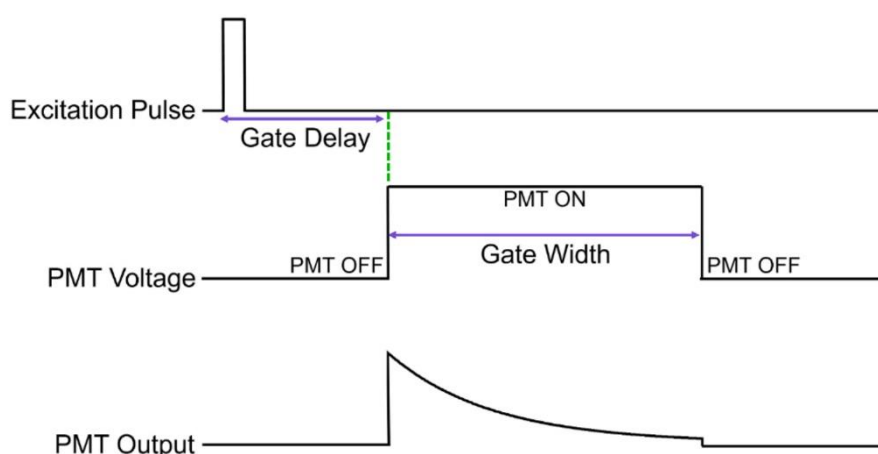


**Figure 4.6** Timing diagram of a gated PMT detection

## 5. Summary and Outlook

The work in the thesis focuses on fundamental studies of the molecular transition dynamics in strong exciton-photon and exciton-exciton coupling regimes. Through manipulation of the electronic transition without changing the molecular structures, several valuable insights are gained.

In **Paper I** and **Paper II**, the effects of strong exciton-photon coupling on the transition dynamics were discussed. Most of the previous literatures on the molecular photophysics of the strong exciton-photon coupling regime has focused on the excited singlet state. In these papers, the transition dynamics in the strong coupling regime were studied considering the triplet channel.

As for **Paper I**, some TADF molecules were inserted into optical cavities. By modification of the cavity thickness, different detuning profiles of the cavities were realized. As a result, the newly-generated exciton-photon hybrid states ( $P^+$  and  $P^-$ ) had different energy positions. In one multiple resonance TADF molecule (DABNA-2), it was noted that the  $P^-$  state could be lower than the excited triplet state. In other words, a singlet-triplet inversion has been achieved by strong exciton-photon coupling. When the molecular contribution is sufficient in the  $P^-$  state, the energy inversion results in a driving force to transfer the energy directly from the triplet state to the  $P^-$  state at low temperatures. In other words, barrier-free RISC occurs when DABNA-2 is inside the cavity. This suggests that strong exciton-photon coupling can break Hund's rule to facilitate triplet harvesting. Furthermore, it was noticed that the connection between the triplet state and the polaritonic state depended on the detuning. When the energy position of the cavity is far lower than the molecular transition, the direct connection was lost due to the low molecular contribution in the  $P^-$  state. Thus, the barrier-free transition was replaced with a conventional thermally activated process from the triplet to the exciton reservoir. One donor-acceptor TADF molecule was also placed in the cavity to reach the strong coupling regime. Even though the molecule realized a larger Rabi splitting, the inverted energy state was not achieved. This is due to the large Stokes shift of the molecule. The results obtained for the exciton-photon interactions between molecules and optical cavities motivate studies directed towards OLED and organic laser applications.

In **Paper II**, the interactions between an exciton-photon hybrid state and excimer trap states were studied. It was observed that delayed excimer emission dominated the long-lived emission process for DABNA-2 at room temperature in neat films. Considering the ratio of the  $P^-$  to excimer delayed emissions, a clear dependency on detuning was observed. Concretely, the more

red-detuned the cavities were, the higher the ratio of the delayed polariton emission. In a blue-detuned cavity, excimer emission dominated the long-lived emission process, similar to the case in the neat film. This result can be explained by the energy positions in the different cavities. A more red-detuned cavity narrows the energy gap between the  $P^-$  state and excimer trap state. Thus, the transition from the trap to the  $P^-$  state will be easier. On the other hand, the control of excimer emission by strong coupling was also observed for et-perylene. Its excimer emission is due to the transition from the excited singlet state to the excimer state. A similar detuning dependency was discovered here as well. In this case, more red-detuned cavities resulted in a larger energy gap between the dark and  $P^-$  states. A larger energy gap leads to a larger driving force for  $P^-$  emission, instead of excimer formation. Overall, strong exciton-photon coupling has potential applications aimed at increasing the efficiency and color purity of molecular emitters.

Other than exciton-photon coupling, in **Paper III**, the molecular photophysics was studied in the strong exciton-exciton coupling regime. Initially, it was observed that bay-alkylated quaterrylene formed J-aggregates when dissolved in 1,1,2,2-tetrachloroethane (TCE), and these aggregates showed significantly different optical properties compared to the monomeric molecule. Then, the dye in TCE was found to have a high emission quantum yield in the NIR regime, which cannot be completely explained by the well-studied super-radiant effect. Next, the delocalization length of the J-aggregates was analyzed by different strategies, which indicated that the excited state is coherently delocalized. Finally, using a semi-quantitative method, the unprecedented decrease in the non-radiative rate of a J-aggregate could be coupled to the excitonic delocalization. Accordingly, this result emphasizes the significance of delocalization of the excited state for achieving high-color-purity, highly emissive NIR dyes.

In conclusion, the molecular photophysics of the strong exciton-photon and exciton-exciton coupling systems were studied. The generated hybrid states were observed to change the molecular transition dynamics. New transfer pathways or more-efficient radiative processes were explored. However, it is clear that the accomplishment on an applied perspective is yet to be realized through the strongly coupled systems above. The challenge for the application is the different architectures between the experimental and practical settings. For example, the structure of our cavities is of great difference from that of the OLED devices. Nonetheless, weak exciton-photon coupling has been achieved in practical devices<sup>[121]</sup>. It is believed that strongly coupled systems will be explored for the practical application in the future.

In addition, solid theoretical frameworks are vital to in-depth understanding of strong coupling phenomena. Recently, Born-Oppenheimer approximation and quantum electrodynamic DFT has been developed for the strongly coupled system<sup>[122, 123]</sup>. These theoretical models are expected to assist the experimental design from now on.

Today, researchers from various background have been studying the newly generated energy states and different transition dynamics through strong coupling. Only our minds will be the limitation for the molecular strongly coupled systems!

# Acknowledgement

First and foremost, I would like to thank my supervisor Prof. Karl Börjesson for the opportunity to be a PhD student in the Molecular Materials research group. It is really appreciated of me to work with you who touched me during all of my PhD period by your enthusiasm for science. I still remember the time that you taught me what is strong coupling in the beginning. Later, I could get precious inspiration after the scientific discussion with you in each time. Your patience has handled my stubbornness. Accordingly, you improved my work to a much higher level and brought me to the fascinating scientific world.

I'd like to thank my examiner Prof. Johan Bergenholtz as well. You guided me about the course selection and gave me valuable scientific suggestion in the PhD period. In addition, I would like to express my appreciation to my co-supervisor Prof. Gunnar Nyman for his help during each discussion with him.

I would like to express my gratitude to Dr. Jenny Clark for accepting to be my opponent, as well as Prof. Maria Abrahamsson, Prof. Ivan Scheblykin, Prof. Alexander Dmitriev and Prof. Joakim Andreasson as members of the grading committee.

To all my current and past group member: Yizhou, Clara, Andrew, Rahul, Jürgen, Martin, Alex, Arpita, Mao, Chen, Xing, Manuel, Pedro and Suman. I am very lucky to be in the same group with you all. I get valuable information when talk with you in working time, and feel relaxed with you after work.

I would like to thank all the administrative staff to reduce my burdens for routine work. Thanks Johanna, Catarina, Gabriella, Linn, Lotta, Marilia, Ingrid and everyone else.

Thank you Yongjin for giving me suggestion in pharmaceutical science, and thank you Chao for teaching me programming and machine learning.

To all the professors, researchers and engineers on the 8<sup>th</sup> floor: Morten, Anna, Marica, Henrik, Carl, Kristina, Philipp, Jürgen, Daniel, Bijan and everyone else.

To all the present and former colleagues on the 8<sup>th</sup> floor: David, Diego, Amalyn, Mullah, Anna, Lisa, Chunxia, Josipa, Anders, Alexandra, Leticia, Peter, Luisa, Jordi, Hanna, Shitanshu, Helal Karan, Rickard, Alica, Jeemol, Monica and everyone else. I also want to thank the chemists and spectroscopist on 5<sup>th</sup> floor: Rasmus, Lili, Fredrik and Ignacio.

I would like to thank previous colleagues and my dear friends in China. Thanks for sharing news with me when I am home sick.

感谢我的父母。你们是我最好的老师，教会了我做人的道理，武汉的家永远是我最好的休憩港湾。感谢我的岳父岳母。我感觉自己不仅仅是你们的女婿，而更像你们的亲生儿子。同时也感谢我的其

他亲人在我生活上的帮助。

最后感谢我的妻子。记得当时是你鼓励我去瑞典读博。不可否认的是在很多重大问题的选择上，你都十分睿智。我并没有这般天赋，但对我而言，我自己在五年多以前做出了人生最正确选择。现在想来，我们从相恋到现在已经快十年了，我们并没有对对方感觉任何的厌烦(也有可能是我单方面吧)，而是持续的互相鼓励和扶持，并不断地发现对方的闪光点。执子之手，夫复何求？

# Bibliography

1. Kwan, A., *et al.*, Who really discovered Snell's law? *Physics World* **2002**, *15* (4), 64.
2. Maxwell, J. C., VIII. A dynamical theory of the electromagnetic field. *Philosophical transactions of the Royal Society of London* **1865**, (155), 459-512.
3. Maxwell, J. C., *On Faraday's lines of force*. Good Press: 2021.
4. De Broglie, L. Recherches sur la théorie des quanta. Migration-université en cours d'affectation, 1924.
5. Dirac, P. A. M.; Bohr, N. H. D., The quantum theory of the emission and absorption of radiation. **1927**, *114* (767), 243-265.
6. Sasitharan, K., *et al.*, Metal–organic framework nanosheets for enhanced performance of organic photovoltaic cells. *Journal of Materials Chemistry A* **2020**, *8* (12), 6067-6075.
7. Tian, H., *et al.*, CHAPTER 3 Dye-sensitised Solar Cells. In *Solar Energy Capture Materials*, The Royal Society of Chemistry: 2019; pp 89-152.
8. Chen, W., *et al.*, Nanophotonics-based low-temperature PECVD epitaxial crystalline silicon solar cells. *Journal of Physics D: Applied Physics* **2016**, *49* (12), 125603.
9. Jayaprakash, R., *et al.*, A hybrid organic–inorganic polariton LED. *Light: Science & Applications* **2019**, *8* (1), 81.
10. Ferri, J., *et al.*, Enhancement of laser-driven ion acceleration in non-periodic nanostructured targets. *Journal of Plasma Physics* **2020**, *86* (1), 905860101.
11. Fredin, L. A., *et al.*, Excited State Dynamics of Bistridentate and Trisbidentate RuII Complexes of Quinoline-Pyrazole Ligands. *Inorganic Chemistry* **2019**, *58* (24), 16354-16363.
12. Shi, J., *et al.*, Energy transfer in multi-funnel systems quantitatively assessed by two-dimensional polarization imaging and single funnel approximation: From single molecules to ensembles. *The Journal of Chemical Physics* **2022**, *156* (7), 074108.
13. Eremchev, I. Y., *et al.*, Lack of Photon Antibunching Supports Supertrap Model of Photoluminescence Blinking in Perovskite Sub-Micrometer Crystals. *Advanced Optical Material* **2021**, *9* (3), 2001596.
14. Abrahamsson, M., *et al.*, A New Strategy for the Improvement of Photophysical Properties in Ruthenium(II) Polypyridyl Complexes. Synthesis and Photophysical and Electrochemical Characterization of Six Mononuclear Ruthenium(II) Bisterpyridine-Type Complexes. *Inorganic Chemistry* **2005**, *44* (9), 3215-3225.
15. Andréasson, J.; Pischel, U., Light-stimulated molecular and supramolecular systems for information processing and beyond. *Coordination Chemistry Reviews* **2021**, *429*, 213695.
16. Dmitriev, A. In *Nanoscale tunable optics for photovoltaics and beyond*, 2018 25th International Workshop on Active-Matrix Flatpanel Displays and Devices (AM-FPD), 3-6 July 2018; 2018; pp 1-3.
17. Bossanyi, D. G., *et al.*, Emissive spin-0 triplet-pairs are a direct product of triplet–triplet annihilation in pentacene single crystals and anthradithiophene films. *Nature Chemistry* **2021**, *13* (2), 163-171.
18. Polak, D., *et al.*, Manipulating molecules with strong coupling: harvesting triplet excitons in organic exciton microcavities. *Chemical Science* **2020**, *11* (2), 343-354.
19. Simpson, W. T.; Peterson, D. L., Coupling Strength for Resonance Force Transfer of Electronic Energy in Van der Waals Solids. *The Journal of Chemical Physics* **1957**, *26* (3), 588-593.
20. Kasprzak, J., *et al.*, Bose–Einstein condensation of exciton polaritons. *Nature* **2006**, *443* (7110), 409-414.
21. Amo, A., *et al.*, Collective fluid dynamics of a polariton condensate in a semiconductor microcavity. *Nature* **2009**, *457* (7227), 291-295.
22. Carusotto, I.; Ciuti, C., Quantum fluids of light. *Reviews of Modern Physics* **2013**, *85* (1), 299-366.
23. Karzig, T., *et al.*, Topological Polaritons. *Physical Review X* **2015**, *5* (3), 031001.
24. Nakayama, T.; Kakuta, A., Organic Luminescent Devices with a Multiplex Cavity Structure. *Japanese Journal of Applied Physics* **1995**, *34* (9B), L1234.

25. Tessler, N., *et al.*, Lasing from conjugated-polymer microcavities. *Nature* **1996**, 382 (6593), 695-697.
26. Lidzey, D. G., *et al.*, Mapping the confined optical field in a microcavity via the emission from a conjugated polymer. *Applied Physics Letters* **1997**, 71 (6), 744-746.
27. Tsutsui, T., *et al.*, Sharply directed emission in organic electroluminescent diodes with an optical-microcavity structure. *Applied Physics Letters* **1994**, 65 (15), 1868-1870.
28. Pockrand, I., *et al.*, Exciton-surface plasmon coupling: An experimental investigation. *The Journal of Chemical Physics* **1982**, 77 (12), 6289-6295.
29. Agranovich, V., *et al.*, Organic and inorganic quantum wells in a microcavity: Frenkel-Wannier-Mott excitons hybridization and energy transformation. *Solid State Communications* **1997**, 102 (8), 631-636.
30. Lidzey, D. G., *et al.*, Strong exciton-photon coupling in an organic semiconductor microcavity. *Nature* **1998**, 395 (6697), 53-55.
31. Maiti, N. C., *et al.*, J- and H-Aggregates of Porphyrin-Surfactant Complexes: Time-Resolved Fluorescence and Other Spectroscopic Studies. *The Journal of Physical Chemistry B* **1998**, 102 (9), 1528-1538.
32. Gierschner, J., *et al.*, Absorption, fluorescence and light scattering of oligothiophene and oligophenylenevinylene nanoaggregates. *Synthetic Metals* **1997**, 84 (1), 529-530.
33. Hestand, N. J.; Spano, F. C., Expanded Theory of H- and J-Molecular Aggregates: The Effects of Vibronic Coupling and Intermolecular Charge Transfer. *Chemical Reviews* **2018**, 118 (15), 7069-7163.
34. Stranius, K., *et al.*, Selective manipulation of electronically excited states through strong light-matter interactions. *Nature Communications* **2018**, 9 (1), 2273.
35. Zhu, S., *et al.*, Near-Infrared-II Molecular Dyes for Cancer Imaging and Surgery. *Advanced Material* **2019**, 31 (24), 1900321.
36. Luo, S., *et al.*, A review of NIR dyes in cancer targeting and imaging. *Biomaterials* **2011**, 32 (29), 7127-7138.
37. Hertz, H., Ueber einen Einfluss des ultravioletten Lichtes auf die elektrische Entladung. *Annalen der Physik* **1887**, 267 (8), 983-1000.
38. Millikan, R. A., A direct photoelectric determination of Planck's "h". *Physical Review* **1916**, 7 (3), 355-388.
39. Bohr, N., XXXVII. On the constitution of atoms and molecules. *The London, Edinburgh, Dublin Philosophical Magazine Journal of Science* **1913**, 26 (153), 476-502.
40. Einstein, A., Strahlungs-emission und-absorption nach der Quantentheorie. *Verh. Deutsch. Phys. Gesell.* **1916**, 18, 318-323.
41. Rubens, H.; Kurlbaum, F., On the heat radiation of long wave-length emitted by black bodies at different temperatures. *The astrophysical journal* **1901**, 14, 335.
42. Kavokin, A. V., *et al.*, *Microcavities*. Oxford university press: 2017; Vol. 21.
43. Schrödinger, E., The Schrödinger equation. *Physical Review* **1926**, 28 (6), 1049-1070.
44. Atkins, P. W.; De Paula, J., *Physikalische chemie*. John Wiley & Sons: 2013.
45. Born, M.; Heisenberg, W., Zur Quantentheorie der Molekeln. In *Original Scientific Papers Wissenschaftliche Originalarbeiten*, Blum, W.; Rechenberg, H.; Dürr, H.-P., Eds. Springer Berlin Heidelberg: Berlin, Heidelberg, 1985; pp 216-246.
46. Mulliken, R. S., Spectroscopy, molecular orbitals, and chemical bonding. *Science* **1967**, 157 (3784), 13-24.
47. Vanquickenborne, L. G., *et al.*, Transition Metals and the Aufbau Principle. *Journal of Chemical Education* **1994**, 71 (6), 469.
48. Altunbulak, M.; Klyachko, A., The Pauli Principle Revisited. *Communications in Mathematical Physics* **2008**, 282 (2), 287-322.
49. Katriel, J.; Pauncz, R., Theoretical Interpretation of Hund's Rule. In *Advances in Quantum Chemistry*, Löwdin, P.-O., Ed. Academic Press: 1977; Vol. 10, pp 143-185.
50. Morse, P. M., Diatomic Molecules According to the Wave Mechanics. II. Vibrational Levels. *Physical Review* **1929**, 34 (1), 57-64.
51. Ball, D. W., *Field guide to spectroscopy*. Spie Press Bellingham, Washington: 2006; Vol. 8.
52. Hughes, V.; Grabner, L. J. P. R., Energy Levels, Selection Rules, and Line Intensities for Molecular Beam Electric Resonance Experiments with Diatomic Molecules. *Physical Review* **1950**, 79 (5), 829.
53. Marian, C. M., Spin-orbit coupling in molecules. *Reviews in computational chemistry* **2001**, 17, 99-204.
54. Dirac, P. A. M., The quantum theory of the electron. Part II. *Proceedings of the Royal Society of London* **1928**, 118 (779), 351-361.
55. Konstantin, N. S. e.; Elena, A. B., Intramolecular heavy-atom effect in the photophysics of organic molecules. *Physics-Uspexhi* **2005**, 48 (3), 231.
56. Jablonski, A., Efficiency of Anti-Stokes Fluorescence in Dyes. *Nature* **1933**, 131 (3319), 839-840.
57. Verhoeven, J., Glossary of terms used in photochemistry (IUPAC Recommendations 1996). *Pure Applied Chemistry* **1996**, 68 (12), 2223-2286.
58. Kasha, M., Characterization of electronic transitions in complex molecules. *Discussions of the Faraday society* **1950**, 9, 14-19.
59. Foldy, L. L.; Wouthuysen, S. A., On the Dirac Theory of Spin 1/2 Particles and Its Non-Relativistic Limit.

*Physical Review* **1950**, *78* (1), 29-36.

60. Yang, Z., *et al.*, Recent advances in organic thermally activated delayed fluorescence materials. *Chemical Society Reviews* **2017**, *46* (3), 915-1016.

61. Englman, R.; Jortner, J., The energy gap law for radiationless transitions in large molecules. *Molecular Physics* **1970**, *18* (2), 145-164.

62. Bixon, M., *et al.*, Lifetimes for radiative charge recombination in donor-acceptor molecules. *Journal of the American Chemical Society* **1994**, *116* (16), 7349-7355.

63. Braslavsky, S. E., Glossary of terms used in photochemistry, 3rd edition (IUPAC Recommendations 2006). **2007**, *79* (3), 293-465.

64. Birks, J. B.; Christophorou, L. G., Excimer fluorescence spectra of pyrene derivatives. *Spectrochimica Acta* **1963**, *19* (2), 401-410.

65. Novotny, L., Strong coupling, energy splitting, and level crossings: A classical perspective. *American Journal of Physics* **2010**, *78* (11), 1199-1202.

66. Jaynes, E. T.; Cummings, F. W., Comparison of quantum and semiclassical radiation theories with application to the beam maser. *Proceedings of the IEEE* **1963**, *51* (1), 89-109.

67. Dicke, R. H., Coherence in Spontaneous Radiation Processes. *Physical Review* **1954**, *93* (1), 99-110.

68. Holstein, T.; Primakoff, H., Field Dependence of the Intrinsic Domain Magnetization of a Ferromagnet. *Physical Review* **1940**, *58* (12), 1098-1113.

69. Hopfield, J. J., Theory of the Contribution of Excitons to the Complex Dielectric Constant of Crystals. *Physical Review* **1958**, *112* (5), 1555-1567.

70. Deng, H., *et al.*, Exciton-polariton Bose-Einstein condensation. *Reviews of Modern Physics* **2010**, *82* (2), 1489-1537.

71. Skolnick, M. S., *et al.*, Strong coupling phenomena in quantum microcavity structures. *Semiconductor Science and Technology* **1998**, *13* (7), 645-669.

72. Hertzog, M., *et al.*, Strong light-matter interactions: a new direction within chemistry. *Chemical Society Reviews* **2019**, *48* (3), 937-961.

73. Agranovich, V. M., *et al.*, Hybrid Resonant Organic-Inorganic Nanostructures for Optoelectronic Applications. *Chemical Reviews* **2011**, *111* (9), 5179-5214.

74. Khitrova, G., *et al.*, Vacuum Rabi splitting in semiconductors. *Nature Physics* **2006**, *2* (2), 81-90.

75. Kasha, M., Energy Transfer Mechanisms and the Molecular Exciton Model for Molecular Aggregates. *Radiation Research* **1963**, *20* (1), 55-70.

76. Kasha, M., *et al.*, The exciton model in molecular spectroscopy. *Butterworths: London, U.K.* **1965**, Vol. 11 (3-4), 371-392.

77. Spano, F. C., The Spectral Signatures of Frenkel Polarons in H- and J-Aggregates. *Accounts of Chemical Research* **2010**, *43* (3), 429-439.

78. Halder, M., *et al.*, Reorganization energy and Stokes shift calculations from spectral data as new efficient approaches in distinguishing the end point of micellization/aggregation. *Analytical Methods* **2016**, *8* (13), 2805-2811.

79. Zhao, H.; Kalt, H., Energy-dependent Huang-Rhys factor of free excitons. *Physical Review B* **2003**, *68* (12), 125309.

80. Scholes, G. D., *et al.*, Using coherence to enhance function in chemical and biophysical systems. *Nature* **2017**, *543* (7647), 647-656.

81. Chen, Z., *et al.*, Near-IR Absorbing J-Aggregate of an Amphiphilic BF<sub>2</sub>-Azadipyromethene Dye by Kinetic Cooperative Self-Assembly. **2017**, *56* (21), 5729-5733.

82. Fidler, H., *et al.*, Superradiant emission and optical dephasing in J-aggregates. *Chemical Physics Letters* **1990**, *171* (5), 529-536.

83. Finkelstein, D.; Rubinstein, J., Connection between Spin, Statistics, and Kinks. *Journal of Mathematical Physics* **1968**, *9* (11), 1762-1779.

84. Tao, Y., *et al.*, Thermally Activated Delayed Fluorescence Materials Towards the Breakthrough of Organoelectronics. *Advanced Materials* **2014**, *26* (47), 7931-7958.

85. Milián-Medina, B.; Gierschner, J., Computational design of low singlet-triplet gap all-organic molecules for OLED application. *Organic Electronics* **2012**, *13* (6), 985-991.

86. Méhes, G., *et al.*, Enhanced Electroluminescence Efficiency in a Spiro-Acridine Derivative through Thermally Activated Delayed Fluorescence. *Angewandte Chemie International Edition* **2012**, *51* (45), 11311-11315.

87. Kim, H. J.; Yasuda, T., Narrowband Emissive Thermally Activated Delayed Fluorescence Materials. *Adv. Optical Mater.* n/a (n/a), 2201714.

88. Hatakeyama, T., *et al.*, Ultrapure Blue Thermally Activated Delayed Fluorescence Molecules: Efficient HOMO-LUMO Separation by the Multiple Resonance Effect. *Advanced Materials* **2016**, *28* (14), 2777-2781.

89. Kim, H. J.; Yasuda, T., Narrowband Emissive Thermally Activated Delayed Fluorescence Materials.

*Advanced Optical Materials* **2022**, n/a (n/a), 2201714.

90. Samanta, P. K., *et al.*, Up-Conversion Intersystem Crossing Rates in Organic Emitters for Thermally Activated Delayed Fluorescence: Impact of the Nature of Singlet vs Triplet Excited States. *Journal of the American Chemical Society* **2017**, *139* (11), 4042-4051.
91. Schmidt, K., *et al.*, Intersystem Crossing Processes in Nonplanar Aromatic Heterocyclic Molecules. *The Journal of Physical Chemistry A* **2007**, *111* (42), 10490-10499.
92. Brédas, J.-L., *et al.*, Charge-Transfer and Energy-Transfer Processes in  $\pi$ -Conjugated Oligomers and Polymers: A Molecular Picture. *Chemical Reviews* **2004**, *104* (11), 4971-5004.
93. Aizawa, N., *et al.*, Delayed fluorescence from inverted singlet and triplet excited states. *Nature* **2022**, *609* (7927), 502-506.
94. de Silva, P., Inverted Singlet–Triplet Gaps and Their Relevance to Thermally Activated Delayed Fluorescence. *The Journal of Physical Chemistry Letters* **2019**, *10* (18), 5674-5679.
95. Ehrmaier, J., *et al.*, Singlet–Triplet Inversion in Heptazine and in Polymeric Carbon Nitrides. *The Journal of Physical Chemistry A* **2019**, *123* (38), 8099-8108.
96. Sanz-Rodrigo, J., *et al.*, Negative Singlet–Triplet Excitation Energy Gap in Triangle-Shaped Molecular Emitters for Efficient Triplet Harvesting. *The Journal of Physical Chemistry A* **2021**, *125* (2), 513-522.
97. Ricci, G., *et al.*, Singlet-Triplet Excited-State Inversion in Heptazine and Related Molecules: Assessment of TD-DFT and ab initio Methods. *ChemPhysChem* **2021**, *22* (6), 553-560.
98. Pollice, R., *et al.*, Organic molecules with inverted gaps between first excited singlet and triplet states and appreciable fluorescence rates. *Matter* **2021**, *4* (5), 1654-1682.
99. Dias, F. B., *et al.*, Photophysics of thermally activated delayed fluorescence molecules. *Methods and Applications in Fluorescence* **2017**, *5* (1), 012001.
100. Baleizão, C.; Berberan-Santos, M. N., Thermally activated delayed fluorescence as a cycling process between excited singlet and triplet states: Application to the fullerenes. *The Journal of Chemical Physics* **2007**, *126* (20), 204510.
101. Dias, F. B., *et al.*, The Role of Local Triplet Excited States and D-A Relative Orientation in Thermally Activated Delayed Fluorescence: Photophysics and Devices. *Advanced Science* **2016**, *3* (12), 1600080.
102. Kaji, H., *et al.*, Purely organic electroluminescent material realizing 100% conversion from electricity to light. *Nature Communications* **2015**, *6* (1), 8476.
103. Kim, D.-H., *et al.*, High-efficiency electroluminescence and amplified spontaneous emission from a thermally activated delayed fluorescent near-infrared emitter. *Nature Photonics* **2018**, *12* (2), 98-104.
104. Hatakeyama, T., *et al.*, Ultrapure Blue Thermally Activated Delayed Fluorescence Molecules: Efficient HOMO–LUMO Separation by the Multiple Resonance Effect. *Adv. Mater.* **2016**, *28* (14), 2777-2781.
105. Liang, X., *et al.*, Peripheral Amplification of Multi-Resonance Induced Thermally Activated Delayed Fluorescence for Highly Efficient OLEDs. *Angew. Chem. Int. Ed.* **2018**, *57* (35), 11316-11320.
106. Stranius, K., *et al.*, Selective manipulation of electronically excited states through strong light–matter interactions. *Nat. Commun.* **2018**, *9* (1), 2273.
107. Andre, J., *et al.*, Kinetics of partly diffusion controlled reactions. 22. Diffusion effects on the kinetics of excimer formation. *J. Phys. Chem.* **1990**, *94* (7), 2942-2948.
108. Halder, M., Determination of the critical micellar concentration (CMC) of a cationic micelle from Stokes shift data. *Chem. Educ.* **2007**, *12* (1), 33-36.
109. Jordanides, X. J., *et al.*, Solvation Dynamics in Protein Environments Studied by Photon Echo Spectroscopy. *The Journal of Physical Chemistry B* **1999**, *103* (37), 7995-8005.
110. Spano, F. C., *et al.*, Reclassifying exciton-phonon coupling in molecular aggregates: Evidence of strong nonadiabatic coupling in oligothiophene crystals. **2007**, *127* (18), 184703.
111. Wei, Y.-C., *et al.*, Overcoming the energy gap law in near-infrared OLEDs by exciton–vibration decoupling. *Nature Photonics* **2020**, *14* (9), 570-577.
112. Chen, W.-C., *et al.*, Low Internal Reorganization Energy of the Metal–Metal-to-Ligand Charge Transfer Emission in Dimeric Pt(II) Complexes. *The Journal of Physical Chemistry C* **2019**, *123* (16), 10225-10236.
113. Zeng, W., *et al.*, Rylene Ribbons with Unusual Diradical Character. *Chem* **2017**, *2* (1), 81-92.
114. Zeng, W., *et al.*, Cyclopenta-fused perylene: a new soluble, stable and functionalizable rylene building block. *Science Bulletin* **2015**, *60* (14), 1266-1271.
115. Miletić, T., *et al.*, A Twisted Bay-Substituted Quaterylene Phosphorescing in the NIR Spectral Region. *Helvetica Chimica Acta* **2017**, *100* (11), e1700192.
116. Chen, Z., *et al.*, Near-IR Absorbing J-Aggregate of an Amphiphilic BF2-Azadipyromethene Dye by Kinetic Cooperative Self-Assembly. *Angewandte Chemie International Edition* **2017**, *56* (21), 5729-5733.
117. Nee, A. Y. C., *Handbook of Manufacturing Engineering and Technology*. Springer Publishing Company, Incorporated: 2014.
118. Swann, S., Magnetron sputtering. *Physics in Technology* **1988**, *19* (2), 67-75.
119. Abitan, H., *et al.*, Correction to the Beer-Lambert-Bouguer law for optical absorption. *Appl. Opt.* **2008**, *47*

(29), 5354-5357.

120. Instrumentation for Fluorescence Spectroscopy. In *Principles of Fluorescence Spectroscopy*, Lakowicz, J. R., Ed. Springer US: Boston, MA, 2006; pp 27-61.

121. Zang, C., *et al.*, Top-emitting thermally activated delayed fluorescence organic light-emitting devices with weak light-matter coupling. *Light: Science & Applications* **2021**, *10* (1), 116.

122. Galego, J., *et al.*, Cavity Casimir-Polder Forces and Their Effects in Ground-State Chemical Reactivity. *Physical Review X* **2019**, *9* (2), 021057.

123. Sentef, M. A., *et al.*, Cavity quantum-electrodynamical polaritonically enhanced electron-phonon coupling and its influence on superconductivity. *Science Advances* **2018**, *4* (11), eaau6969.



# Appendix

